

*Copy 13 of 23*

LMSC-A642961

THE EFFECT OF BAFFLES  
ON TANK SLOSHING

Part I

December 1964

Richard G. Schwind  
Richard S. Scotti  
Jörgen Skogh

Final Report on NASA Langley Contract  
NASI-4065

## SUMMARY

36442

Three types of flexible baffles, cantilevered flexible, hinged, and slamming baffles were tested by subjecting the baffle to a sinusoidal velocity variation in water far from the free surface. Energy losses were obtained, made dimensionless as the loss coefficient, as a function of the flexibility and period parameter. The hydrogen bubble technique was developed and used to visualize the flow about the baffle. Two distinct flow regimes were observed. A 700 ft 16mm silent motion picture of the flow visualization has been made as part of this report. Six printed sections of this movie have been analyzed by tracing baffle tip and vortex center positions.

The cantilevered flexible baffle has an optimum flexibility for maximum loss coefficient, normalized by the loss coefficient of the rigid baffle. The optimum flexibility and normalized loss coefficient both increase with decreasing period parameter. The data for this type baffle has been fitted with an empirical equation and used to determine the baffle efficiency for circular tanks with axisymmetric and lateral slosh, and rectangular tanks with lateral slosh. At a period parameter of 2, the baffle with optimum flexibility is 10 times more efficient than a baffle which is nearly rigid.

*Author*

## TABLE OF CONTENTS\*

Section	Page
1 INTRODUCTION	1-1
1.1 The Problem	1-1
1.2 Related Work	1-1
1.3 Research Program	1-3
2 THE FLUID MECHANICS PROBLEM	2-1
2.1 Dimensional Analysis	2-1
2.2 Sloshing Tank Apparatus	2-2
2.2.1 Apparatus	2-2
2.2.2 Procedure	2-4
2.2.3 Results	2-5
2.3 Pendulum Apparatus	2-6
2.3.1 Apparatus	2-6
2.3.2 Procedure	2-7
2.3.3 Results	2-9
2.4 Flow Visualization	2-12
2.4.1 Apparatus	2-12
2.4.2 Procedure	2-14
2.4.3 Results	2-15
2.5 Discussion of Results	2-20
2.5.1 The Physical Phenomenon	2-20
2.5.2 The Pendulum Apparatus and Its Results	2-24
2.5.3 The Sloshing Tank Apparatus and Its Results	2-29
2.5.4 Flow Model Considerations	2-29

---

\*A 700 ft silent 16mm film of flow visualization, described in Section 2.4, has been prepared as part of this report.

Section		Page
3	EFFICIENCY AND OPTIMIZATION ANALYSIS OF TWO-DIMENSIONAL AND CIRCULAR BAFFLES	3-1
3.1	Modal Characteristics of Sloshing Motion	3-1
3.2	Stresses and Deflections	3-4
3.3	Determination of an Empiric-Analytic Expression for the Loss Coefficient	3-5
3.4	Baffle Efficiency	3-6
	3.4.1 Circular Cylinder Tank: Lateral Slosh	3-6
	3.4.2 Circular Cylinder Tank: Axisymmetric Slosh	3-10
	3.4.3 Two-Dimensional Rectangular Tank: Lateral Slosh	3-11
3.5	Baffle Weights Optimization	3-13

## Section 1 INTRODUCTION

### 1.1 THE PROBLEM

The danger of propellant sloshing causing unstable modes for space vehicles is well known. The amount of damping required for stability can be determined from analog studies. The problem is then reduced to finding a baffle arrangement of minimum weight which will perform the necessary amount of damping. The determination of this optimum might be attempted in full-scale or model tests. However, since baffles are usually annular plates mounted rigidly to the wall, if section loss coefficients are available for the various baffle types of interest, the optimum can be approximately determined analytically. Since a baffle is only effective when close to the surface a series of baffles will be required to provide the necessary damping in a draining tank. The baffle weight then becomes important. This study was initiated to examine the feasibility of using flexible and moveable baffle types for reducing the baffle weight for a given damping.

### 1.2 RELATED WORK

Miles (1)\* first used the potential solution for the fundamental slosh mode in a circular tank and combined it with section loss coefficients for a ring baffle. These he obtained from the drag coefficient data of Keulegan and Carpenter (2) for a perpendicular flat plate. Silveira, Stephens, and Leonard (3) tested various axisymmetric rigid baffles in two circular tanks and obtained very good agreement with O'Neill's version (4) of Miles' equation except when the baffle is one baffle width or closer to the surface as shown in Figure 1. Cole and Gambucci (5) obtained experimental loss coefficients

---

\*See Reference Section.

for a wide variety of two dimensional baffle shapes including the effect of a nearby free surface (see discussion in Section 2.5). They also tested two three-dimensional baffle shapes and the two-dimensional flat ring as used by Silveira et al but did not attempt to correlate any of their data with other author's results. Recently Abramson and Garza (6) also confirmed Miles' result for solid ring baffles and examined the effect of ring baffles with perforations in more detail. However, no rigid baffle has been reliably reported to be more effective per unit baffle weight than the simple ring baffle. Preliminary, unpublished evidence of Silveira, Stephens, and Leonard indicated that a flexible baffle could be more effective than a rigid baffle of the same size, \* and, of course, much lighter.

Using a different testing method Martin (7) also obtained drag coefficients for a perpendicular flat plate. While both Keulegan and Carpenter (2) and Martin (7) observed vortices being shed from the tips of their plates, they did not consider how the flow losses were related to these vortices.

The theoretical determination of the drag or energy loss of a bluff body, such as a perpendicular plate, would require either a complete solution of the Navier-Stokes equations for the desired boundary conditions or a good technique for obtaining approximate solutions. Even for laminar flow no Navier-Stokes solutions of interest have been obtained. For a bluff body in a steady flow Kirchhoff's free streamline theory and von Karman's vortex street have been combined by Roshko (8, 9) to obtain an approximate solution but it is still dependent upon one experimental measurement. Furthermore, this method does not give a fundamental explanation of the flow phenomenon involved immediately behind the body. For oscillating motion of the plate, a completely different flow occurs if the amplitude of the oscillation is small or of the same order of magnitude as the plate width. This phenomenon has been examined to some extent by McNown (10) and McNown and Keulegan (11) for a sinusoidal oscillation by examining the interrelation between the drag and virtual mass coefficients. Anten (12) has considered the growth of the vortex from the tip of a semi-infinite

---

\*Private communication from D. Stephens NASA Langley Field.

perpendicular plate which is instantaneously accelerated from zero to a constant velocity. Fromm (13) has successfully programmed the Navier Stokes equations in finite difference form onto a large computer and has obtained a solution for the starting flow about a perpendicular baffle extending into a channel at a Reynolds number of 400. For just how long after the starting of motion this program produces acceptable results is unknown. It is known, however, that convergence of the computer solution quickly becomes a problem as the Reynolds number increases.

### 1.3 RESEARCH PROGRAM

It still appears that the only method for obtaining loss coefficients for a given baffle shape is by experiment. Loss coefficients were measured with three types of baffles: a uniformly flexible baffle cantilevered from a wall, a rigid baffle but hinged to the wall and spring loaded, and a baffle free to translate perpendicular to its plane between rigid stops (see Figure 2.) These three baffles are denoted as Types I, II, and III, respectively. Considering the good agreement between Miles' theoretical relationship and Silveira's data described above, two major simplifications in obtaining loss coefficients were made: 1) use of only a sinusoidally-varying velocity field (or equivalently, oscillate the baffle in a sinusoidal manner in a quiescent fluid), and 2) elimination of the effect of the free surface. The meaning of these simplifications is discussed in Section 2.5. Two experimental apparatuses were used in this study. First the baffle was mounted in the center of the bottom of a rectangular tank and the decay of the sloshing amplitude noted. This is reported in Section 2.2. However, the maximum period parameter (see Section 2.1 for its definition) was limited to a value considerably below that expected by experimental uncertainty. Baffle Types I and III were then tested in a pendulum apparatus. This is reported in Section 2.3. To better understand the physical phenomenon involved flow visualization about the baffle was performed using the rather new technique involving hydrogen bubbles; see Section 2.4.

Using the two dimensional loss coefficients obtained in Section 2, the baffle flexibility for both circular and two-dimensional tanks is optimized in Section 3.

## Section 2

### THE FLUID MECHANICS PROBLEM

#### 2.1 DIMENSIONAL ANALYSIS

We consider here the dimensional analysis for a flexible baffle translating sinusoidally in an infinite, uniform fluid (far from a free surface.) If a plate perpendicular to the direction of motion is used to represent the baffle, then, one might expect that the flow would be symmetric and each half of the plate might be considered as representing a baffle mounted to an inviscid wall. However, as is discussed later, it is known that in steady flow the forces on such a plate are strongly affected by placing a splitter plate on the plane of symmetry. We add, then, to our geometry a splitter plate of length  $2S$  which is infinitely thin and parallel to the translation. The baffle is  $2D$  wide and has thickness  $t$  (we limit our discussion temporarily to the Type I baffle). The two-dimensional, incompressible flow problem can then be stated as (see List of Symbols)

$$\Delta E \text{ or } F = f(D, S, \rho, \mu, U, T, t, E, \nu, \rho_b) \quad (2.1)$$

These ten independent quantities contain three dimensions, for which the Pi theorem allows a maximum of 7 independent dimensionless quantities, but only 5 are used

$$\frac{\Delta E}{\rho U^3 T D} \text{ or } \frac{F}{\frac{\rho}{2} U^2 D} = f\left[\frac{UT}{D}, \frac{S}{D}, \frac{\rho U D}{\mu}, \left(\frac{D}{t}\right)^3 \left(\frac{1-\nu^2}{E}\right) \frac{\rho D^2}{T^2}, \frac{\rho}{\rho_b}\right] \quad (2.2)$$

If the baffle were negligibly thin but rigid, the first three quantities on the right side would determine the flow. For flexible baffles with small deflections it is known from stress analysis that  $\nu$  and  $E$  will only appear as  $(1-\nu^2)/E$ . In this study the baffle thickness will always be small enough as to not cause any noticeable fluid



mechanics effects, so  $t/D$  is not considered alone, but is combined as  $(D/t)^3(1 - \nu^2)/E$ , a parameter common in elasticity theory. It has been made dimensionless avoiding the use of velocity to keep its effect better separable from that of the period parameter, and is denoted the flexibility parameter,  $(D/t)^3[(1 - \nu^2)/E]\rho D^2/T^2 \equiv F_A$ . The third quantity is a Reynolds number. For the hinged baffle  $\nu$  and  $E$  are replaced in (1) by the torsional spring constant,  $k$ , and the appropriate flexibility parameter is developed in Appendix A. For the slamming baffle the flexibility parameter is based upon the gap between stops, the distance the baffle is allowed to travel,  $g$ , and is simply  $g/D$ , which is denoted the gap parameter. For both of these latter two cases the baffle is assumed to operate on frictionless pins.

## 2.2 SLOSHING TANK APPARATUS

There are two methods for determining the energy dissipation due to a body in a periodic flow. Either the instantaneous force can be integrated with respect to position change  $\int \vec{F} \cdot d\vec{x}$ , or the change in energy of the medium can be determined. This latter principle was used in both apparatuses of this study.

In a two-dimensional horizontal rectangular tank at rest containing an inviscid fluid in periodic motion due to the fundamental sloshing mode the velocity at a point is, in general, a complicated combination of trigonometric and hyperbolic functions. (See Ref. 2 for the equations.) However, on the centerline of the tank both the horizontal and vertical velocity components reduce to trigonometric functions. At the bottom of the tank the vertical component of the velocity is of course, zero. Furthermore, neither velocity component changes rapidly in this bottom center region of the tank. Advantage was taken of this phenomenon and baffles were mounted on the centerline at the bottom of a rectangular tank.

### 2.2.1 Apparatus

A glass tank 20 in. long by 12 in. wide was used for this experiment. The quiescent water depth was always 7.5 in. An extra bottom was placed in the tank so that the

bars clamping the baffle were flush with the bottom surface. (See Figure 2 for the arrangement of the baffles in the tank.) The tank rested on a flat surface hinged near one end of the tank. Figure 3 shows the tank with a baffle mounted in it, but the tank support has been modified for flow visualization.

A BLH SR4 strain gauge load cell under the other end measured the instantaneous torque about the hinge. A height probe simply consisted of seven electrical wires ending vertically at various heights between zero and 1-1/2 in. above the quiescent water level. The conductivity of the water was great enough so that it was easily determined what wires were reached by the surface during any cycle. The signals from both the height probe and load cell were recorded on a multichannel Offner Dynograph paper chart recorder. This recorder is distinguished by its rapid response accurate at 150 cps - and its linearity and sensitivity - as great as  $1 \mu\text{V}/\text{mm}$ . A decadivider battery arrangement allowed varying zero suppression so that the sensitive scales could be used here.

Type I baffles (cantilevered flexible) were cut from Type A mylar of various thicknesses between 0.001 and 0.010 in., and Type 302 stainless steel of 0.001 and 0.002 in. thickness. All baffles were cut so that  $1 \pm 0.01$  in. protruded above the bottom surface. Baffles of all three types extended the full 12 in. width of the tank, allowing only a few thousandths of an inch at each end for clearance. The thickness tolerance of the mylar was within 10% of the thickness, and within one half ten-thousands inch for the stainless steel. Young's modulus of elasticity and Poisson's ratio for the mylar were determined to be 800,000 psi and 0.3, respectively, for samples from the same supplier. The Type II baffle (hinged) consisted of 1/16 in. aluminum 1 in. by 12 in. A small pin hinge at each end allowed it to rotate. Four sets of springs were made, calibrated, and adjusted so as to have two of each spring constant ( $\pm 3\%$ ):  $k = 1.05, 0.43, 5.0,$  and  $11.4 \text{ oz}/\text{in.}$ , for spring sets 1, 2, 3, and 4, respectively. A set of these were attached to the baffle near one end at a radius arm of 0.20 in. (See Figure 2.)

The Type III baffle (slamming) was of the same material and size as the Type II, but supported 0.5 in. above the bottom surface by a long 1/16 in. diameter rod near each end of the baffle and perpendicular to it. The rods were supported in small journals about 4 in. from the baffle so as to be far from the fluid motion of the baffle. (See Figure 2.) The weight of the moving part, the baffle and rods, was 128 gm. Adjustable stops limited the baffle travel to various amounts. The friction at the sliding contacts was made as small as reasonably practical.

### 2.2.2 Procedure

From Kuelegan and Carpenter's second-order equations (2) for the shape of the surface and the velocity components of a fluid in a rectangular tank, the energy of the fluid is easily related to the maximum surface height. From their equations it is noted that when the fluid reaches its maximum amplitude during a cycle the velocity is everywhere zero (except for the rotational motion of the fluid) so all the fluid energy is potential energy, which is determined by integrating the surface shape. This yields (see Appendix B)

$$PE = \frac{g\rho a^2 LW}{4} \left[ 1 + \frac{k^2 a^2}{16} (N_1 + N_2)^2 \right]$$

where

$$a = \frac{-B + \sqrt{B^2 + 4Bh}}{2}$$

$$B = \frac{4}{k(N_1 + N_2)}$$

$$N_1 = \frac{\cosh 2kH}{\sinh 2kH}$$

$$N_2 = \frac{\cosh^2 kH (\cosh 2kH + 2)}{\sinh^3 kH}$$

Noting the fluid height at the end of the tank using the height probe simultaneously with the load cell reading allowed the latter to be expressed directly in terms of the potential energy. The calibration curves are shown in Figure 4. The torque due to the force on the baffle is negligible compared to the torque due to the wave because the baffle force has a very small moment arm.

The fluid is set in motion by carefully rocking the tank by hand at the natural frequency rate and then setting it down on the load cell. Good wave shapes were obtained with amplitudes as great as 2 in. The load cell output was recorded on the Offner on a very sensitive scale,  $2 \mu\text{V}/\text{mm}$ , with carefully calibrated zero suppression to allow accurate recording over a large range of wave amplitudes, 2 to 0.05 in.

A sample of the data is shown in Figure 5. Four or five runs were recorded and the peak load cell readings of the best three runs were averaged. These values were plotted and the slope of the resulting curves carefully determined by using the mirror technique. These slopes are proportional to the energy loss per cycle. The same procedure was performed for the no baffle case to obtain the residual losses. The slopes were then plotted versus load cell reading so that the no baffles loss could be deducted. Typical curves are shown in Figure 6. The velocity used in  $C_L$  and  $\frac{UT}{D}$  was that which would exist at the baffle tip if the baffle were not there. This procedure was also followed by Keulegan and Carpenter (2) for determining  $u$  and is discussed in Section 2.5.

### 2.2.3 Results

Figure 7 shows  $C_L$  vs  $\frac{UT}{D}$  for the Type I baffles. The average flexibility,  $F_A$ , is indicated for each baffle. The period increases about 2% as the period parameter decreased from 2.6 to 0.3 causing  $F_A$  to decrease 4% between these limits. While these data appear erratic in this plot with large bumps in the data, some interesting points are to be noted. The most flexible baffles, the 0.001, 0.0015, and 0.002 in. mylar have much steeper slopes than the rest, the last of these being the best baffle

for a range at the lower period parameters. Both stainless steel baffles have very pronounced minimum  $C_L$ 's near  $UT/D$  of 0.4. The stiffer mylar baffles behave very similarly to the rigid baffle.

Figure 8 shows  $C_L$  vs  $UT/D$  for the for Type I baffles tested and again, the rigid baffle (it is a limiting case for each type of baffle.) Even though there is a large range of flexibility in the 4 sets of springs, there are only very small differences between the resulting loss coefficients. For this reason, study of the Type II baffle was not pursued any further.

## 2.3 PENDULUM APPARATUS

### 2.3.1 Apparatus

For a pendulum oscillating through a small angle the angular velocity is sinusoidal, and at a large radius from the axis this motion will be nearly linear. Martin (7) made use of these principles to obtain average drag coefficients for rigid baffles by attaching them to a pendulum, and this method is used here. A tank 37 in. wide, 5 ft long and 6 ft high was available and used for these tests. To a 1-in. steel shaft held by two ball bearings was attached a pendulum arm and strut, as shown in Figures 9A and 9B. The strut, 1/4 in. thick and 30 in. long was tapered from 3 to 1 in. and aerodynamically shaped. The strut held the baffle through two baffle support bars, 36.8 in. from the shaft center to the baffle center (See Figures 10A and 11). These bars were 1/4 in. by 1-1/4 in. steel with outer edges tapered for better aerodynamic flow. The inner edges were kept square so as to clamp the baffle securely with 6 screws between the support bars. These bars were actually attached to the strut via two rigid offset angles so as to allow the upper half of the baffle considerable deflection before touching. The baffles and support bars were 36 in. long, allowing 1/2-in. clearance between the tank walls. At rest, the baffle was 25 in. from the surface and 37 in. from the bottom. At a deflection of 10 in., the baffle was 20 in. from the nearest wall. The pendulum arm consisted of a shaft 1.5 in. by 3.5 in. by 5 ft. Near the end were clamped eight 20 lb weights,

the maximum that could be conveniently attached. A pointer attached to this arm at 53.4 in. indicated the angular deflection on a ruler curved to this radius.

For testing Type III baffles, the baffle support bars were drilled and reamed to accept four small pins, the baffle being bolted to the center of the pins (Figure 10B). The bars were clamped together with various-sized spacers in between to create a gap from 0.022 to 0.413 in. wide for the baffle to slam back and forth, riding on the pins, (Figures 10B and 11). Several tests were made with rigid baffles without the baffle support bars and also with thin splitter plates of various lengths. These rigid baffles were made 1/8 in. thick, but with the edges tapered to 1/16 in. — the thickness of the rigid baffles that were clamped by the baffle support bars.

A strain gauge bridge consisting of four 120- $\Omega$  foil gauges was mounted on small sections of flat edges of the strut at a radius of 20 in. The signal from this bridge was amplified and recorded on the Offner Dynograph described in Section 2.2.2. A one-turn precision 20,000 - $\Omega$  potentiometer mounted on the end of the shaft was used to record instantaneous angular position. An angular velocity transducer was devised using the concept that current equals rate of change of the quantity, volts times capacitance. The voltage was held constant at 380 V across a variable air capacitor of 1,000 pF which was connected to the shaft. The capacitance varied linearly with angular deflection, so by measuring the current into the capacitor the angular velocity was determined.

### 2.3.2 Procedure

At the position of maximum angular deflection all of the energy in the pendulum is potential, thus

$$PE = Wr_{cg}(1 - \cos\theta) = Wr\left(\frac{\theta^2}{2} + \frac{\theta^4}{4} + \dots\right) \quad (2.3)$$

The quantity  $Wr_{cg}$  was determined by careful calibration using a string with a calibrated weight,  $w$ , hanging on it to deflect the pendulum an amount  $\theta$ ; by measuring the angle  $\beta$  the force  $F$  which is horizontal, need not be known. Since the sum of the torque is zero, the quantity  $Wr_{cg}$  is related to  $w$  and  $\beta$  by

$$Wr_{cg} = wr_a \left( \frac{1}{\tan \beta \tan \theta} - 1 \right) \quad (2.4)$$

From readings varying  $w$  and  $\beta$ ,  $Wr_{cg}$  was determined to be 999 ft lb for the tests described here.

The operating procedure, starting with negligible wave amplitude in the large tank, was to obtain the desired oscillation amplitude (usually 12 in. on the scales, approximately 12 deg) by carefully pulling on a string attached to the pendulum arm so as not to excite the bending natural frequency of the pendulum arm (if excited, this vibration would cause the strut and baffle to vibrate in the plane perpendicular to the plane of the main oscillation.) The velocity displacement and strain signals were then recorded on the Offner Dynograph while the maximum amplitude of each cycle was read manually. With a little practice it was possible to read this to the nearest graduation on the scale, 0.01 in. The data for the maximum deflections denoted  $r_m \theta$ , were plotted for two or three runs.

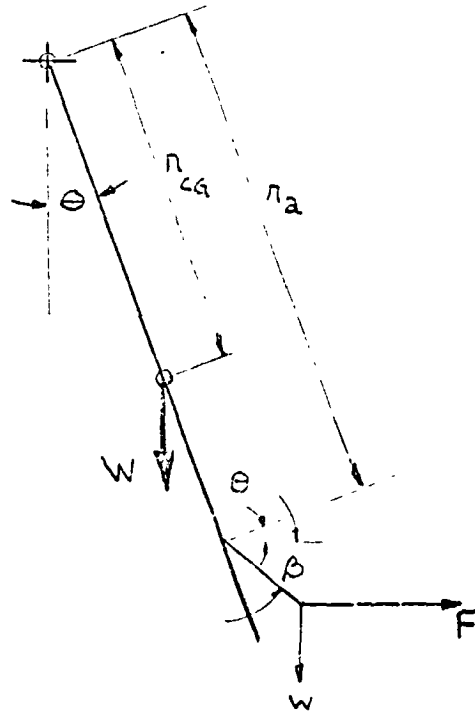


Figure 12 is a typical curve of  $r\theta$  vs cycle number. By determining the difference in  $r_m \theta$  for each cycle and using it in the differential of Eq. (2.3), the change in potential

energy (i. e., total energy) per cycle vs maximum angular deflections for the 3 in. by 0.005 in. mylar baffle is reflected in Figure 13. The losses in the system due to sources other than the baffle,  $\Delta e$ , were calibrated by performing the test without the baffle and baffle support bars. The net change in energy per cycle due to losses created by the baffle is then taken to be  $\Delta E = \Delta PE - \Delta e$ . At the low amplitudes where the net potential energy change for the baffle was one third or less of the gross potential energy change, the values were not plotted or used further.

The maximum velocity over a cycle,  $U$ , was obtained by noting that the motion of the pendulum is essentially sinusoidal, so  $U = x_0 \frac{2\pi}{T}$ , where  $x_0$  is the average of the maximum amplitudes at the beginning and end of a cycle. With the values of  $\Delta E$  and  $U$ , loss coefficients and period parameters were calculated using the definitions given in Section 2.1.

Considerable difficulty was encountered with drifting of the strain gauge calibration. A new set of strain gauges were mounted, relieving the problem considerably (both sets were mounted by experienced personnel in the solid mechanics laboratory). Fortunately, highly accurate strain gauge readings were not needed. The accuracy obtained was more than adequate to determine the maximum force for stress limit calculations and the relations between force, velocity, and displacement. The final strain gauge calibration shown in Figure 14 was determined by supporting the strut in a horizontal position and hanging calibrated weights at a known distance from the strain gauges.

### 2.3.3 Results

Offner chart recordings of force versus time for 3 in. rigid, 0.004 in. stainless steel and 0.005 in. mylar baffles are shown in Figure 15. Note that force is more peaked the more rigid the baffle. Similar recordings for the slamming baffle are shown in Figure 16.



Figure 17 shows force versus distance along the baffle arc as plotted by an x-y recorder for the 0.003 in. by 3 in. mylar baffle. The dark central spot is the  $F = x = 0$  position. Along a vertical line through this point  $x = 0$  and the velocity is a maximum (sinusoidal velocity variation is assumed by the large angular momentum of the pendulum arm) but the force is a maximum before this point is reached.

The loss coefficients as period parameter for 11 different Type I baffles are presented in Figures 18A through 18G in ascending order of flexibility. The increase in the period from 2.32 sec at large amplitudes of 10 deg deflection to 2.46 sec at small amplitudes causes negligible change in the flexibility parameter. The dotted curves are best fits and the solid curves are the empirical correlation described in Section 3.

$$C_L = A \left( \frac{UT}{D} \right)^B - J \exp \left( - E \frac{UT}{D} \right) + H \exp \left[ - 1 / \left( G \frac{UT}{D} \right)^2 \right]$$

where  $A$  and  $B$  are functions of flexibility. While the baffle is described by its full width, its half width is defined as  $D$  to be consistent with the slosh tank results. However, a further modification is necessary in the flexibility parameter to relate it to the tip deflection. Denoting the baffle support bar width as  $2\delta$

$$F = \left( \frac{D - \delta}{t} \right)^3 \left( \frac{1 - \nu}{E} \right) \frac{\rho D^2}{T^2} \quad (2.5)$$

For the 2-in. baffles the period parameter ranges from 3 to 30, and for the 4-in. baffles, 1 to 13. The average slope of the curves becomes increasingly more negative with greater flexibility. Little trend can be found in the shape of the curves except in general, the stiffer baffles tend to have very little curvature, and the few most flexible baffles tend to have an inflection point, being steepest in the middle. No consistent difference can be determined between the shape of the mylar and stainless steel curves.

Figure 19 is a cross plot of Figure 18, loss coefficient vs flexibility. Values for the rigid baffle,  $F = 0$ , are plotted on the y-axis and are limiting values. At the higher period parameters  $C_L$  continually decreases with flexibility, and the plotted points are very consistent. With decreasing period parameter, larger discrepancies between the baffles develop with the smaller baffles having larger loss coefficients. Curves determined from Eq. (2.5) are solid, the dotted again being best fit curves. Figure 20A shows rigid plate results for the no splitter plate case from all known sources: this apparatus with its 2 and 4 inch width baffles, Martin (7), and Keulegan and Carpenter (2). The results from these two references were presented as average drag coefficient, but this is converted to loss coefficient as follows:

$$\Delta E = \int_0^T \vec{F} \cdot \vec{U} dt = \frac{\rho}{2} \int U^3 D C_D dt$$

Taking  $C_D$  constant and  $U = U_0 \sin \omega t$

$$\Delta E = \rho D C_D U_0^3 \int_0^{\pi/\omega} \sin^3 \omega t dt = \frac{4}{3\omega} \rho D C_D U_0^3$$

$$C_L = \frac{2}{3\pi} C_D$$

The data of Martin and Keulegan and Carpenter agree very well. For the present 2 inch baffle tests,  $C_L$  is 20 percent below their values.

The effect of thin and thick splitter plates is examined in Figures 20B, 21A, and 21B. All 4-in. baffle cases are plotted in Figure 20B. The splitter plate to width ratio,  $S/D$  varies from 0 to 2, yet no effect can be detected. Figure 21A contains all 2-in. rigid baffle data. No difference exists between the 4 and 8-in. total-length splitter

plates, but with the baffle support bars (1/4-in. thick splitter, plates)  $C_L$  is 10% greater at large period parameter. The 4-in. baffle data are 10% greater,  $S = 0, 4$ . The sloshing tank results are also shown; they appear to be only one-third of the value obtained for the pendulum apparatus. The curves of Figure 21B are obtained using the baffle support bars with 1-, 2-, 3-, and 4-in. width baffles. Agreement is very good at lower period parameters, but each baffle shows a greater  $C_L$  at its maximum  $UT/D$  than the smaller baffles.

Twenty-seven Type III baffles were tested. They are listed in Table 1. Loss coefficient versus period parameter for the Type III baffle is plotted in Figures 22, 23, and 24. In the first, data for a 3-in. aluminum baffle with various gap-to-baffle width ratios is presented, including one with "zero gap" meaning no motion, though there was a total gap between the baffle support bars of 0.345 in., not including the baffle. To see if this gap had any appreciable effect on this size baffle, 3-in. Type I baffle results are also included, the support bars here being tight against the baffle. All values are within 10% of each other with no trend evident for the effect of gap width. Figure 23 shows the effect of baffle mass; 3-in. aluminum, plastic and stainless steel baffles all at a gap to width ratio of 0.139. In Figure 24 various width plastic baffles are plotted. The gap-to-width ratio, however, does vary here. Results from the other 25 runs with Type III baffles are not presented, as they show no further trends.

## 2.4 FLOW VISUALIZATION

### 2.4.1 Apparatus

Considerable experimenting with the apparatus was necessary before good pictures were obtained. The arrangement finally used is shown in Figure 3. The same tank used for the results reported in Section 2.2 was used, but with the support it was resting on now hinged in the middle. This was oscillated by a cam and lever arrangement that was driven by a variable speed gear motor. Several amplitudes of oscillations were available, all being only a few thousandths of an inch.

Table 1  
SLAMMING BAFFLE TEST PROGRAM

Run	Baffle Width (in. )	Baffle Material	Gap (in. )
(no baffle calibration)			
11-17-1	4	aluminum	0.278
-18-1			0.099
-2	3		0.413
-3			0.278
-4			0.099
-5			0.150
-6			0.055
-7			0.022
11-19-1			0.208
-2			0.336
-3			0
-4		phenolic	0.208
-5			0.413
-6			0.022
-7		stainless	0.022
(no baffle calibration)			
-8	3	stainless	0.208
-9			0.413
-10	4	phenolic	0.278
-11			0.208
(no baffle calibration)			
-12	4	phenolic	0.285
-13			0.343
-14	2		0.208
11-20-1			0.413
-2			0
-3	1		0.055
-4			0.413
-5			0
(no baffle calibration)			

Schraub, et al (15) have developed the hydrogen bubble technique for flow visualization, the method used here, into a most useful research tool for fluid flows. The apparatus consists of a d-c power supply, an R-C pulsing system and the probe itself. A universal electronic regulated power supply (Model 425-A) was used as the d-c source while the pulser was designed and built to allow for a wide range of pulsing rates. Two probes placed on the tank centerline each made of six 0.003-in. platinum wires which were soldered to heavier support wires. These support wires extended at a 45-deg angle from near the base of the baffle to the tank wall and were mounted on a rigid frame. The platinum wires, 1/2 in. long, lie parallel to the baffle length on each side. All supporting wires and exposed terminals were insulated by spraying with a sprayed-on liquid insulator. The probe was wired as one terminal while a metal plate placed in another part of the tank was connected to the other side of the d-c supply.

A Bell and Howell 16-mm movie camera was placed in line with the baffle 16 in. from the plane of flow visualization. Film speeds of 32 and 64 frames/sec were used. The points of interest in the film strips that were analyzed were read on a Vanguard film reader. This instrument projects the film on a ground glass screen, magnification cross hairs can be located over the point of interest and the position read to the nearest thousandths of an inch.

#### 2.4.2 Procedure

Considerable adjusting of the cam travel and motor speed setting was necessary to obtain the desired sloshing amplitude with the cam driving the apparatus near the natural frequency. This was necessary so as to obtain a vortex shedding pattern as symmetric as possible. At this point the motion of the tank was so small as to be negligible compared to the motion of the liquid in the tank. With the liquid oscillation at the desired amplitude, the d-c supply voltage and pulser rate were adjusted for the amount, texture, and timing of the bubble production. Typical currents were 10 to 20 mA with voltages of 35 to 50 V. Lighting was a very important factor and it was found that the collimated light from commercial 35-mm slide projectors gave favorable results. Two such projectors were used and placed one on each side of the tank

at an obtuse angle of 125 deg from the camera. A stroboscope light shining through a hole in the black background of the tank provided a source of accurate timing of the film speed.

### 2.4.3 Results

A 400-ft 16 mm motion picture is a part of this report. The various test conditions shown are listed in Table 2. Seven sections of this film were studied in great detail. For six of these sections, about 1-1/2 cycles, have been printed and are presented as Figures 25, 29, 33, 37, 41, and 45. The positions of the baffle tip, vortex centers, and an undisturbed particle in the main motion have been determined frame by frame for these seven cases and are included after each set of photographs as three figures: position versus time, velocity versus time, and path of travel (x vs y position). Some of these figures are graphs from the automatic plotter and one of its idiosyncrasies is that every symbol is plotted each time, even where not applicable. These non-applicable symbols are plotted as the initial or final values with no curves drawn through them.

In Frame 1 of Fig. 25, the rigid baffle case, the last two vortices shed are still seen in the upper right-hand corner. The main motion is just starting to the left. Hydrogen bubbles are just starting to stream away from the right probe, opposite the tip of the baffle. By Frame 6 a small vortex can be seen on the left side of the baffle. This continues to grow, and in Frame 16 bubbles from the left probe begin to visualize this vortex. By Frame 23, the vortex has grown to its maximum strength as indicated by the fact that the bubbles visualizing the vortex sheet trailing off the tip are beginning to move to the right, indicating that vorticity of the opposite sense is being shed. By Frame 27, the vortex of opposite sense is seen forming on the right. As it grows, interaction of the vortex velocity fields cause the vortices to induce velocity components in each other perpendicular to the line connecting the vortex centers. By Frame 37, the next cycle has started. This example is, unfortunately, very asymmetric. Better flow patterns were obtained later and are included in the motion picture.

Table 2

ORDER OF APPEARANCE OF BAFFLES IN FLOW VISUALIZATION FILM,  
"THE EFFECT OF FLEXIBLE BAFFLES ON TANK SLOSHING"

Baffle	Period Parameter	Flexibility
Rigid	0.79	0
(0.001) Mylar	0.79	$1.38 \times 10^{-1}$
(0.001) Stainless Steel	0.79	$3.65 \times 10^{-3}$
(0.003) Mylar	0.79	$5.09 \times 10^{-3}$
(0.010) Mylar	0.79	$1.38 \times 10^{-4}$
Type II, Spring Set 4	0.79	$6.15 \times 10^{-3}$
Rigid	1.80	0
(0.001) Mylar	1.80	$1.38 \times 10^{-1}$
(0.001) Stainless Steel	1.80	$3.65 \times 10^{-3}$
(0.003) Mylar	1.80	$5.09 \times 10^{-3}$
(0.010) Mylar	1.80	$1.38 \times 10^{-4}$
Type II, Spring Set 2	1.80	$1.64 \times 10^{-1}$
Type II, Spring Set 4	1.80	$6.15 \times 10^{-3}$
(0.003) Mylar - Damped Sloshing Starting With $UT/D = 2.8$		
Type III Baffle, $UT/D = 2.57$		
1-in. Rigid Baffle 1 in. From the Surface in a Sloshing Fluid Showing the Same Vortex Shedding Phenomenon		
Rigid ( $D = 0.6$ )	9.0	0
Rigid ( $D = 0.2$ )	30.0	0
Rigid ( $D = 0.6$ ) - Damped Sloshing Starting With $UT/D = 9.0$		
(0.001) Mylar ( $D = 0.5$ ) - Damped Sloshing Starting With $UT/D = 3.6$		
(0.001) Mylar ( $D = 0.5$ ) - Damped Sloshing Starting With $UT/D = 9.0$		
Rigid ( $D = 1.0$ ) - Baffle 1.5 in. From Tank Bottom, $UT/D = 10.0$		
Rigid ( $D = 0.5$ ) - Baffle 1.5 in. From Tank Bottom, $UT/D = 10.0$		

In Fig. 29, Frame 1, the 0.001 in. mylar baffle, operating at  $UT/D = 0.79$ , is just starting to move to the right. Four shed vortices are visible. At Frame 7, the new vortex is made visible. Vorticity in the boundary layers along the baffle is convected to the growing vortex via the vortex sheet (somewhat diffused by viscous action) extending from the baffle tip into the vortex. The x-y coordinates of this vortex are plotted in Fig. 30 as  $x_{VC1}, y_{VC1}$ , respectively. From Fig. 31 the undisturbed velocity (the velocity that would exist at the baffle tip if the baffle were not there)  $u_{\infty}$ , is seen to be equal to the baffle tip velocity at 0.31 sec near Frame 12, which is after the baffle has started returning to the left. Near this time, when the velocity of the baffle tip equals the velocity of the fluid without the necessity of a vortex sheet, the vortex sheet strength at the baffle tip decreases to zero and goes negative. The vorticity of this new sense forms the next vortex which is first seen in Fig. 24, though particles near the tip from Frame 17 on can be followed as they form this vortex. The positions of vortex centers and baffle tip vs. time can be followed in Fig. 30, the main motion and horizontal component of the baffle tip velocities vs. time, in Fig. 31, and vortex positions in an x-y plot, in Fig. 31. Note that the velocity of this baffle is essentially in phase with the main motion and that its wave shape is more peaked than a sine wave. In the plot of vortex paths (Fig. 32) note that the x-coordinate has been enlarged, that the x-position of the baffle tip is also plotted (at the maximum y-value), and that corresponding frame numbers are noted on the three vortex paths and baffle tip so that relative positioning can be easily recognized. From the photographs, it is seen that the vortices shed lie in a pattern with regular spacing above the baffle in the form of a von Karman vortex sheet. The baffle creates an overall motion of pulling fluid horizontally along the tank bottom (which is equivalent to a plane of symmetry of a baffle translating in an infinite fluid) and ejecting it vertically above the baffle.

Figure 33 shows the same baffle at a higher period parameter, 1.80. The flow is qualitatively the same as in Fig. 29. (It has been noted too late for correction that Frames 21 through 25 have been omitted.) Quantitatively, the baffle travels further, the vortex formed is further from the baffle, and the vortices rise in distinct pairs.



This causes the flow pattern here to be fundamentally asymmetric, and the mirror image of the flow could be easily obtained. The baffle tip is slightly out of phase LEADING the main motion. Note that if the flow were exactly the same each cycle the third vortex path would coincide with the first one, but this is never quite the case in the examples selected.

For the 0.001 in. thick stainless steel baffle at  $UT/D = 0.79$  shown in Fig. 37, the baffle tip motion is very small compared to the horizontal motion of the vortices (see also Fig. 40.) Again the baffle tip velocity slightly leads the main motion. Comparing the vortex paths of the 0.001-in. mylar baffle with this case, Figs. 32 and 40, the first and third vortices in the former case start farther from the baffle and sweep across the centerline before rising very far (0.2 of a baffle height), but in the latter case, these vortices first travel away from the baffle while rising, then sweep back just past the centerline about a baffle height above the baffle. The second vortex in these two cases also behave in opposite manners.

For the 0.001 in. stainless steel baffle at  $UT/D = 1.80$ , Figs. 41 through 44, the baffle tip velocity leads the main motion by more than 90 deg. The same qualitative differences exist between the vortex paths in this case as compared to the 0.001-in. mylar baffle at this period parameter (Figs. 36 and 44.)

The hinged baffle results of Fig. 45 through 48 show no strikingly different results. The equivalent flexibility is essentially the same as for the 0.001 mylar and so the results are compared with that baffle at the same period parameter, Figs. 33 through 36. The baffle tip for the mylar case travels twice as far as it does for this Type II baffle. This baffle tip velocity leads the main motion by 90 deg as compared to about 10 deg in the former case. From Figs. 46 and 47 it is noted that the baffle tip tends to move quickly from one side to the other but linger near the extreme deflection. The vortex path shape appears similar to the case of the more rigid 0.001 in. stainless steel baffle.

Figure 49(a) shows the baffle tip and first vortex x-positions vs. time for a 1-in. by 0.003 in. mylar baffle at a period parameter of 1.65, and corresponding

main motion, baffle tip and vortex x-component of velocity are included in Fig. 49(b). Prints of this case are not included but closely corresponding cases can be found in the motion picture.

The average vorticity in the vortices being shed was determined approximately for the above cases studied by assuming that away from the baffle the vortex motion is due only to induced velocity from the nearest vortex and the main motion. Values thus obtained are listed here along with period parameter and loss coefficient:

Baffle	UT/D	$C_L$	$\Gamma/UD$
1 in. by 0.001 mylar	0.79	2.9	0.11
1 in. by 0.001 stainless	0.79	2.35	0.055
1 in. by 0.001 mylar	1.80	1.3	0.20
1 in. by 0.001 stainless	1.80	1.95	0.22
Type II	1.80	1.44	0.28

Comparing the mylar and stainless baffles at the same period parameters some correspondence is seen between larger  $\Gamma/UD$  for larger  $C_L$ .

Included in the motion picture but not printed here are flow visualization of the slamming baffle, and more recent flow visualization about a flexible and a rigid baffle up to considerably higher period parameters. Above approximately  $UT/D = 4.0$ , a completely different flow regime is observed. The vortex formed on either side is not shed upward away from the baffle tip, but is quickly forced over the tip of the baffle and the newly forming vortex on that side and proceeds on away from the baffle parallel to the inviscid line of symmetry. The net flow direction is reversed from the earlier lower period parameter cases discussed, coming toward the baffle in its plane and flowing away with the expelled vortices along the centerline. This is depicted in Fig. 50. The flow pattern was able to change smoothly from this flow pattern to the low period parameter through a series of asymmetric flows as indicated in Fig. 50.

## 2.5 DISCUSSION OF RESULTS

It was intended at the outset that this would be primarily an analytical study of the effect of flexible baffles on inducing flow losses. However, separated flows has remained virtually untouched in fluid mechanics research for good reason – the complete Navier-Stokes are unsolvable in this general form, and the physical phenomena involved are simply not understood well enough to establish good flow models to simplify the mathematics. Preliminary flow visualization with ink in the tank used for the flow visualization presented soon led to preliminary flow-loss measurements to determine whether flexible baffles were indeed more effective, and if so, what baffle was most effective so that flow visualization of it could be compared with the rigid baffle. This led to the flow-loss measurements in the sloshing tank reported here. In the meantime flow visualization using ink was proving unsatisfactory for the detail desired and work started on developing and perfecting the hydrogen bubble technique. With the realization of the small differences between the best flexible baffle and the rigid one with little qualitative difference in the flow field, the development of a crude flow model to predict the differences seemed futile. With the realization of the limitations of the sloshing tank apparatus in not being able to simulate higher period parameters, the pendulum apparatus was developed. Since the Type II baffles had proved to be quite disappointing in the sloshing tank experiments, they were not tested in this apparatus, but all effort was concentrated upon Types I and III. Thus this study has, in seven months, produced adequate experimental information for the optimization of flexible baffles in rectangular and circular tanks (this optimization is reported in Sec. 3) and definitive flow visualization information to further the study of the fluid mechanics of the separated flow problem.

### 2.5.1 The Physical Phenomenon

The classical example of separated flow is the steady two-dimensional flow behind a circular cylinder. This is well discussed by Goldstein (p. 62, Ref. 16). At very small Reynolds numbers ( $Re \ll 1$ ), a viscous flow called Stokes' flow has fore-and-aft symmetry. At slightly higher speeds a wake forms (Oseen flow), and a

separation occurs essentially at the downstream stagnation point. At  $Re \approx 25$  two symmetric, stationary vortices exist. At higher Reynolds numbers these vortices become asymmetric, then alternately shed in a von Karman vortex street ( $Re \approx 70$ ). The sharp corners of the perpendicular flat plate cause large velocities in this region even at very small free stream velocities, so the regime of two symmetric vortices can no doubt occur at a smaller Reynolds number. Plates 33 and 34 of Ref. 16 show the separated flow in the range  $800 < Re < 8000$ . A splitter plate on the line of symmetry can considerably delay the vortex shedding process, as is discussed later.

When a symmetric bluff body is accelerated from rest to some constant velocity, the Stokes and Oseen flows are quickly replaced by boundary layer formation and separation with the separated boundary layer (a diffused vortex sheet) feeding vorticity into the center region of the vortices. If the Reynolds number of the steady flow is in the region of the two symmetric vortices as the maximum velocity is reached the separated flow shear layer will quit feeding its vorticity into the vortex center and any excess vorticity will either be cancelled or convected on downstream. If the steady-state Reynolds number is greater, vortex shedding can be expected.

We now consider the physical phenomena and the effect of each of the dimensionless parameters of the dimensional analysis of Sec. 2.1. For sinusoidal motion of geometrically similar bodies in an incompressible, infinite fluid, the period parameter is added to the Reynolds number as an independent dimensionless quantity. In this report the notation of Keulegan and Carpenter (Ref. 2) for period parameter,  $UT/D$ , is followed, but with  $D$  equal to one-half the total plate width (or the width of the plate if mounted to a wall). It is often more convenient to consider this parameter as the ratio of the distance traveled by the free stream during a half cycle, multiplied by  $2\pi$ , to this plate half-width,  $2\pi x_0/D$ . Two distinct flow regimes, denoted here as Regimes 1 and 2, and the asymmetric transition flow between these regimes were described in Sec. 2.4.3 and depicted in Fig. 50. In Regime 1 the vortices travel away from the plate in a vortex street perpendicular to the direction of the plate motion. The net fluid motion is a symmetric flow inward along the center

line toward the baffle and away from the baffle with the vortices. In Regime 2 the net fluid motion is in the opposite direction as each vortex which forms is swept across the top of the baffle and away from the baffle along the center line. At lower period parameters than those tested, of the orders of 0.01 and 0.1, the flow would not be expected to change greatly from the Regime 1 as presented in the flow visualization, the vortices simply being smaller. At larger period parameters than those obtained here and at moderately high Reynolds numbers, there must eventually be a transition from the Regime 2 flow to a periodic and/or unsteady vortex shedding case, a Regime 3.

Regime 3 will be delayed, and possibly completely prevented if splitter plates are present. Roshko (Ref. 8) compares the base pressure in the range  $5,000 < Re < 17,000$  for a perpendicular flat plate in a steady free stream flow with and without a splitter plate. The splitter plate was the same length as the perpendicular plate, but its leading edge was three lengths downstream. The difference between the free stream and base pressures for the splitter plate case was about 60% of that for the case with no splitter. While there was no accompanying flow visualization, it is highly suspected that this difference is caused by the shedding of vortices for the geometry with no splitter plate, but no shedding with this plate.

In Regime 1 the plate is always traveling through fluid unaffected by viscous action. However, in Regimes 2 and 3 the viscous fluid motion caused by the diffusion of the vortices is deposited along the centerline of the perpendicular plate and main motion. While its net motion is away from the plate this fluid which has been affected by viscosity does not move away fast enough at the higher period parameters, so the plate moves back and forth through its own wake. This increases the relative velocity that the plate experiences, increasing the drag and resulting losses. This is shown in the schematic, Fig. 50a.

Specifying the period parameter for a given body in sinusoidal motion still leaves the period of the cycle and the fluid properties unstated. These are combined in the

Reynolds number. It is instructive to consider the effect of Reynolds number at a constant period parameter in each flow regime for the perpendicular plate with and without splitter plates. Holding  $UT/D$  constant while varying  $Re = UD/\nu$  only allows  $\nu$  and  $T$  to vary. Determination of the period of the cycle determines the forces due to the virtual mass effect, so the Reynolds number plays an additional role in a periodic flow. For a given fluid, period parameter and body, increasing the Reynolds number results in increased forces due to virtual mass. Discussion of this effect is deferred until later.

The Reynolds number effect considered here is the usual steady state effect, which is best considered as the ratio of convection to diffusion of vorticity. This is expected to have a very small influence on the flow in Regime 1. It determines the amount of viscous diffusion in the vortex sheets emanating from the baffle tip, but this diffusion has only a slight effect on the dynamics of the quasi-steady flow. Addition of the splitter plate thickens the boundary layer at the baffle tip, and will only have a major effect if the splitter plate is so long that the baffle is completely submersed in the boundary layer. In Regimes 2 and 3 the viscous effect of Reynolds number is expected to be more pronounced, either with or without the splitter plate, since it determines the diffusion of the wake.

We consider next the effects of plate flexibility upon the physical phenomena. Only the forces acting on the plate due to the instantaneous flow field, and not those due to the acceleration, are examined here. Steady potential flow theory nicely accounts for the lift of an airfoil with the concept of the bound vortex. Only the strength of this vortex is needed, not the positioning, to determine the lift. A symmetric bluff body in a potential flow has no bound vorticity and the drag is determined by knowledge of the strength and position of all vorticity. Thus the two obvious ways for the flexible plate to have greater forces and create greater energy losses (still considering only the instantaneous effect) is to create more vorticity and deposit it closer to the plate so that it will have a greater effect on the pressure distribution of the plate. The vorticity generated at the plate edge is the amount needed to prevent infinite

velocities at the baffle tip, and is roughly proportional to the square of the free stream velocity but is affected by all the vorticity previously shed. It was seen in Sec. 2.4 that baffle tip can be out of phase with the main motion, so its relative tip velocity can be considerably greater than that for the rigid baffle. This is a mechanism for generating greater amounts of vorticity. Furthermore, it appears that the motion of the flexible baffle can cause the rolling up vorticity to come closer to the baffle than otherwise possible. At each period parameter there is a flexibility which will create the greatest flow losses, this optimum flexibility increasing with decreasing period parameter. When the flexibility is greater than the optimum it appears that the vorticity rolls up into a vortex further removed from the baffle than optimum.

### 2.5.2 The Pendulum Apparatus and Its Results

The size of this apparatus was basically determined by the bars which clamped the flexible baffle. Since the minimum feasible width was about 1/4-inch, the baffle needed to be about 2 in. wide so that this thickness would have negligible effect. To reduce end effects the length of the baffle was made the full width of the tank, and the radius of curvature was made reasonably large to keep its effect to a minimum. To obtain reasonably large period parameters with this arrangement without too great a decay rate in the amplitude then required as much weight on the pendulum as the apparatus could bear. Knife edges with their extremely low losses were tried, but the high contact stresses greatly limited this weight, so ball bearings were substituted.

A pendulum apparatus for determining oscillating flow losses has the great advantages over a sloshing tank type of apparatus of low parasitic losses and highly accurate energy determination. It does have disadvantages which are best discussed by adding more dimensionless parameters to the basic case of Sec. 2.1. The pendulum apparatus can be characterized by two additional quantities, the radius arm that the baffle rotates about,  $R_B$ , and the rate of decrease of the pendulum energy, a quantity which is inversely proportional to the pendulum weight times the radius arm to the

center of gravity,  $(WR)_{CG}$  (assuming parasitic losses are small). The radius of curvature effect is best made a dimensionless parameter as the ratio of the maximum amplitude to the arm radius,  $UT/2\pi R_B$ , denoted the curvature parameter, so that any correction factor for this effect goes to zero as the radius arm goes to infinity and the motion truly becomes linear. The damping of the pendulum energy results in the baffle motion being a damped sinusoid instead of the ideal undamped motion. Thus it is desired to have as the dimensionless ratio the amplitude decrement of the baffle motion. Taking the baffle length to be  $\lambda$ , this is derived as follows. The energy change per cycle (see Eq. 2.3):

$$(WR)_{CG} \Delta\left(\frac{\theta}{2}\right) = \lambda C_L \rho U^3 T (2D)$$

and since  $R_B \theta = 2\pi UT$ :

$$\frac{\Delta\theta}{\theta} = \frac{\rho U D \lambda C_L R_B^2}{2\pi^2 (WR)_{CG} T}$$

This is denoted as the damping parameter.

It is expected that the curvature and damping parameters are principally responsible for the variation of  $C_L$  at a given  $UT/D$  for the 2- and 4-in. baffles in Fig. 20a, and these two parameters, plus the splitter plate effect, in Fig. 21b. The Reynolds number only varies by a factor of two, so its effect is expected to be very small. The table below indicates the range of values for the curvature and damping parameters for 2- and 4-in. rigid baffles.



<u>2D</u>	<u>UT/D</u>	<u>2</u>	<u>6</u>	<u>30</u>
2	$UT/2\pi R_B$	0.0087	0.026	0.13
4	$UT/2\pi R_B$	.017	.052	
2	$\Delta\theta/\theta$	.020	.039	.091
4	$\Delta\theta/\theta$	.13	.21	

At a given  $UT/D$  , the smaller the baffle the smaller are the curvature and damping parameters, thus the 2-in. baffle results in Fig. 20a, which are 10 to 15% less than the 4-in. baffle loss coefficient, must be taken as the more correct values.

We consider next the expected effect of the variation of the curvature and damping parameters in the light of the present understanding of the physical phenomenon. In Regime 2 as the curvature parameter becomes large the wake fluid will become much more widely spread since the momentum of the fluid of each element in the wake will tend to carry it in a straight line, not the arc that the baffle travels through. The viscous fluid can be expected to move into an arc of greater radius of curvature, as depicted in Fig. 50b. What effect this will have on  $C_L$  is not obvious. Since the maximum relative velocity created by the baffle passing through its own wake (see previous discussion) appears to be reduced, it might be expected that the  $C_L$  would be decreased. However, it would also seem reasonable that the baffle now gradually pumps fluid downward in the maximum amplitude regions, in which case the entire area below the baffle soon is filled with fluid which was formerly of the wake, and this may be recirculated back into the immediate vicinity of the baffle as shown in the schematic in Fig. 50c. This effect may cause a greater asymmetric flow. Besides that effect, a more obvious one is that the edge of the plate further from the axis generates more vorticity and more losses. For instance, if the plate width is 10% of the radius arm, then the far edge of the plate travels 10% faster and may be capable of creating 30% more losses (energy losses are proportional to the velocity to the third power at a given period parameter) and 20% more vorticity. It is reasonable to assume that the vortex trailing this half of the plate will be larger than that trailing the inner half. This asymmetric vortex pattern may cause greater losses

than the symmetric case, as this seems to be the result from Roshko's data (Ref. 8) for the steady state case. Such asymmetric flow could also greatly change the period parameter at which transition from Regime 1 to Regime 2 occurs. Further testing changing only one parameter at a time is needed to verify these hypotheses. In Regime 1 flow, much less effect should be expected with variation of the curvature parameter.

Considering the effect of a large damping parameter on Regimes 2 and 3 flow at small values of the curvature parameter, higher  $C_L$  would be expected since the added relative velocity due to the wake flow would be larger. This is so because in the former cycle the velocity was greater. Thus a smaller damping parameter in these tests would have resulted in smaller  $C_L$  values. Again, what effect the damping parameter would have on the flow in Regime 1 is not obvious, and so is expected to be small.

Examining Fig. 20a, a 20% discrepancy exists between the present 2-in. rigid baffle and earlier tests, those of Martin (Ref. 7) which agree very well with those of Keulegan and Carpenter (Ref. 2). Martin tested 0.625, 1.0, 1.25, 1.75, and 2.5 in. baffles. Above  $UT/D$  the data are quite consistent for  $UT/D > 15$  except for the 0.625-in. baffle which is as much as 15% low. Below  $UT/D$  of 15 considerable scatter occurs, but his curve fit (which has been transposed onto Fig. 20a) generally follows the lower values of  $C_L$ . His 1.25-in. baffle closely follows his curve and is considered further here. His short radius arm of 10.7 in. results in a curvature parameter of 0.11 at  $UT/D = 6$ . This is more than four times greater than in the present tests with a 2-in. baffle. His damping ratio at this  $UT/D$  is 0.0078, considerably below that of the present apparatus. The only obvious reason for the discrepancy between these results and those of Martin is in the curvature term. A more ideal, lower damping ratio in the present tests would cause lower  $C_L$ 's, as discussed above, increasing the discrepancy. A small correction for damping ratio effect could be expected for the present data for  $UT/D > 25$ , which will tend to make this curve more similar to the former ones.

More minor effects to be considered which might be responsible for some error with this type of apparatus are: variation of the velocity wave shape due to nonlinear effects of large deflection angle and changing damping coefficient, and effects on the baffle, water surface effect, and tank size. At  $UT/D = 6$  the angular deflection of the present apparatus and Martin's are 1 and 3.5 deg, respectively. Even this larger value will cause an exceedingly small effect on the wave shape. As for the nonlinear damping effect, it must be small when the damping is small and the moment of inertia as large as it is here. The length-to-width ratio of the baffle in the present apparatus and Martin's are large, 18:1 and 9.8:1, respectively. Both baffles come very close to side walls to reduce end effects. The end correction should be considerably less than that determined by Ridjanovic (Ref. 17) at these aspect ratios as his plates ended far from the walls. In fact, he plots Martin's result as his infinite length-to-width case. In the present test the baffle was 25 in., or 25D from the surface, and in Martin's apparatus, this dimension is 10 in., or 20D. In these tests any surface wave was allowed to decay to a very low level (1/4-in.) before the test was started. No effect of the baffle on the surface was noted in the present tests. This is important because if the baffle had created a wave, this would have represented energy obtained from the baffle for future dissipation. Since the baffle does cause a net flow about itself, a mean circulation pattern must exist, the ejected wake flow mixing with surrounding fluid and eventually being sucked back around the baffle. The tank size must be large enough so that this wake flow does have adequate time for complete mixing. Both the present tank and Martin's channel are more than adequate in size.

The motion about the splitter plates is completely different when the baffle is removed, the skin friction decreasing and possibly a form drag appearing, the parasitic loss calibration was performed without these bars. The losses measured actually include the skin friction effect of these bars, which is negligible. The effect of splitter plate length as shown in Fig. 20b is inconclusive as the 8-in. splitter plates could not be mounted symmetrically enough to completely prevent a new lateral swaying of the baffle during the test.

### 2.5.3 The Sloshing Tank Apparatus and Its Results

The only reason these data are included is to show the relative effect of the Type II baffles tested. The discrepancy between the loss coefficients obtained from the sloshing tank and pendulum apparatuses is so great as to make one immediately suspect the data reduction technique. This has been carefully checked. The error must be mainly due to two causes: effect of the baffle on the surface wave, and the effective free stream velocity being improperly chosen.

The baffle size that could be used in this tank was severely limited. The losses from a half-inch baffle were too small compared to the parasitic losses. A one-inch baffle seemed like a good compromise size, but it did cause some surface wave effect which was overlooked at the time of the tests. This wave perturbation could store appreciable amounts of energy, causing some of the error. The velocity error is expected to be more important. The velocity that was used in the data reduction was that which would exist at the baffle tip if the baffle were not there. A similar assumption was used by Keulegan and Carpenter (Ref. 2). What is really desired though, is the free stream velocity that would cause the same effect if there were a semi-infinite amount of fluid about the baffle. The baffle and the resulting vortices did create disturbances for several inches about the baffle, and so it may be possible that the effective velocity is only 70 or 80% of that used. This effect would be greatly magnified by the  $U^3$  term in  $C_L$ . It is not expected that this  $C_L$  discrepancy devaluates the flow visualization, other than that the performance parameters listed may be 20 or 30% too large.

### 2.5.4 Flow Model Considerations

As a body is accelerated in an inviscid fluid (no vortex shedding allowed) greater potential velocities are required of the fluid near the body, thus increasing the energy of the fluid. The body must perform the work to add the energy to the fluid. The extra force required to do this work appears as if the body has a greater mass, and this is called the virtual mass. When the body decelerates to its original velocity

this extra kinetic energy is simultaneously returned to the body. Thus the force associated with the virtual mass cannot directly cause any damping to a body oscillating periodically (see Ref. 18, Chap. 6, or Ref. 19, Chaps. 3 and 17). If the fluid cannot transfer the energy back to the body this energy must be converted into energy associated with the viscous losses. To analytically determine permanent energy loss from a body as compared to a temporary energy exchange between the body and fluid) the instantaneous forces due to skin friction, a viscous action, and pressure determined from the potential flow and vorticity distribution, treating the flow as if it were quasi-steady, must be determined. For a body with separated flow, such as the perpendicular plate, the geometry of the potential flow is continually changing. This would cause changes in the virtual mass even if the plates were not accelerating. It is impossible to separate the virtual mass force and the force to be associated with permanent energy losses a priori. However, this should not detract from the efforts of McNown (Refs. 10 and 11) and Keulegan and Carpenter (Ref. 2) to divide the forces between these effects, as the force was their main interest, not flow losses, and this division did help McNown (Ref. 10) to obtain an interesting analytical-empirical flow model for determining the forces.

In Regime 1 the action of viscosity in diffusing vorticity is not expected to be important unless the Reynolds number is very small, so an inviscid flow assumption is reasonable. The ideal inviscid flow model would allow vorticity to emanate in a vortex sheet from the baffle tip and roll up into vortices, these vortices, the vortex sheet and potential motion all helping to determine the rate of vortex shedding to keep the velocity tangential at the baffle tip. To evaluate the flow with this type of model would require a finite difference computer program. Such a flow model should predict both Regimes 1 and 2. A simpler model should be adequate, however, for Regime 2. During most of the cycle in this regime, all but during the low velocity part of the cycle, two symmetric vortices are located just downstream of the plate essentially as in the flow model proposed by Foppl for the steady flow (See Ref. 20, p. 263). His model, two concentrated vortices which are stationary, was a poor one for the steady flow case since the vorticity is diffused almost uniformly throughout the closed wake region. Here, though, at reasonably large Reynolds numbers the vorticity may be well approximated as a concentrated vortex.

## Section 3

EFFICIENCY AND OPTIMIZATION ANALYSIS OF TWO-DIMENSIONAL  
AND CIRCULAR BAFFLES

Two problems are considered in this section:

- Determination of the baffle efficiency
- Design of a baffle of least possible weight for a given damping ratio

The analysis is performed for three different baffle configurations (see also Figure 51):

- Ring baffle in a circular cylindrical tank with lateral slosh
- Ring baffle in a circular cylindrical tank with axisymmetric slosh
- Two-dimensional rectangular tank with lateral slosh

The main ingredients of the analysis are the model characteristics of the sloshing motion and the structural and hydrodynamic characteristics of the baffle. These items will first be briefly discussed, and then synthesized into an expression for the baffle efficiency.

Only cantilevered baffles operating at period parameters above approximately 1 are treated.

## 3.1 MODAL CHARACTERISTICS OF SLOSHING MOTION

Below are given results based on solutions to Laplace's equation for incompressible, non-viscid, irrotational flow. The method of solution is analogous to that used by Lamb [(14), p. 285].

### 3.1.1 Circular Cylindrical Tank: Lateral Slosh

Miles (1) has given modal characteristics for the fundamental mode of lateral slosh. His results that are of interest in the present context follow:

Modal frequency

$$\omega^2 = 1.84 \frac{g}{a} \quad (3.1)$$

Total kinetic energy of motion

$$E_t = 0.553 \rho g a^2 \xi_1^2 \quad (3.2)$$

### 3.1.2 Circular Cylindrical Tank: Axisymmetric Slosh

For axisymmetric motion the modal velocity potential satisfying the differential equation and all boundary conditions is

$$\phi_n(r, z, t) = \xi_1 \frac{a \omega_n}{k_n a} \frac{J_0(k_n r)}{J_0(k_n a)} \frac{\cosh [k_n (z + h)]}{\sinh k_n h} \cos \omega_n t \quad (3.3)$$

where parameter  $k_n$  is determined by

$$J_1(k_n a) = 0 \quad k_n a = 3.8317, 7.0156, \dots \quad (3.4)$$

and the modal frequency  $\omega_n$  is given by

$$\omega_n^2 = \frac{g}{a} k_n a \tanh k_n h \quad (3.5)$$

Vertical velocity of the liquid at any point is given by

$$U_z = \frac{\partial \phi}{\partial z} = \xi_1 \omega_n \frac{J_0(k_n r)}{J_0(k_n a)} \frac{\sinh k_n(z+h)}{\sinh k_n h} \cos \omega_n t \quad (3.6)$$

The kinetic energy of the motion is found from [(14), p. 46].

$$E_T = \frac{\rho}{2} \int_S \phi_n \frac{\partial \phi}{\partial n} ds \quad (3.7)$$

Since the normal derivative  $\partial \phi_n / \partial \eta$  is zero on the cylindrical walls and bottom of the tank, the integration extends over the liquid free surface only

$$\begin{aligned} E_T &= \pi \rho \int_0^a \left( \phi_n \frac{\partial \phi_n}{\partial \eta} \right)_{z=0} r dr \\ &= \frac{\pi}{2} \rho \xi_1^2 \frac{a^3 \omega_n^3}{k_n a} \coth k_n h \cos^2 \omega_n t \end{aligned} \quad (3.8)$$

For the fundamental mode of axisymmetric slosh, the maximum kinetic energy is

$$E_T = \frac{\pi}{2} \rho g a^2 \xi_1^2 \quad (3.9)$$

### 3.1.3 Two-Dimensional Rectangular Tank: Lateral Slosh

The velocity potential in this case is

$$\phi_n(x, z, t) = \xi_1 \frac{a \omega_n}{k_n a} \sin k_n x \frac{\cosh k_n(z+h)}{\sinh k_n h} \cos \omega_n t \quad (3.10)$$



where  $k_n$  is given by

$$\cos k_n a = 0 \quad k_n = \frac{(2n - 1) \pi}{2a} \quad (3.11)$$

and the frequency by

$$\omega_n^2 = \frac{g}{h} k_n h \tanh k_n h \quad (3.12)$$

Vertical velocity of the liquid is

$$U_z = \xi_1 \omega_n \sin k_n x \frac{\sinh k_n (z + h)}{\sinh k_n h} \cos \omega_n t \quad (3.13)$$

Finally the kinetic energy determined as above is

$$E_T = \frac{1}{(2n - 1) \pi} \rho \xi_1^2 a^2 L \omega_n^2 \coth k_n h \cos^2 \omega_n t \quad (3.14)$$

For the fundamental mode of lateral slosh ( $n = 1$ ), the maximum kinetic energy is

$$E_T = \frac{1}{4} \rho g 2a L \xi_1^2 \quad (3.15)$$

### 3.2 STRESSES AND DEFLECTIONS

The maximum stress and tip deflection were calculated for the baffle configurations under consideration by using small-deflection theory. The results are summarized in Figures 52 through 55. Two loading cases were considered: uniform loading over the baffle width  $D$  and concentrated line load at the baffle tip. These cases are assumed to be possible extremes; no effort was made in the present investigation to determine actual load distributions across the baffle width.

The baffle flexibility parameter,  $F_A$ , as defined earlier in this report, is proportional to the tip deflection. But since the tip deflection is expressed differently depending on the loading and the baffle geometry it is necessary to redefine the flexibility parameter, so that it can be used for an arbitrary baffle configuration, as well as for the straight baffles used in the present series of tests. Thus, the flexibility is redefined as

$$F_A = \left(\frac{D}{t}\right)^3 \left(\frac{D}{T}\right)^2 \frac{1 - \nu^2}{E} \rho f\left(\frac{b}{a}\right) \quad (3.16)$$

where

$$f\left(\frac{b}{a}\right) = \frac{\text{Tip deflection - curved baffle}}{\text{Tip deflection - straight baffle}}$$

The function  $f\left(\frac{b}{a}\right)$  is shown graphically in Figure 56.

### 3.3 DETERMINATION OF AN EMPIRIC-ANALYTIC EXPRESSION FOR THE LOSS COEFFICIENT $C_L$

In the initial review of the anticipated problems associated with a baffle efficiency analysis, it was realized that an analytic or empiric-analytic approach rather than a purely numerical one would be advantageous, particularly from a point of view of determining meaningful trends. The experimental curves of  $C_L$  vs  $(UT/D)$ , Fig. 18, were fit exceedingly well with the function

$$C_L = A\left(\frac{UT}{D}\right)^B - J \exp\left(-E\frac{UT}{D}\right) + H \exp\left[-1/\left(G\frac{UT}{D}\right)^2\right] \quad (3.17)$$

$A$ ,  $B$ ,  $E$ ,  $J$ ,  $G$ , and  $H$  are the functions of flexibility shown in Figs. 57, 58, and 59. Values from this curve fit are plotted in Fig. 18. Values from this expression at

period parameters of 2, 4, 6, 10, 15, and 30 determined the curves drawn in the cross plot,  $C_L$  vs  $F$ , Fig. 19. The first term in Eq. (3.17) represents a straight line tangent to the  $C_L$  vs  $UT/D$  curves in the region of  $UT/D = 9$ . The second term is a correction for the lower period parameters and the third term, a correction for the higher period parameters.

### 3.4 BAFFLE EFFICIENCY

#### 3.4.1 Circular Cylindrical Tank: Lateral Slosh

The energy loss per unit length of baffle per cycle is

$$\Delta E_b = C_L \rho D T U^3$$

or,

$$\Delta E_b = C_L \rho D T U_o^3 \cos^3 \theta \quad (3.18)$$

where  $U_o$  is the maximum velocity, assumed independent of  $r$ . It is assumed as in Mile's paper (1) that  $U_o$  can be written in the following form

$$U_o = \omega \xi_1 f(-d) \quad (3.19)$$

The depth function  $f(-d)$  may be written, for relatively large depths  $d$  as

$$f(-d) = \exp \left[ - (ka) \frac{d}{a} \right] \quad (3.20)$$

where  $ka = 1.84$  for the circular cylindrical tank with lateral slosh (1).

Integrating Eq. (3.18) around the baffle, using  $C_L$  of the form given in Eq. (3.17), the following equation for the mean rate of energy dissipation over one cycle results:

$$\frac{\overline{dE}}{dt} = \frac{E}{T} b = 2\rho(a+b) \frac{D^4}{T^3} P^3 [I] \quad (3.21)$$

where

$$[I] \equiv \left[ P^B A \int_0^{\pi/2} (\cos \theta)^{B+3} d\theta - J \int_0^{\pi/2} \exp(-PE \cos \theta) (\cos \theta)^3 d\theta + H \int_0^{\pi/2} \exp\left(-\frac{1}{P^2 G^2 \cos^2 \theta}\right) (\cos \theta)^3 d\theta \right] \quad (3.22)$$

where  $P$  is  $U_0 T/D$ , the period parameter based on the maximum velocity at the baffle at the position of maximum slosh amplitude. The damping ratio is

$$\gamma = \frac{T \frac{dE}{dt}}{4\pi E_T}$$

Substituting Eqs. (3.2), (3.18), (3.19) and (3.21) yields the damping ratio as a function of the slosh amplitude, flexibility and tank dimensions:

$$\gamma_s = \left( \frac{8\pi^2}{0.553} \right) \frac{\left( 2 - \frac{D}{a} \right) \left( \frac{D}{a} \right) \left( \frac{\xi_1}{a} \right) [f(-d)]^3}{\left( \frac{T^2 g}{a} \right)} \left[ \left( 2\pi \left( \frac{a}{D} \right) \left( \frac{\xi_1}{a} \right) f(-d) \right)^B A \int_0^{\pi/2} (\cos \theta)^{B+3} d\theta - J \int_0^{\pi/2} \exp \left[ -2\pi \left( \frac{a}{D} \right) \left( \frac{\xi_1}{D} \right) f(-d) E \cos \theta \right] (\cos \theta)^3 d\theta + H \int_0^{\pi/2} \exp \left\{ -1 / \left[ 2\pi \left( \frac{a}{D} \right) \left( \frac{\xi_1}{D} \right) f(-d) G \cos \theta \right]^2 \right\} (\cos \theta)^3 d\theta \right] \quad (3.23)$$

In the region where the second and third integrals are negligible, the expression is simply

$$\gamma_s = \frac{2(2\pi)^{2+B}}{0.553} \left(2 - \frac{D}{a}\right) \left(\frac{D}{a}\right)^{1-B} \left(\frac{a}{T^2 g}\right) \left(\frac{\xi_1}{a}\right)^{1+B} [f(-d)]^{3+B} \int_0^{\pi/2} (\cos \theta)^{B+3} d\theta \quad (3.23a)$$

For the rigid baffle case

$$A = 5.2$$

$$B = -0.67$$

$$\int_0^{\pi/2} (\cos \theta)^{B+3} d\theta = 0.739$$

The mathematical expression for the relative hydrodynamic efficiency of the flexible baffle is

$$\left(\frac{\gamma_s}{\gamma_{so}}\right)_1 = \frac{[I]}{[I_o]} \quad (3.24)$$

where

$$I_o \equiv \left[ P_o A_o \int_0^{\pi/2} (\cos \theta)^{B_o+3} d\theta - J_o \int_0^{\pi/2} \exp(-PE_o \cos \theta) (\cos \theta)^3 d\theta + H_o \int_0^{\pi/2} \exp\left(-\frac{1}{P^2 G_o^2 \cos^2 \theta}\right) (\cos \theta)^3 d\theta \right] \quad (3.24a)$$

A plot of  $(\gamma_s/\gamma_{s0})$  appears in Fig. 60. At a period parameter of 2 a baffle with optimum flexibility of  $10^{-2}$  is seen to be 67% more efficient than the rigid baffle. This is greater than the 42% increase found in the baffle tests (see Fig. 19) because the period parameter actually varies from 0 to 2 around the baffle (virtually all of the loss contributions is for  $1 < UT/D < 2$ ), and the lower the period parameter, the greater the relative efficiency has been found to be.

The baffle weight efficiency is expressed by the ratio

$$\eta_1 = \frac{S}{\left(\frac{W}{\gamma a^3}\right)} \quad (3.25)$$

The weight of the baffle is

$$\frac{W}{\gamma a^3} = \pi \frac{t}{D} \left(2 - \frac{D}{a}\right) \left(\frac{D}{a}\right)^2 \quad (3.26)$$

and the stiffness parameter is

$$F_A = 4.23 \times 10^{-2} \left(\frac{D}{t}\right)^3 \left(\frac{D}{a}\right)^2 \frac{gap}{E} f\left(\frac{b}{a}\right) \quad (3.27)$$

where

$$\frac{1.84}{4\pi^2} (1 - \nu^2) = 4.23 \cdot 10^{-2} \quad \text{for } \nu = 0.3$$

Combining Eqs. (3.23), (3.24), (3.26) and (3.27) yields

$$\left[ f\left(\frac{b}{a}\right) \right]^{1/3} \left[ f(-d) \right]^{-2} \left( \frac{ga\rho}{E} \right)^{1/3} \left( \frac{D}{a} \right)^{2/3} \eta_1 = 0.4842 (F_A)^{1/3} P\left(\frac{\gamma_o}{\gamma_{so}}\right) [I_o] \quad (3.28)$$

This modified weight efficiency parameter is plotted vs.  $F_A$  in Fig. 61. The effectiveness of flexible over the rigid baffles is amplified by the introduction of the weight factor. This is most pronounced at low period parameters where the maximum efficiency occurs at  $F_A \cong 5 \times 10^{-3}$ . Compared to a baffle which is only slightly flexible,  $F_A = 10^{-5}$ , the optimum baffle at  $UT/D = 4$  is nine times as efficient. This locus of maximum values is indicated with a dotted line and has been transposed onto Fig. 60.

### 3.4.2 Circular Cylinder Tank: Axisymmetric Slosh

By performing the same process the damping ratio and relative hydrodynamic efficiencies are determined as:

$$\gamma_s = 16\pi^3 \left(2 - \frac{D}{a}\right) \left(\frac{D}{a}\right) \left[ f(-d) \right]^3 \left( \frac{a}{gT^2} \right) \left( \frac{\xi_1}{a} \right) C_L \quad (3.29)$$

and

$$\left( \frac{\gamma_s}{\gamma_{so}} \right)_2 = \frac{C_{L_0}}{C_L} \quad (3.30)$$

where  $C_{L_0}$  is  $C_L$  determined at  $F_A = 0$ . This ratio,  $(\gamma_s/\gamma_{so})$  is plotted in Fig. 62.

The stiffness parameter for this configuration is given by

$$F_A = 8.93 \cdot 10^{-2} \left(\frac{D}{t}\right)^3 \left(\frac{D}{a}\right)^2 \left(\frac{ga\rho}{E}\right) f\left(\frac{b}{a}\right) \quad (3.31)$$

The efficiency equation is

$$\left[f\left(\frac{b}{a}\right)\right]^{1/3} \left[f(-d)\right]^{-2} \left(\frac{ga\rho}{E}\right)^{1/3} \left(\frac{D}{a}\right)^{2/3} \eta_2 = 0.557 (F_A)^{1/3} \left(\frac{U_o T}{D}\right) C_L \quad (3.32)$$

This modified weight efficiency parameter is plotted in Fig. 63.

### 3.4.3 Two-Dimensional Rectangular Tank: Lateral Slosh

For the two-dimensional rectangular tank case again

$$\frac{\gamma_s}{\gamma_{so}} = \frac{C_L}{C_{L_o}}$$

which is plotted in Fig. 62. For this case the rigid baffle damping ratio is

$$\gamma_{so} = \frac{\pi}{2} \left(\frac{D}{a}\right) \left(\frac{L}{a}\right) \left[f_1(-d)\right]^3 C_L$$

Here  $\eta$  is defined in a slightly different way than for cylindrical tanks

$$\eta_3 = \frac{\gamma_s}{\left(\frac{W}{\gamma a^2 L}\right)} \quad (3.33)$$

where  $L$  is the tank dimension perpendicular to the slosh direction.



where

$$F_A = 3.62 \times 10^{-2} \left(\frac{D}{t}\right)^3 \left(\frac{D}{a}\right)^2 \left(\frac{ga\rho}{E}\right) \quad (3.34)$$

and  $f_1(-d)$  as given by Keulegan (Ref. 2) is

$$u = \omega t \frac{\cosh k(Z+H)}{\cosh kH} \sin kx \cos \omega t - \frac{3}{4} \omega \frac{\xi^2}{a} \frac{\cos 2k(Z+H)}{\sinh^2 kH \sinh 2kH} \sin 2kx \sin 2\omega t \quad (3.35)$$

Using the same procedure as before we obtain

$$\left(\frac{ga\rho}{D}\right)^{1/3} [f_1(-d)]^{-2} \left(\frac{D}{a}\right)^{2/3} \eta_3 = 0.75 \left(\frac{UT}{D}\right) (F_A)^{1/3} C_L \quad (3.36)$$

Comparing with Eq. (3.29) we find

$$\eta_3 = 1.72 \left[f\left(\frac{b}{a}\right)\right]^{1/3} \eta_2$$

Thus Fig. 63,  $\eta_2$  vs.  $F_A$ , may be used for the rectangular tank configuration provided the ordinate values are multiplied by the coefficient to  $\eta_2$  in the above expression, and the proper flexibility be used.

### 3.5 BAFFLE WEIGHT OPTIMIZATION

With the information collected so far we now possess the necessary tools to make it possible to perform a baffle weight optimization. Before we start to optimize, however, we must make clear precisely what kind of a criterion we are using when we say that the baffle weight is optimized. In the above analysis the damping ratio to baffle weight factor,  $\eta$ , has been evaluated, thereby tacitly assuming that the damping should be part of the optimization criterion. But what damping? As we see in Figures 61 and 63 the damping is not a constant value for any particular baffle configuration; it varies with the period parameter  $U_0 T/D$ , which in turn varies with the slosh amplitude  $\xi_1$ , and, consequently, with time. We see, that in the lower region of the flexibility parameter  $F_A$  the damping decreases as the period parameter (or slosh amplitude) decreases, while for higher values of the flexibility parameter the damping increases with decreasing period parameters. At one point,  $F_A \sim 10^{-5}$ , the damping is nearly independent of  $UT/D$  for  $UT/D > 4$ . Thus, we have three regions of different baffle behavior and the question that must be answered before we attempt an optimization of the baffle weight is in which region do we want our particular baffle to operate? When this question is answered, others remain, such as number of baffles, whether the tank is emptying or not, etc. Instead of trying to answer these questions, or circumnavigate them by investigating all possibilities, we will, as an example, scrutinize a simplified case.

We make the following assumptions:

- Circular tank, lateral slosh
- One baffle
- Non-emptying tank
- Flexibility  $F_A = 1.1 \times 10^{-3}$ ,  $UT/D > 6$

The last assumption makes the baffle efficiency essentially independent of the period parameter, and, thus, of the slosh amplitude,  $\xi_1$ . (See Figure 61.) While, strictly speaking, we are leaving the flexibility parameter out of the picture, this is not a

serious omission, since, as is seen in Figure 61, the weight efficiency is not materially affected by rather large changes of  $F_A$  in this flexibility region. Thus, nothing material is omitted in the following discussion. With these four assumptions the problem can be written in the following form:

$$\left. \begin{aligned} (a) \quad \eta_1 &= 0.40 \left( \frac{E}{ga\rho} \right)^{1/3} \left( \frac{D}{a} \right)^{-2/3} [f(-d)]^2 \left[ f\left(\frac{b}{a}\right) \right]^{-1/3} \\ (b) \quad F_A &= 1.1 \times 10^{-3} \\ (c) \quad F_A &= 4.23 \times 10^{-2} \left( \frac{D}{t} \right)^3 \left( \frac{D}{a} \right)^2 \left( \frac{ga\rho}{E} \right) f\left(\frac{b}{a}\right) \\ (d) \quad \eta_1 &= \frac{\gamma_s}{(W/\gamma a^3)} \\ (e) \quad \frac{W}{\gamma a^3} &= \pi \left( \frac{t}{D} \right) \left( 2 - \frac{D}{a} \right) \left( \frac{D}{a} \right)^2 \end{aligned} \right\} \quad (3.37)$$

The constant in the first equation is from Figure 61. Combining these equations and approximating  $f(b/a)$  as  $(b/a)$  (see Figure 56), the following weight equation is obtained:

$$\frac{W}{\gamma a^3} = 1.23 \gamma_s^{4/3} \left( \frac{ga\rho}{E} \right)^{1/3} f[(-d)]^{2/3} \frac{R}{R_0} \quad (3.38)$$

where

$$R = \left[ \frac{1 - (D/a)}{2 - (D/a)} \right]^{1/3}$$

and  $R_0$  is the maximum value of this function, 0.793, when  $D$  is zero. The function  $R/R_0$  varies very slowly, i. e., for  $D/a = 0.3$ ,  $R/R_0 = 0.94$  and can

be considered as a small correction term. The damping ratio, as determined from Figures 60 and 64 for this flexibility, at  $UT/D = 10$  is

$$\gamma_s = 115 \left(2 - \frac{D}{a}\right) \left(\frac{D}{a}\right) \left(\frac{\xi_1}{a}\right) [f(-d)]^3 \left(\frac{a}{T_g^2}\right) \quad (3.39)$$

From inspection of Eq. (3.39) the following comments emerge:

- Baffle weight is proportional to the material parameter  $\gamma/E^{1/3}$ . This parameter is given below for some typical materials:

Material	$\gamma$ (lb/in. <sup>3</sup> )	E (lb/in. <sup>2</sup> )	$\frac{\gamma}{E^{1/3}}$ (lb) <sup>2/3</sup> (in.) <sup>-7/3</sup>
Magnesium	0.064	$6.5 \times 10^6$	$3.43 \times 10^{-4}$
Aluminum	0.100	$10 \times 10^6$	$4.63 \times 10^{-4}$
Titanium	0.160	$16 \times 10^6$	$6.35 \times 10^{-4}$
Steel	0.280	$30 \times 10^6$	$9.00 \times 10^{-4}$

- The baffle weight increases at a faster rate than the damping factor
- The closer to the surface the baffle is located, the lighter it is.

The methods employed in this analysis will not, however, adequately account for the rather complicated fluid motions that will develop if the baffle is located close to the fluid surface.

The actual baffle dimensions are found as follows, assuming known values of  $f(-d)$  and  $\gamma_s$ :

Baffle weight — Eq. (3.38)

Baffle width  $\frac{D}{a}$  — Eq. (3.39)

Baffle thickness  $\frac{t}{D}$  — Eq. (3.37c)

The baffle dimensions calculated in this manner will have to be checked for stress. This requires a knowledge of the actual load distribution on the baffle, information which was beyond the scope of the present work. Some preliminary computations, based on the assumption of linear proportionality between load and energy absorption indicate a stress relation of the following type

$$\sigma_{\max} = (gap) \times \left( \frac{E}{gap} \right)^{2/3} \times f(d, \xi_1, \gamma_s)$$

for the simplified case discussed here. This equation indicates a rather strong size effect, i.e., large tanks would be more severely strength-limited than smaller ones. However, the stress may be lowered without appreciable weight increases by decreasing the flexibility factor  $F_A$  (moving left in Figure 60).

# Section 4 LIST OF SYMBOLS

a	cylinder radius, half-width of rectangular tank; semiwave height of slosh, Section 3
A, B	functions of flexibility parameter, see Section 3
b	a - d
C	$A \int_0^{\pi/2} (\cos \theta)^{B+3} d\theta$
$C_D$	drag coefficient, $\frac{F}{\frac{\rho}{2} U^2 D}$
$C_L$	loss coefficient, $\frac{dE}{\rho U^3 T D}$
D	width of baffle mounted to a wall, half-width of a plate perpendicular to the direction of relative motion
$\Delta e$	change in total energy per cycle with no baffle in apparatus
E	total energy, Young's modulus of elasticity
$E_t$	total kinetic energy
$f\left(\frac{b}{a}\right)$	relative tip deflection, see Figure 55
$f(-d)$	depth function
F, $F_A$	flexibility parameter $\left(\frac{D - \delta}{t}\right)^3 \left(\frac{1 - \nu^2}{E}\right) \frac{\rho D^2}{T^2} f\left(\frac{b}{a}\right)$ where $f = 1$ in Section 2 and $\delta = 0$ in Sections 2.1, 2.2, and 3
g	acceleration due to gravity, length of travel of slamming baffle
H	depth of fluid in quiescent tank
k	torsional spring constant, $\pi/L$
L	length of rectangular tank

PE	potential energy per unit length
$r_{CG}$	radius to center of gravity of pendulum
$r_m$	radius to arc where pendulum deflection is read
$r, z$	cylindrical coordinates
S	length of splitter plate on each side of baffle
T	period of cycle
t	time, baffle thickness
u, v	velocity components in x, z directions
U, $U_0$	maximum velocity of periodic motion
W	pendulum weight; baffle weight (Section 3)
$x_0$	amplitude of periodic motion
x, z	rectangular coordinates
$\gamma$	specific weight of baffle material
$\gamma_s$	damping ratio, (logarithmic decrement)/ $2\pi$
$\gamma_{s_0}$	damping ratio, rigid baffle
$\Delta$	finite difference
$\xi_1$	maximum slosh amplitude
$\eta_1, \eta_2$	$\frac{\gamma_s}{\left(\frac{W}{\gamma a^3}\right)}$ , baffle weight efficiency, circular tank
$\eta_3$	$\frac{\gamma_s}{\left(\frac{W}{\gamma a^2 L}\right)}$ , baffle weight efficiency, rectangular tank
$\theta$	deflection angle of pendulum
$\mu$	viscosity
$\nu$	Poisson's ratio
$\rho$	fluid density
$\rho_0$	baffle density
$\omega$	modal, circular frequency

Subscripts:

BT	baffle tip
$\infty$	undisturbed by baffle
x	horizontal direction
z	vertical direction



Section 2  
REFERENCES

1. J. W. Miles, "Ring Damping of Free Surface Oscillations in a Circular Tank," J. Appl. Mech., Vol. 25, No. 2, June 1958
2. G. H. Keulegan and L. H. Carpenter, "Forces on Cylinders and Plates in an Oscillating Fluid," J. Res. NBS, Vol. 80, No. 5, May 1958
3. M. A. Silveira, David G. Stephens, and H. W. Leonard, "An Experimental Investigation of the Damping of Liquid Oscillations in Cylindrical Tanks," NASA, TN D-715, Langley Research Center, Langley Field, Va.
4. J. P. O'Neill, "Semianual Report on Experimental Investigation of Sloshing," Tr-59-0000-00713, Space Technology Laboratories, January 1-June 30, 1959
5. H. A. Cole, Jr. and B. J. Gambucci, "Measured Two-Dimensional Damping Effectiveness of Fuel-Sloshing Baffles Applied to Ring Baffles in Cylindrical Tanks," NASA, TN D-694, Ames Research Center, Moffett Field, Calif.
6. H. N. Abramson and L. R. Garza, "Some Measurements of the Effects of Ring Baffles in Cylindrical Tanks," J. Spacecraft, Vol. 1, No. 5, September-October 1964
7. Milton Martin, "Roll Damping Due to Bilge Keels," ONR Report, Contract Nonr 1611(01), November 1958
8. Anatol Roshko, "A New Hodograph for Free-Streamline Theory," NACA, TN 3168, California Institute of Technology
9. -----, "On the Drag and Shedding Frequency of Two-Dimensional Bluff Bodies," NACA, TN 3169, California Institute of Technology
10. J. S. McNown, "Drag in Unsteady Flow," The University of Michigan and the Sandia Corporation

11. J. S. McNown and C. H. Keulegan, "Vortex Formation and Resistance in Periodic Motion," Proc. Am. Soc. Civil Engrs., January 1959
12. Leo Anton, "Formation of a Vortex at the Edge of a Plate," NACA, TM 1398
13. J. E. Fromm, "A Method for Computing Nonsteady, Incompressible, Viscous Fluid Flows," LA-2910, Los Alamos Scientific Laboratory, Los Alamos, N.M.
14. Horace Lamb, Hydrodynamics, (sixth edition), Dover Publications, New York, 1932
15. F. A. Schraub, S. J. Kline, J. Henry, P. W. Runstadler, Jr., and A. Littell, "Use of Hydrogen Bubbles for Quantitative Determination of Time Dependent Velocity Fields in Low Speed Water Flows," Report Md-10, Department of Mechanical Engineering, Stanford University
16. Goldstein, "Modern Developments in Fluid Dynamics," Vols. 1 and 2, Oxford University Press, 1957
17. Muhamed Ridjanovic, "Drag Coefficients of Flat Plates Oscillating Normally to Their Planes," Schiffstechnik, Bd 9, Heft 45, 1964
18. G. Birkhoff, "Hydrodynamics," Princeton University Press, 2nd edition, 1960
19. Milne Thompson, "Theoretical Hydrodynamics," The Macmillan Co.,
20. Birkhoff and Zarantonello, "Jets, Wakes, and Cavities," Vol 2, Academic Press, Inc., 1957

# Appendix A RELATIONSHIP BETWEEN TYPES I AND II BAFFLES

Approach. Seek a relationship through baffle tip and strain energy considerations.  
Assume pressure distributions for Type I baffle.



(NOTE:  $L = D$  = Baffle height from text)

For small deflections, we calculate the strain energy to be for (a):

$$SE_{(a)} = \int_0^L \frac{M^2}{2EI} dx = \frac{Q^2 L^5}{2EI} (0.05) \quad (A. 1)$$

and for (b):

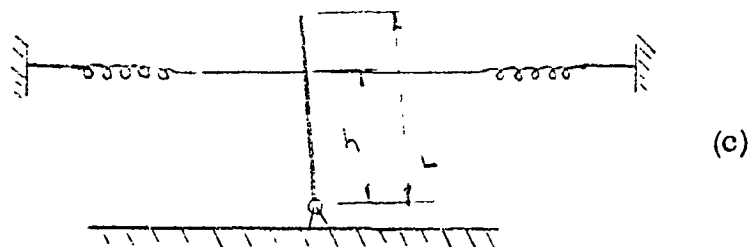
$$SE_{(b)} = \frac{P^2 L^5}{2EI} (0.0287) \quad (A. 2)$$

The deflection at L,

$$\delta_{(a)} = \frac{QL^4}{EI} \left( \frac{1}{8} \right) \quad (A. 3)$$

$$\delta_{(b)} = \frac{PL^4}{EI} \left( \frac{7}{72} \right) \quad (A. 4)$$

For Type II baffle the strain energy is



$$SE_{(c)} = 2 \int F dx = x^2 k = (hQ)^2 k \quad (A. 15)$$

The tip deflection is

$$\delta_{(c)} = L\phi \quad (A. 6)$$

Utilizing configuration (a), Eqs. (A. 1), and (A. 2) with  $h = \frac{L}{5}$  yield for the same tip deflection:

$$\frac{QL^4}{3EI} = \frac{5F}{k}, \text{ or } F = \frac{QL^4}{40EI} k$$

and for the same strain energy:

$$(0.05) \frac{Q^2 L^5}{2EI} = \frac{F^2}{k} = \frac{Q^2 L^8}{(40)^2 E^2 I^2} k$$

or

$$k = \frac{EI}{L^3} (40) \text{ lb/in.} \quad (A. 7)$$

Utilizing configuration (b), Eqs. (A. 3), and (A. 4) yield for the same

tip deflection:

$$\frac{PL^4}{EI} \left( \frac{7}{72} \right) = \frac{5F}{k} , \quad F = \frac{PL^4 7}{EI(5)(72)} k$$

and for the same strain energy:

$$\frac{P^2 L^5}{2EI} (0.0287) = \frac{F^2}{k} = \frac{P^2 L^8 (49)k}{E^2 J^2 (2s)(72)^2}$$

or

$$k = \frac{EI}{L^3} \frac{(25)(72)^2}{(96)} (0.0287)$$

$$k = \frac{EI}{L^3} 38.0 \text{ lb/in.} \quad (\text{A. 8})$$

Example. Given: A Type I, 1-in. 0.001 stainless steel baffle 12 in. long. The Type II baffle, having an equivalent amount of strain energy for the same baffle tip deflection, would have springs of

$$k_{1,2} = \frac{EI}{L^3} (38.0) \text{ located at } L/5 \text{ from the pivot point.}$$

In this case

$$L = 1 \text{ in.}$$

$$E = 30 \times 10^6 \text{ lb/in.}^2$$

$$\begin{aligned} I &= \frac{1}{12} (12) \left( \frac{1}{0.001} \right)^3 \\ &= 10^{-9} \end{aligned}$$

so

$$\begin{aligned} k_{1,2} &= (30)(38)10^6 \times 10^{-9} \text{ lb/in.} \\ &= (16)(30)(38)10^{-3} = 18.2 \text{ oz/in.} \end{aligned}$$

Alternately, for

$$\begin{aligned} I &= \frac{1}{12} bt^3 \\ b &= 12 \text{ in.} \\ L &= 1 \text{ in.} \\ t^3 &= \frac{k}{(38)E}, \quad k = \text{lb/in.} \end{aligned}$$

So flexibility for Type II baffles may be defined as,

$$F = \left(\frac{38}{k}\right) \left(\frac{1 - \nu^2}{T^2}\right) \rho$$

More generally,

$$\begin{aligned} k &= (38.0) \frac{EI}{D^3} \\ &= \frac{(38.0)}{(12.0)} bE \frac{t^3}{D^3} \end{aligned}$$

or

$$\left(\frac{D}{t}\right)^3 = \frac{(38.0) bE}{12}$$

and

$$F = \left(\frac{38}{12}\right) \frac{b}{K} \left(\frac{1 - \nu^2}{T^2}\right) \rho$$

# Appendix B

## ENERGY DETERMINATION FOR SLOSHING TANK APPARATUS

The object is to determine the energy of the system as a function of the maximum height of the surface profile.

Basically, at any time total energy = potential energy + kinetic energy.

From Ref. 14,

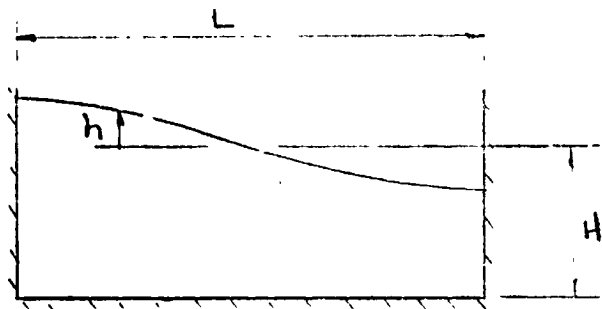
$$u = f(g, \text{geometry}, x, z) \cos w\tau - g'(g, \text{geometry}, x, z) \sin 2w\tau$$

And similarly for  $w$

$$\text{For } \tau = \frac{\pi}{2w}, \quad \cos w\tau = 0 = \sin 2w\tau$$

So kinetic energy = 0 . Total energy is, therefore, all potential at this time. Now at  $\tau = \frac{\pi}{2w} + \frac{nT}{2}$ ,

$$\frac{\text{Total Energy}}{\text{Ft (Tank Width)}} = \frac{\text{PE}}{w} = \frac{\rho g}{2} \left[ \int_0^L (h + H)^2 dx - H^2 L \right]$$



From Ref. 14,

$$(h + H) = a \cosh x + \frac{a^2 k}{4} (N_1 + N_2) \cos 2kx + H$$

So

$$\begin{aligned} \frac{\rho g}{2} \int_0^L (h + H)^2 dx &= \frac{\rho g}{2} \int_0^L \left[ a^2 \cos^2 kx + \frac{a^4 k^2}{16} (N_1 + N_2)^2 \cos^2 2kx + H^2 \right. \\ &\quad + \frac{a^3 k}{2} (N_1 + N_2) \cos kx \cos 2kx + 2aH \cos kx \\ &\quad \left. + \frac{a^2 kH}{2} (N_1 + N_2) \cos 2kx \right] dx \end{aligned}$$

and

$$\frac{PE}{W} = \frac{\rho g a^2 L}{4} \left[ 1 + \frac{k^2 a^2}{16} (N_1 + N_2)^2 \right]$$



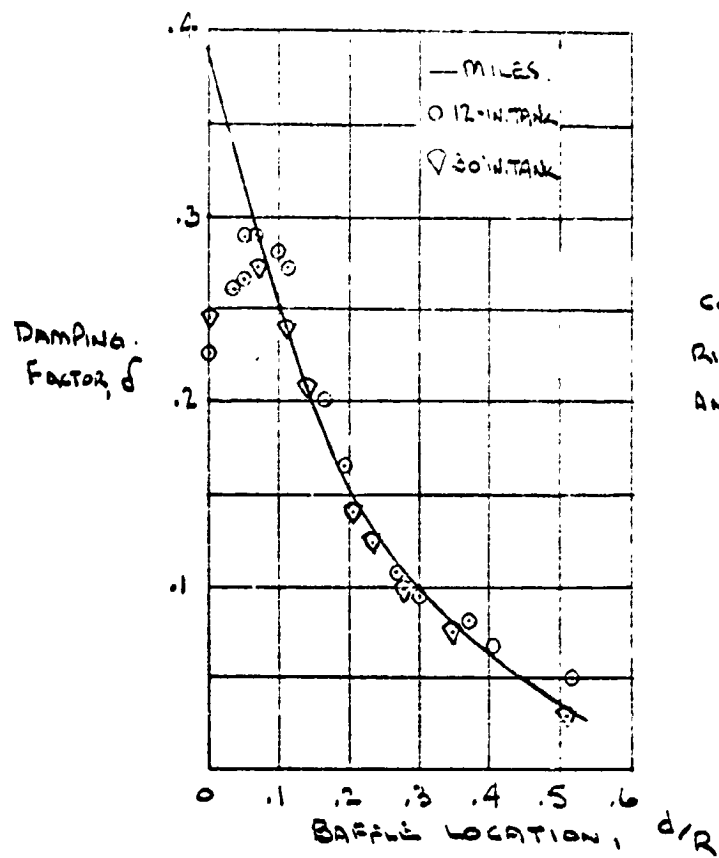
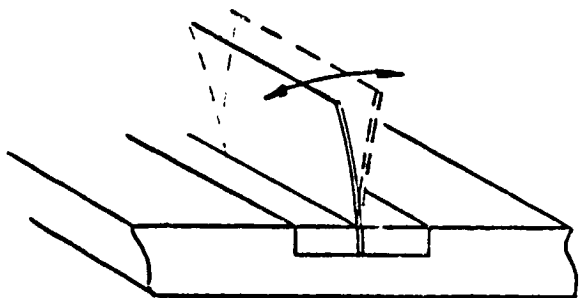
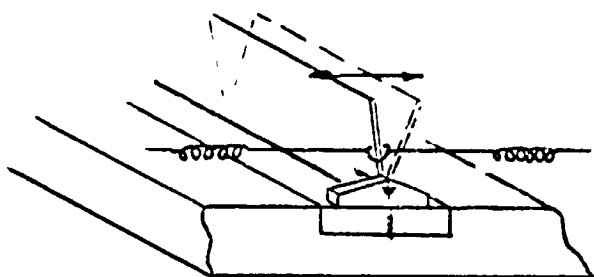


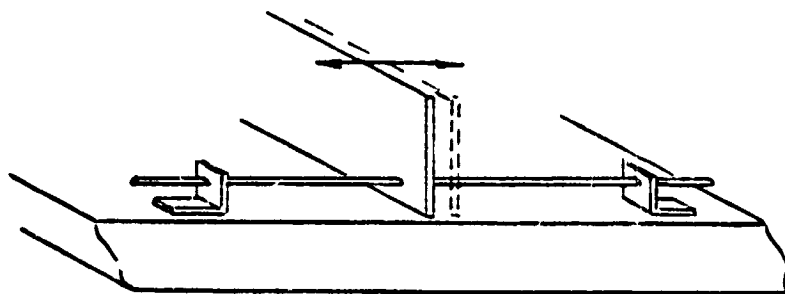
FIG. 1  
 COMPARISON OF EXPERIMENTAL  
 RIGID RING BAFFLE DAMPING  
 AND MILES' THEORY  
 (FIG. 10 OF REF. 3)



TYPE I, CANTILEVERED FLEXIBLE



TYPE II, HINGED - SPRING LOADED.

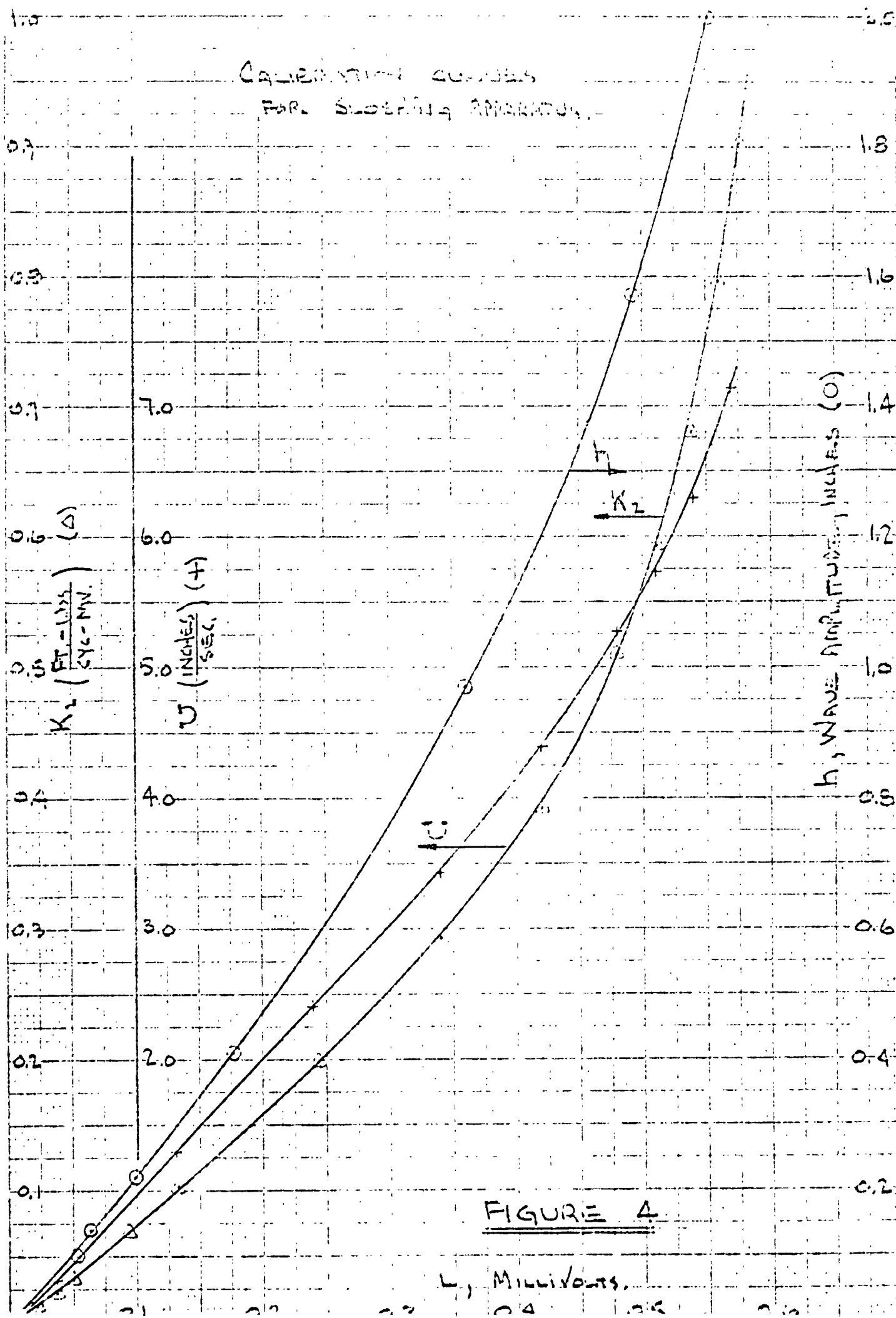


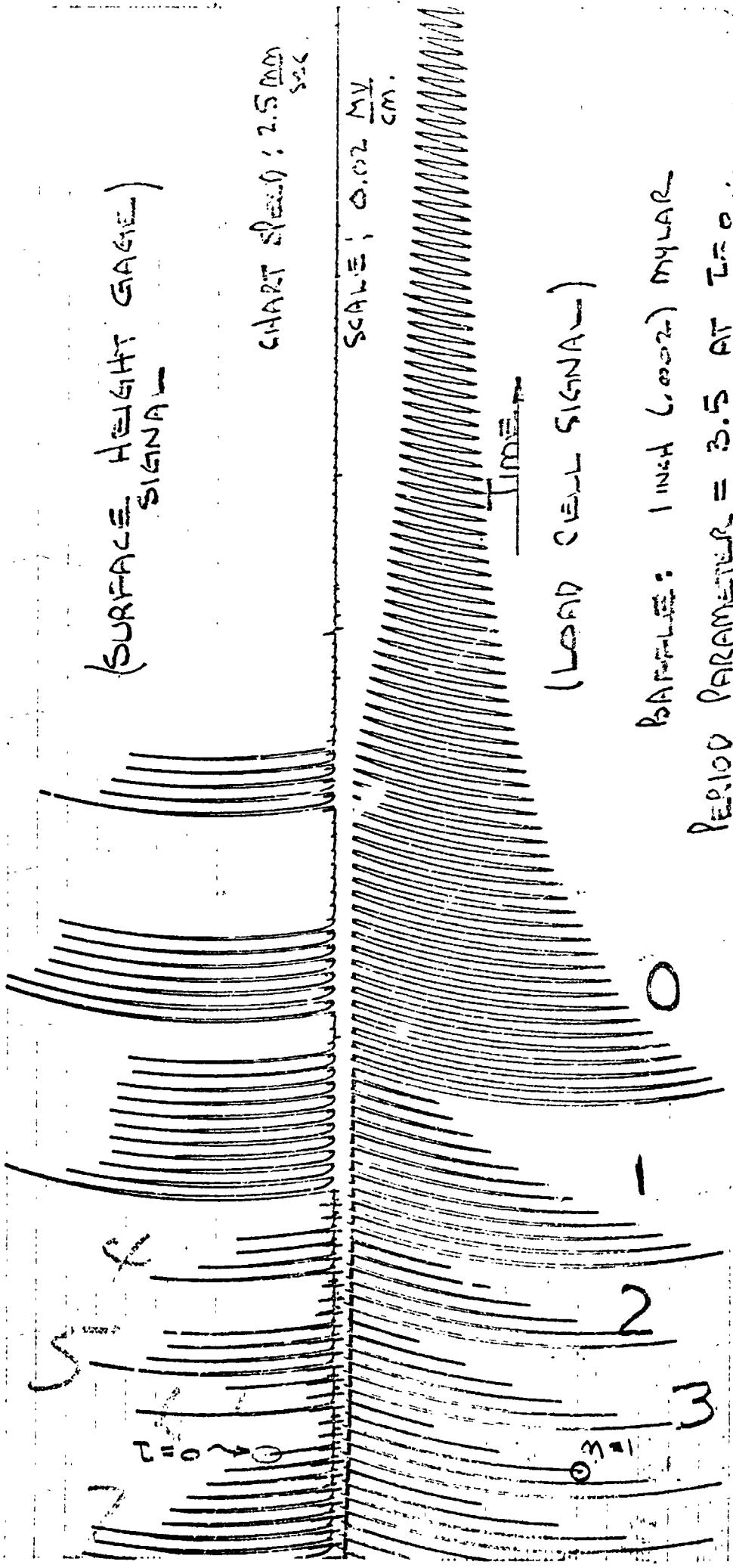
TYPE III, SLAMMING.

FIG. 2 THREE BAFFLE TYPES AS SUPPORTED IN  
 SLOSHING TANK APPARATUS



FIGURE 3 SLOSHING TANK ARRANGED FOR FLOW VISUALIZATION





SAMPLE OF OBTAINED DATA  
FOR SLOSHING TANK

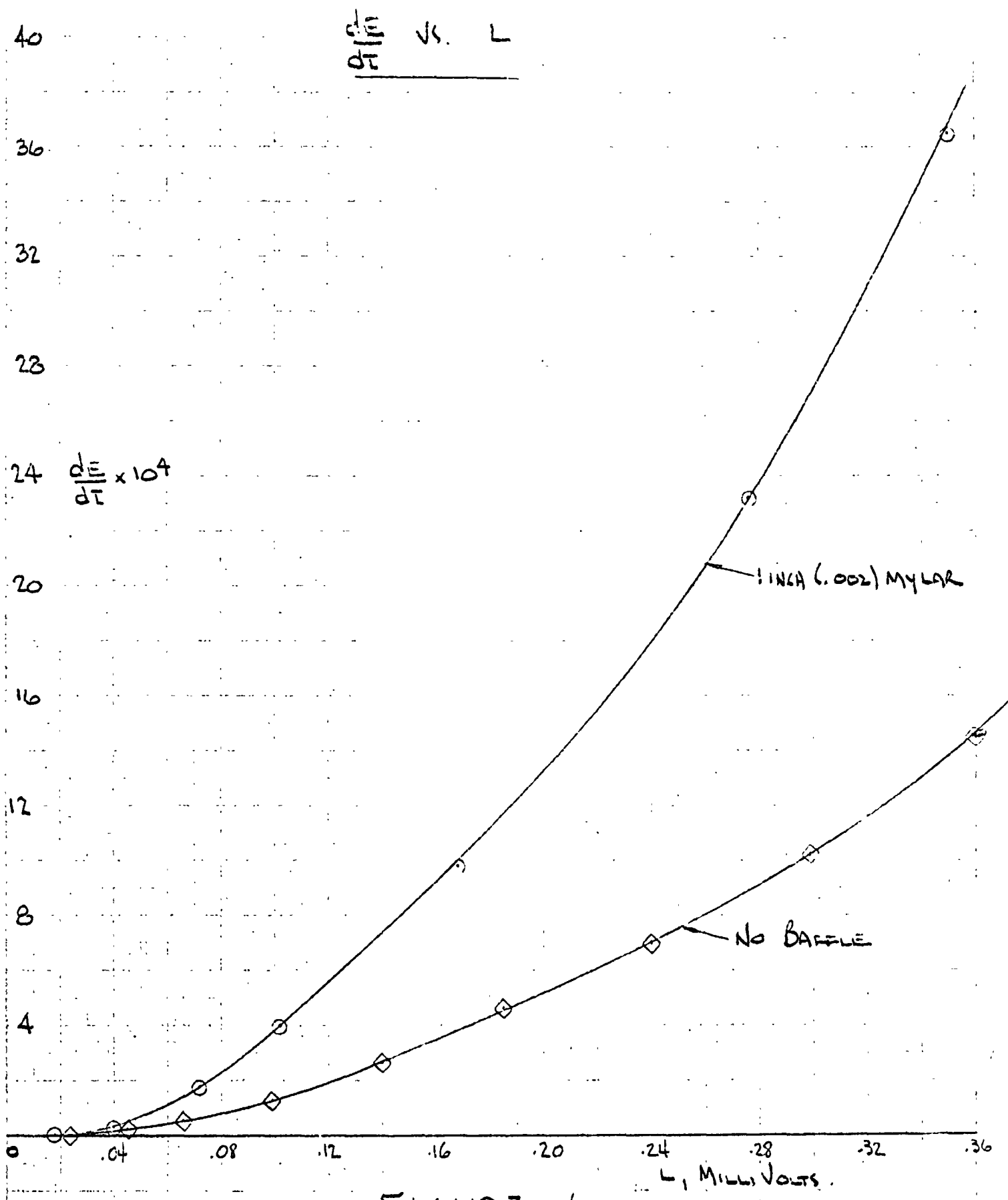


FIGURE 6

Loss Coefficient,  $C_L$

FIGURE 7-A

PERIOD PARAMETER,  $UT/D$

(TYPE I)

◇ - (.001) MYLAR

□ - (.010) MYLAR

○ - (.002) MYLAR

△ - 1 INCH RIGID

◇ - 1 INCH (.001) ST'N ST'W

○ - 1 INCH (.002) ST'N ST'W

PERIOD PARAMETER,  $UT/D$

LOSS COEFFICIENT,  $C_L$

PERIOD PARAMETER,  $UT/D$   
(TYPE I)

4.0

$C_L$

(.005) MYLAR

4.0

$C_L$

1.0

(.0015) MYLAR

0.4

FIGURE 7-B

PERIOD PARAMETER  $UT/D$

$C_L \times UT/D$  - TYPE II BARRAGES.

SPRING SET

- # 1
- # 2
- ◇ # 3
- ▽ # 4

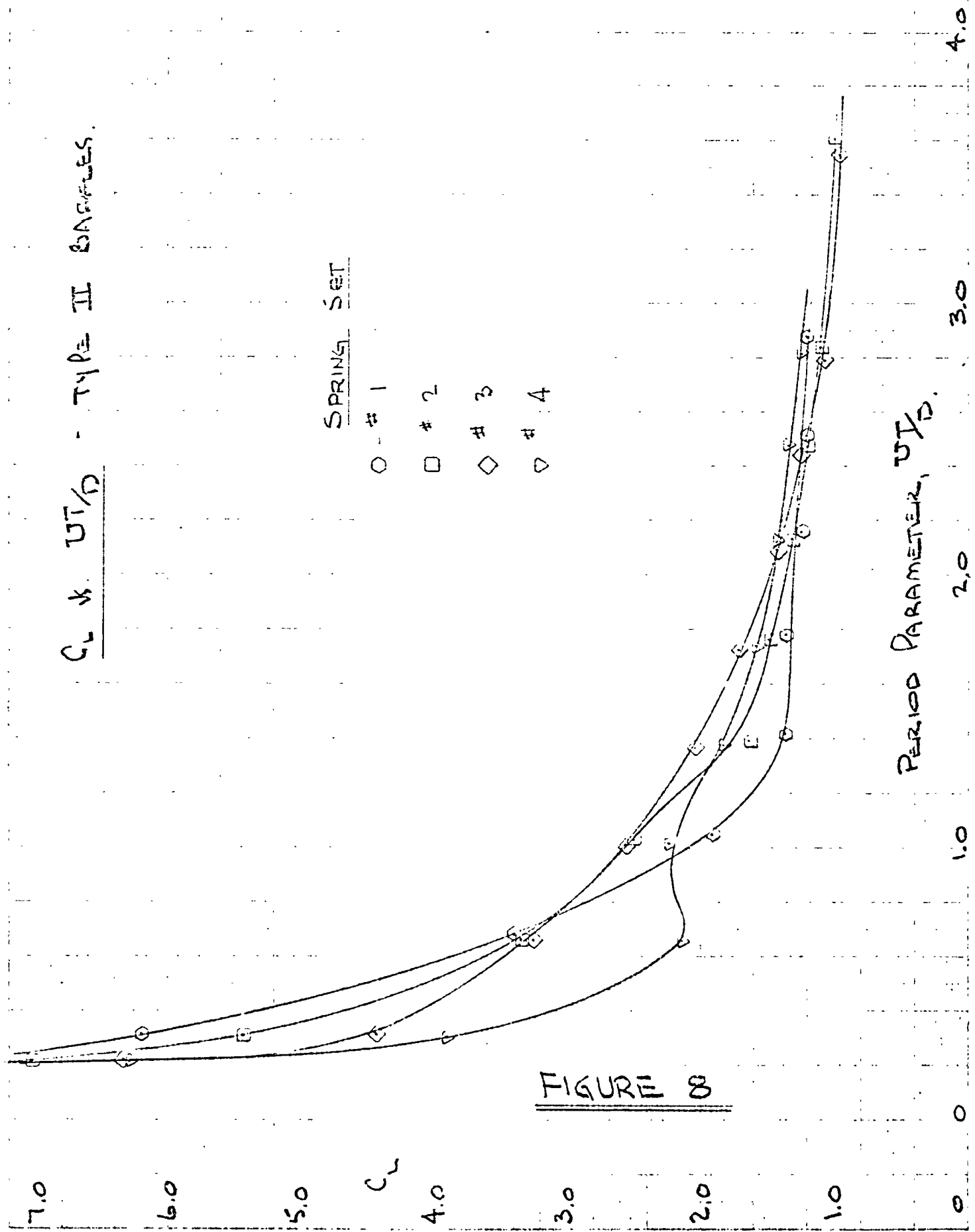


FIGURE 8

PERIOD PARAMETER,  $UT/D$ .





FIGURE 9A PENDULUM APPARATUS -- BAFFLE, STRUT AND SHAFT

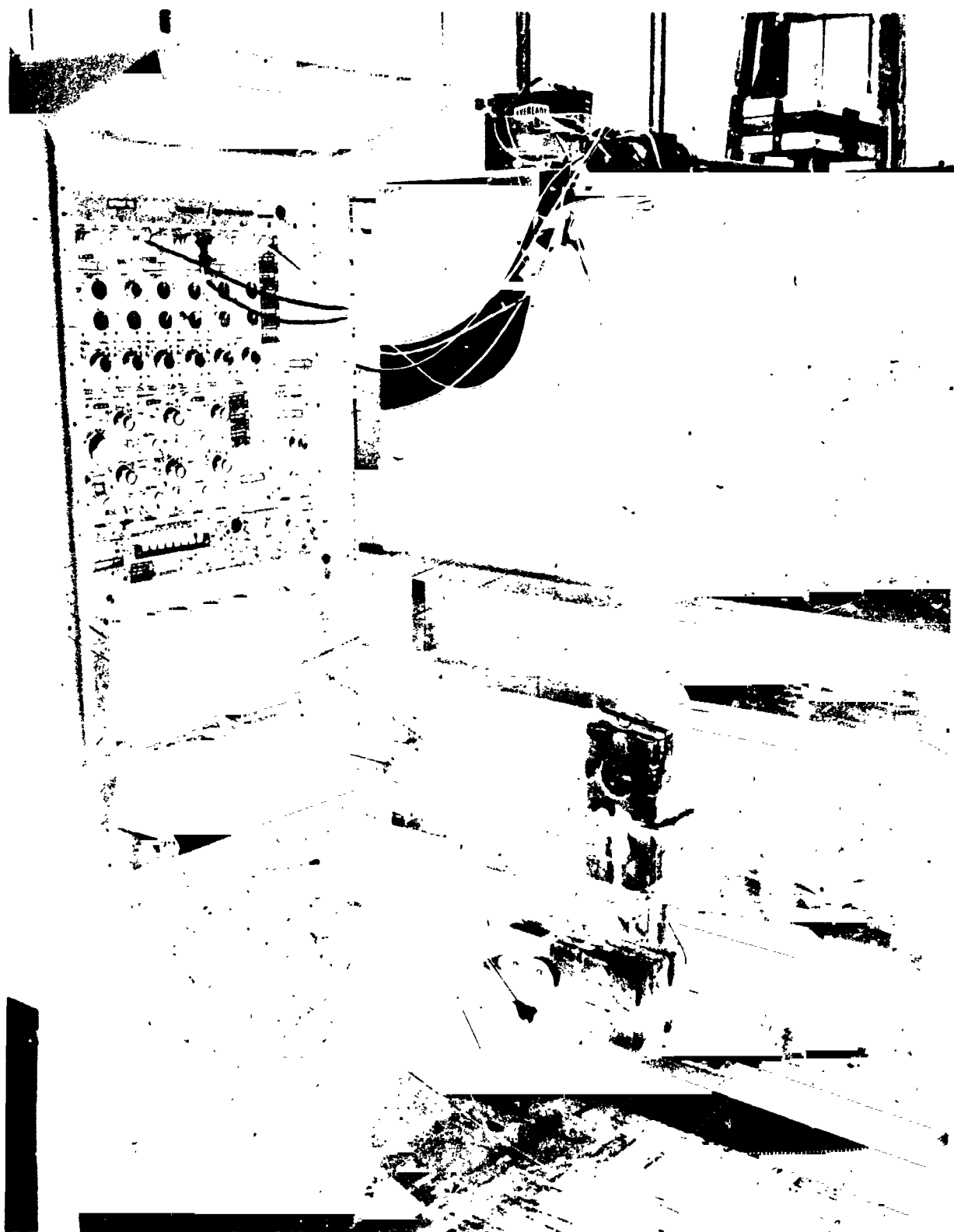


FIGURE 9B PENDULUM APPARATUS - PENDULUM ARM

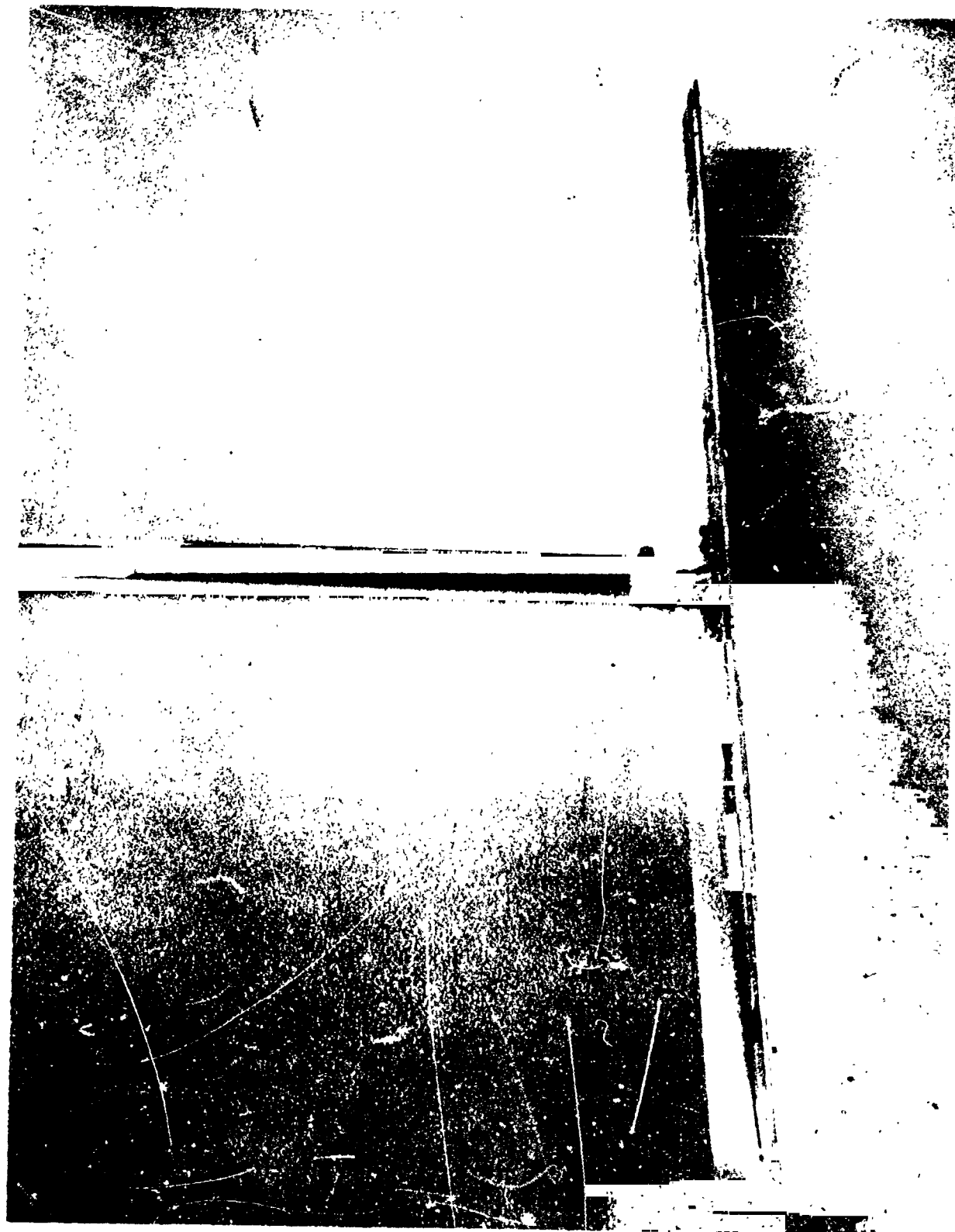


FIGURE 10A MYLAR BAFFLE CLAMPED IN BAFFLE SUPPORT BARS, ATTACHED TO STRUT

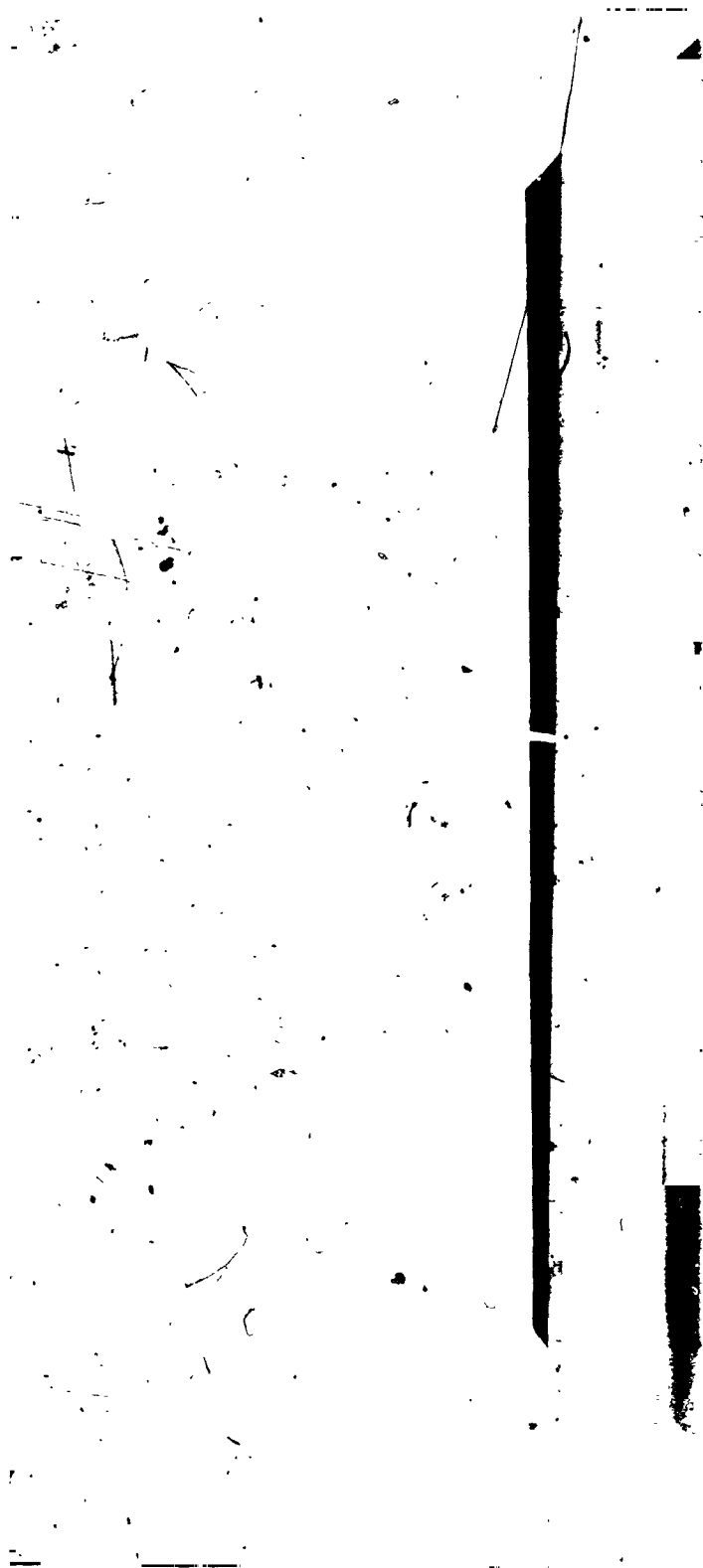


FIGURE 10B SLAMMING BAFFLE BETWEEN BAFFLE SUPPORT BARS

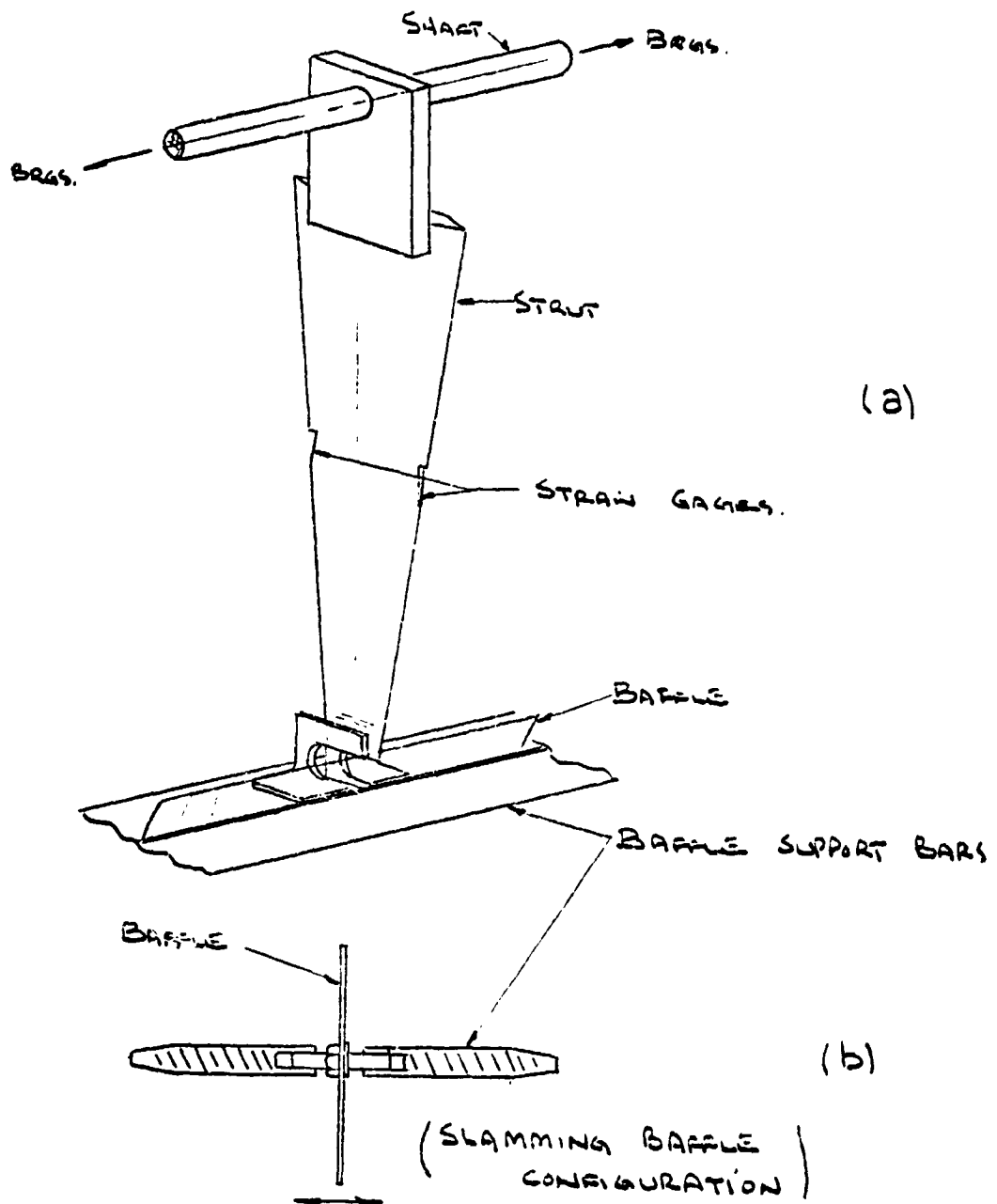


FIGURE 11

STRUT AND BAFFLE  
ARRANGEMENT

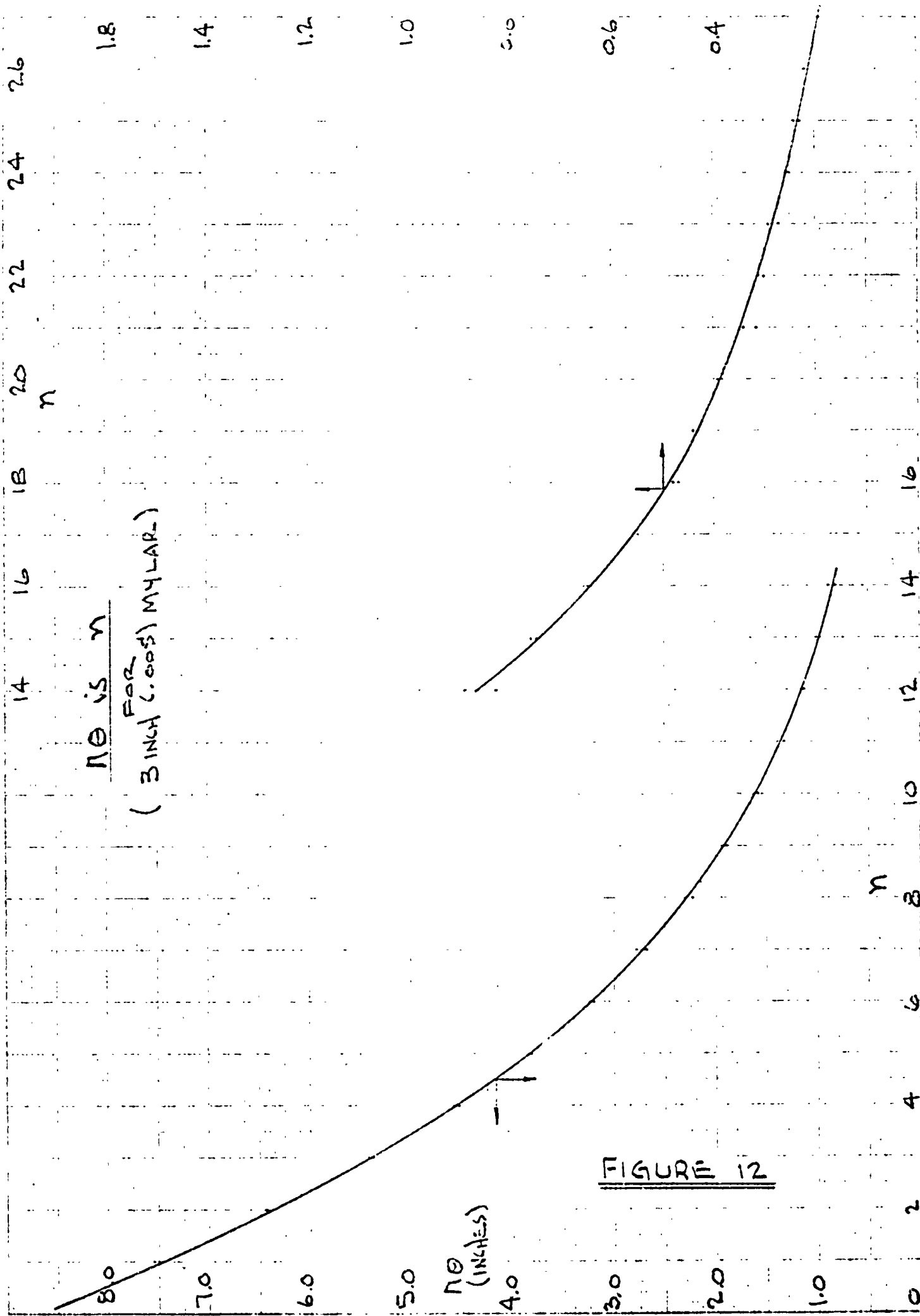


FIGURE 12

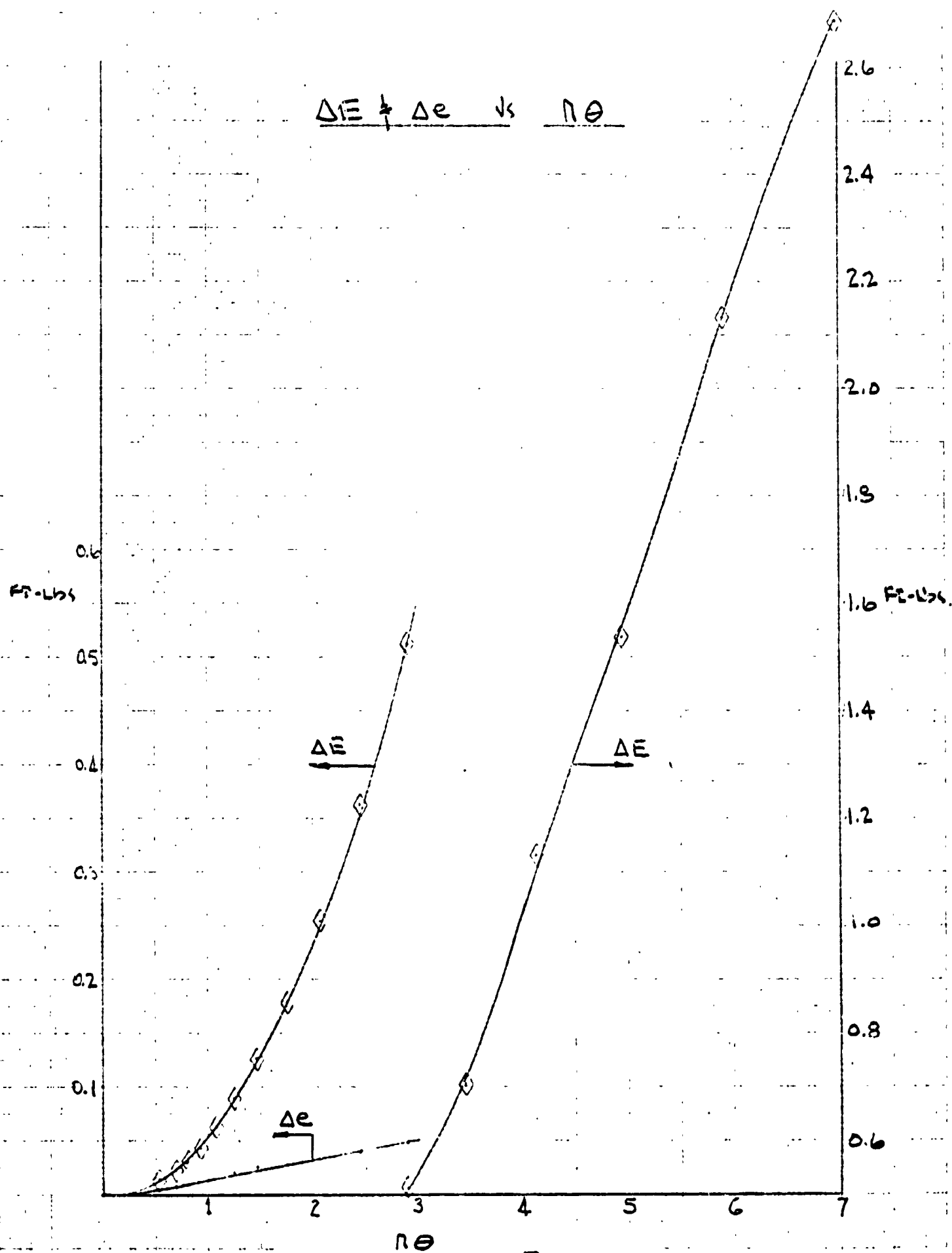


FIGURE 13

STRAIN GAGE CALIBRATION

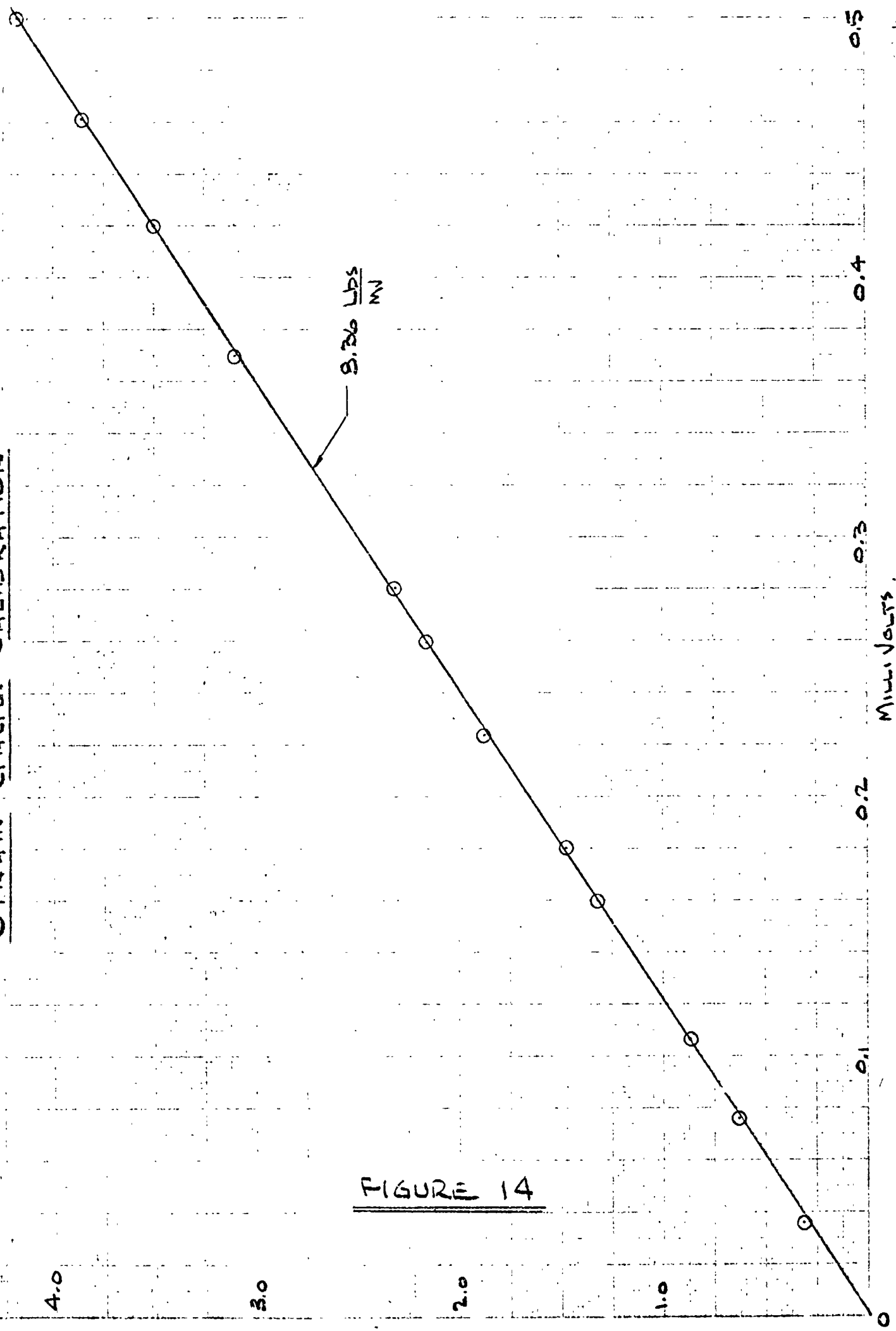
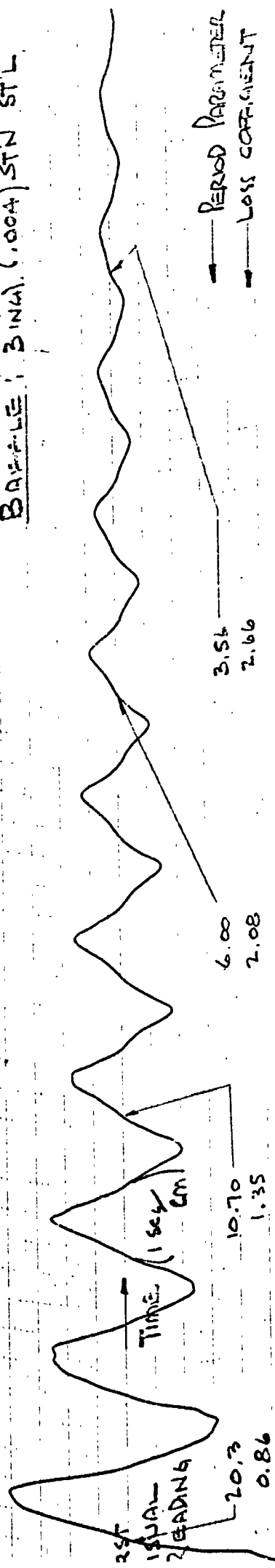


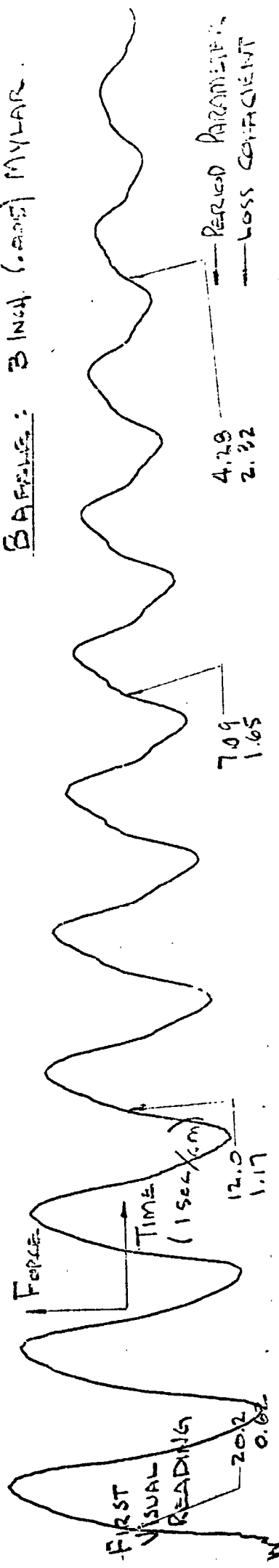
FIGURE 14



Baffle: 3 INCH (1.004) STN STL



Baffle: 3 INCH (1.004) MYLAR



Baffle: 3 INCH RIGID

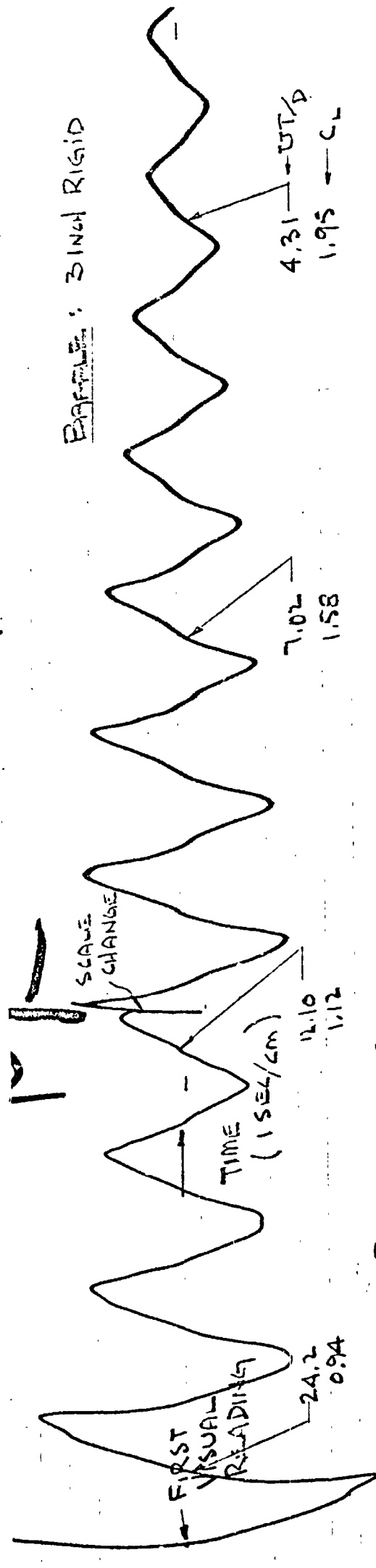


FIGURE 15

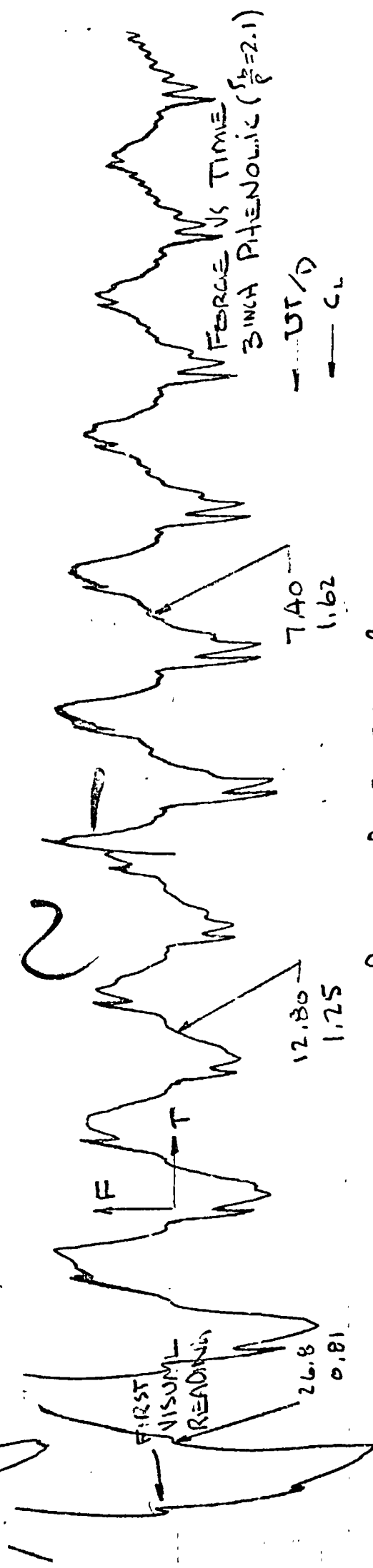
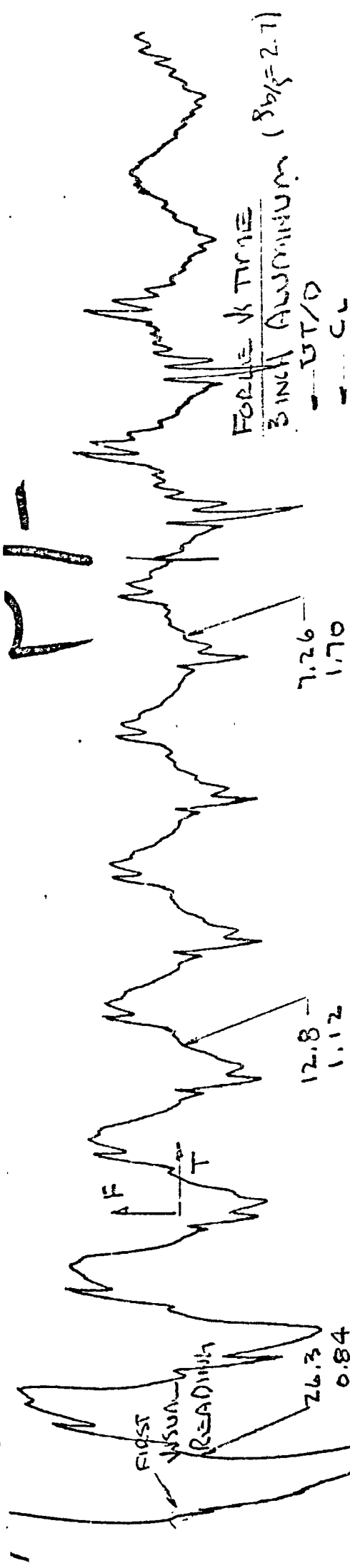
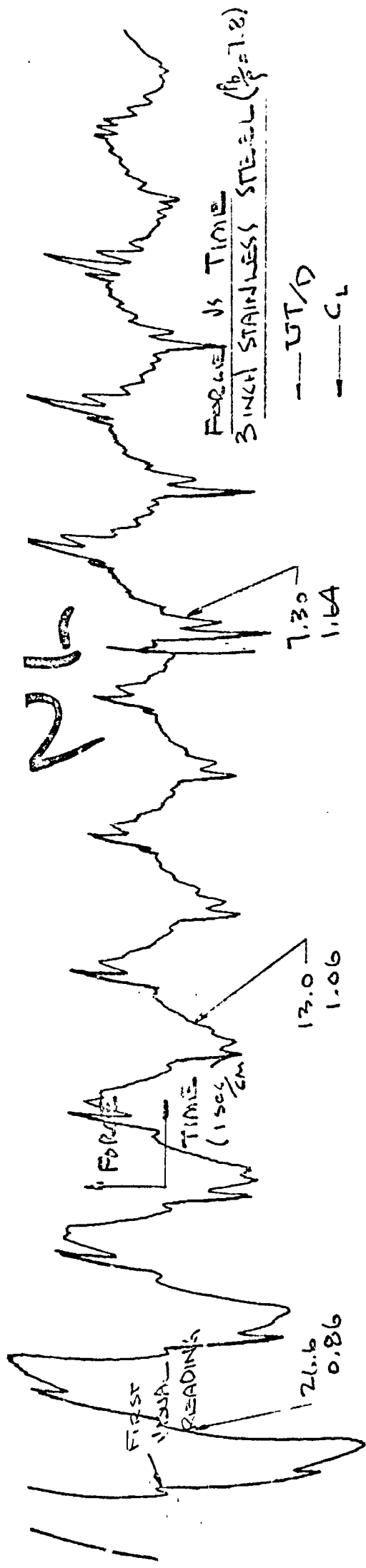
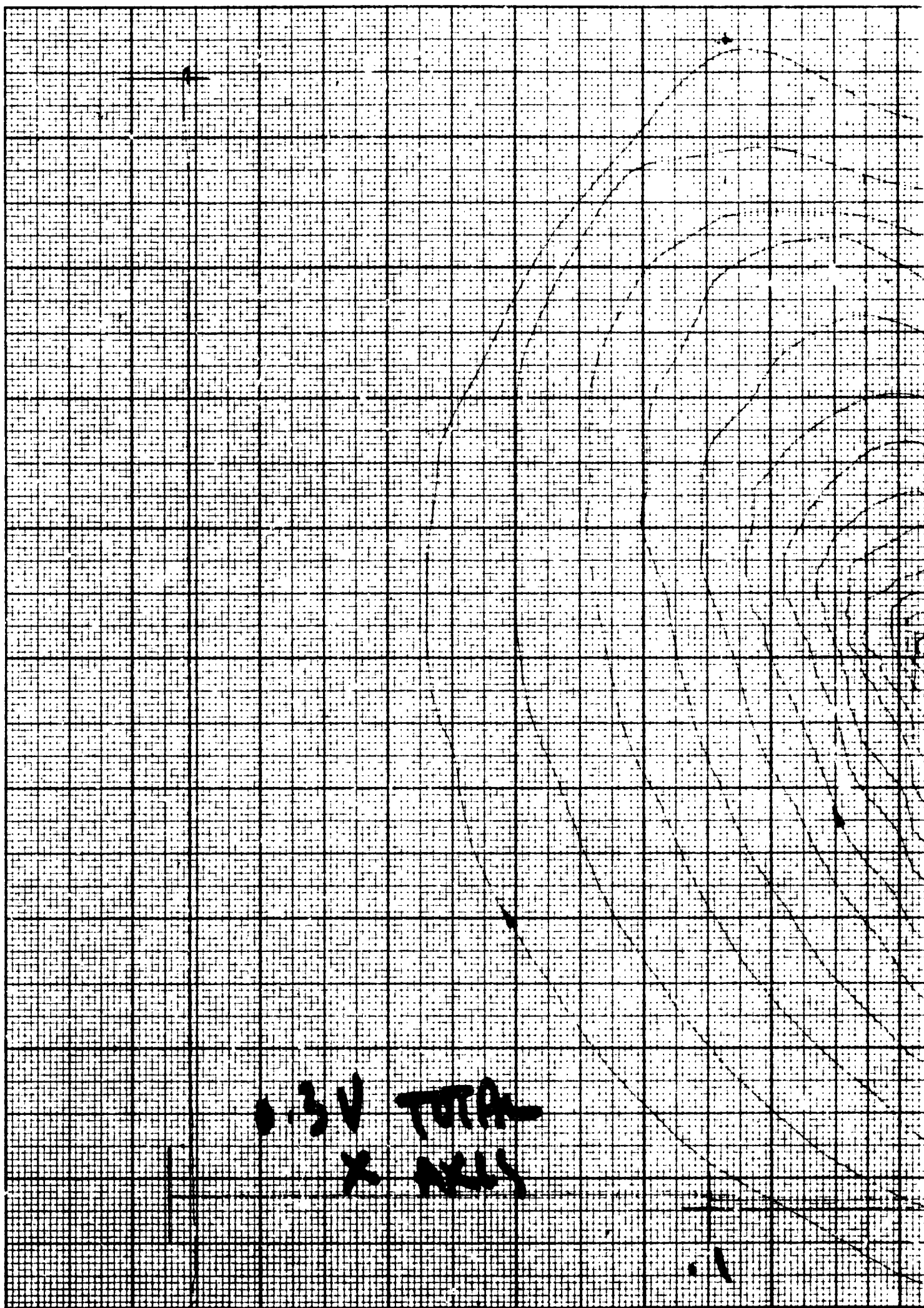


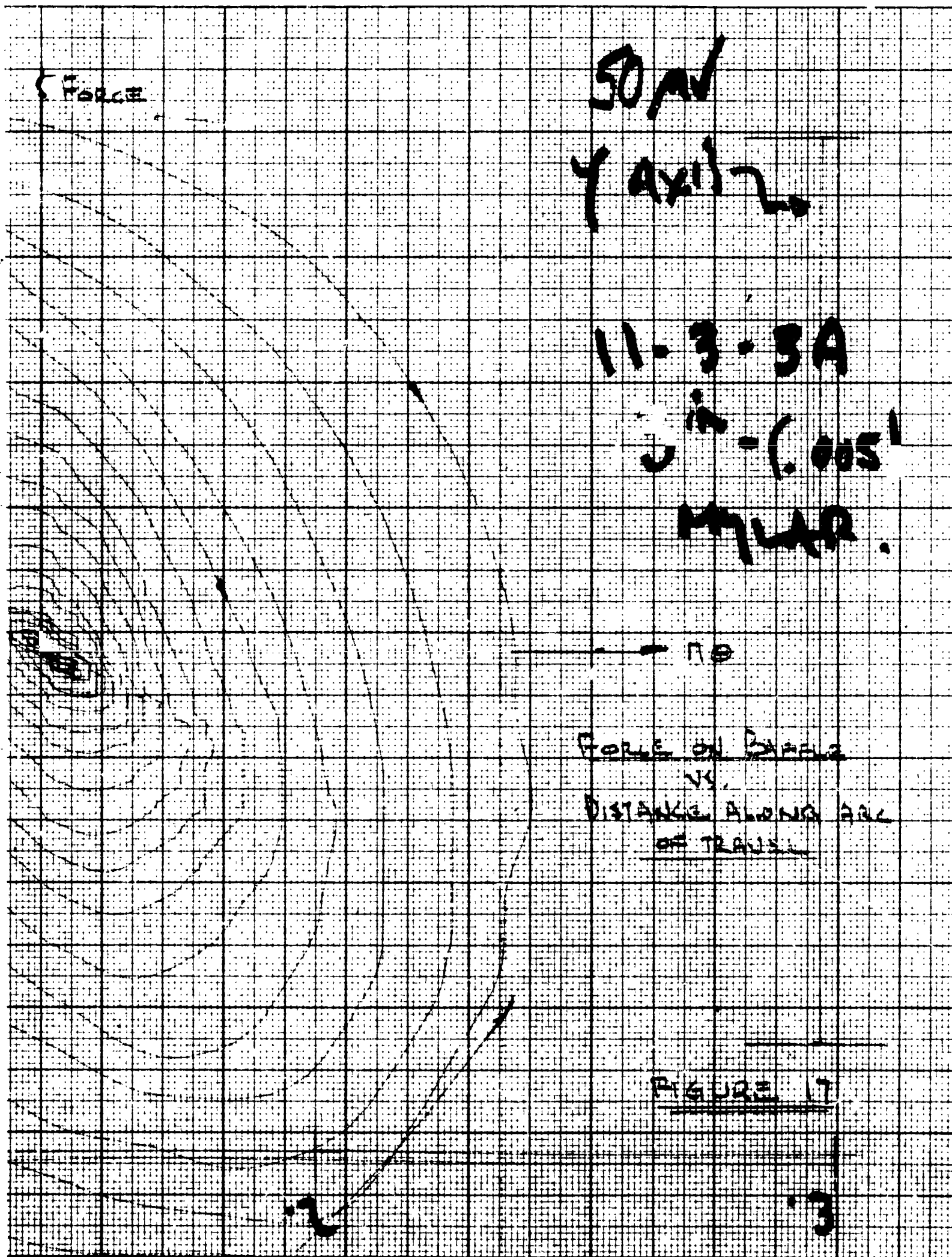
FIGURE 16 TYPE III Baffles,  $\delta/\delta_b = 0.139$



PREPARED BY  
DATE  
CHECKED BY

LOCKHEED AIRCRAFT CORPORATION  
MISSILES SYSTEMS DIVISION

PAGE  
MODEL  
REPORT NO



4.0

10.0  $UT/D$ 

40.0

2" RIGID $F = 0$ 

4.0

 $C_L$ 

1.0

-EXPERIMENTAL DATA (.)

-ANALYTIC CURVE FIT (O)

4.0

1.0

2" (.004) STAINLESS STEEL $F = 5.76 \times 10^{-6}$ FIGURE 18 (A)LOSS COEFFICIENT

VS

PERIOD PARAMETER(TYPE I BAFFLES)

4

10

 $UT/D$ 

40

4.0

10.0  $\frac{U}{D}$ 

40.0

4.0

2  $\frac{1}{2}$  (.003) STAINLESS STEEL

$$F = 1.357 \times 10^{-5}$$

 $C_L$ 

1.0

4.0

2  $\frac{1}{2}$  (.002) STAINLESS STEEL

$$F = 4.49 \times 10^{-5}$$

1.0

FIGURE 18(B)

4.0

10.0  $\frac{U}{D}$ 

40.0

4.0

10.0

 $\frac{U_T}{D}$ 

40.0

4.0

2 IN (.005) MYLAR $F = 1.07 \times 10^{-4}$  $C_L$ 

1.0

4.0

2 IN (.003) MYLAR $F = 4.99 \times 10^{-4}$  $C_L$ 

1.0

FIGURE 18 (C)

4.0

10.0

 $\frac{U_T}{D}$ 

40.0

2 1/2 (.002) MYLAR  
 $F = 1.74 \times 10^{-3}$

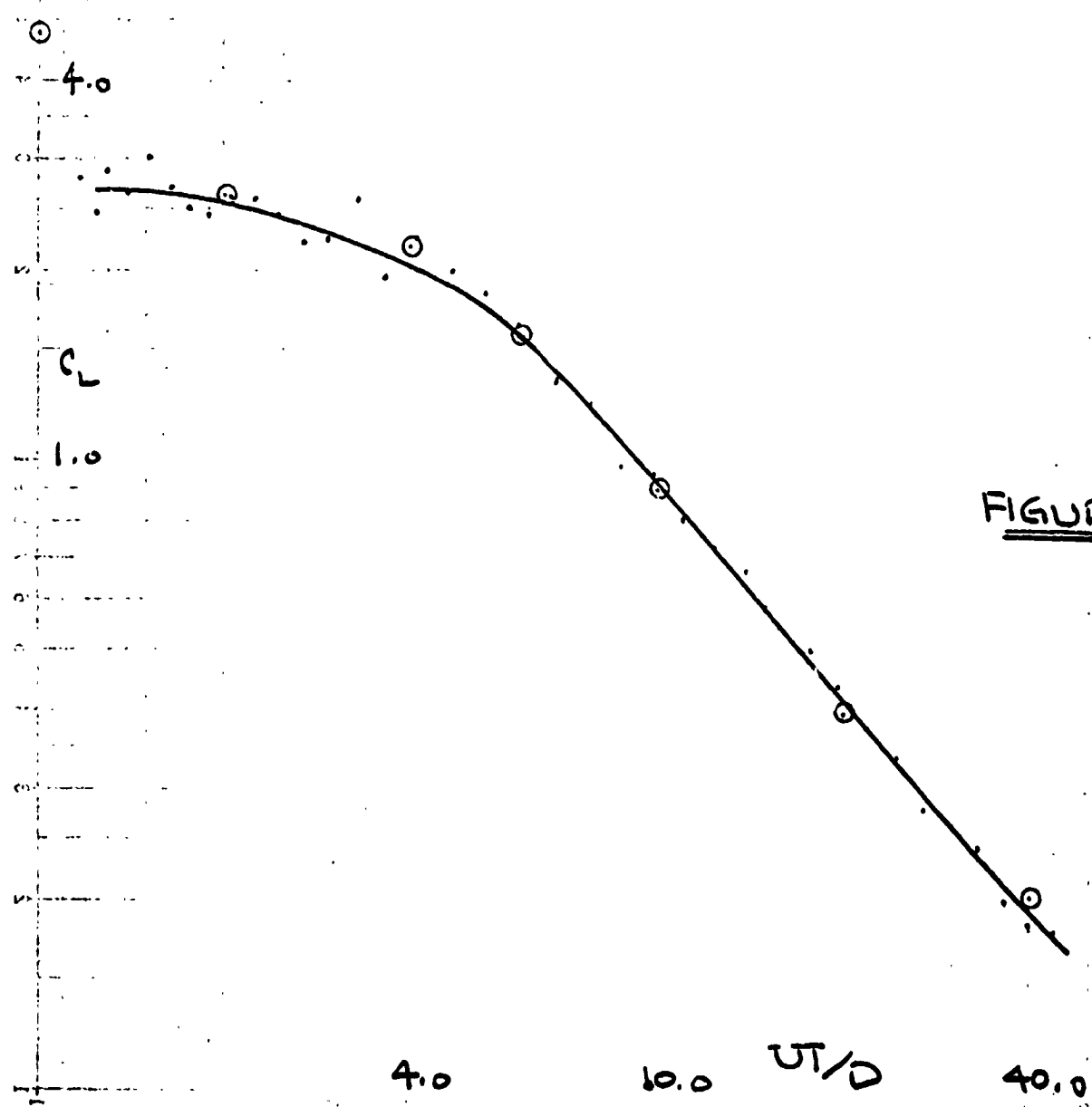


FIGURE 18(D)



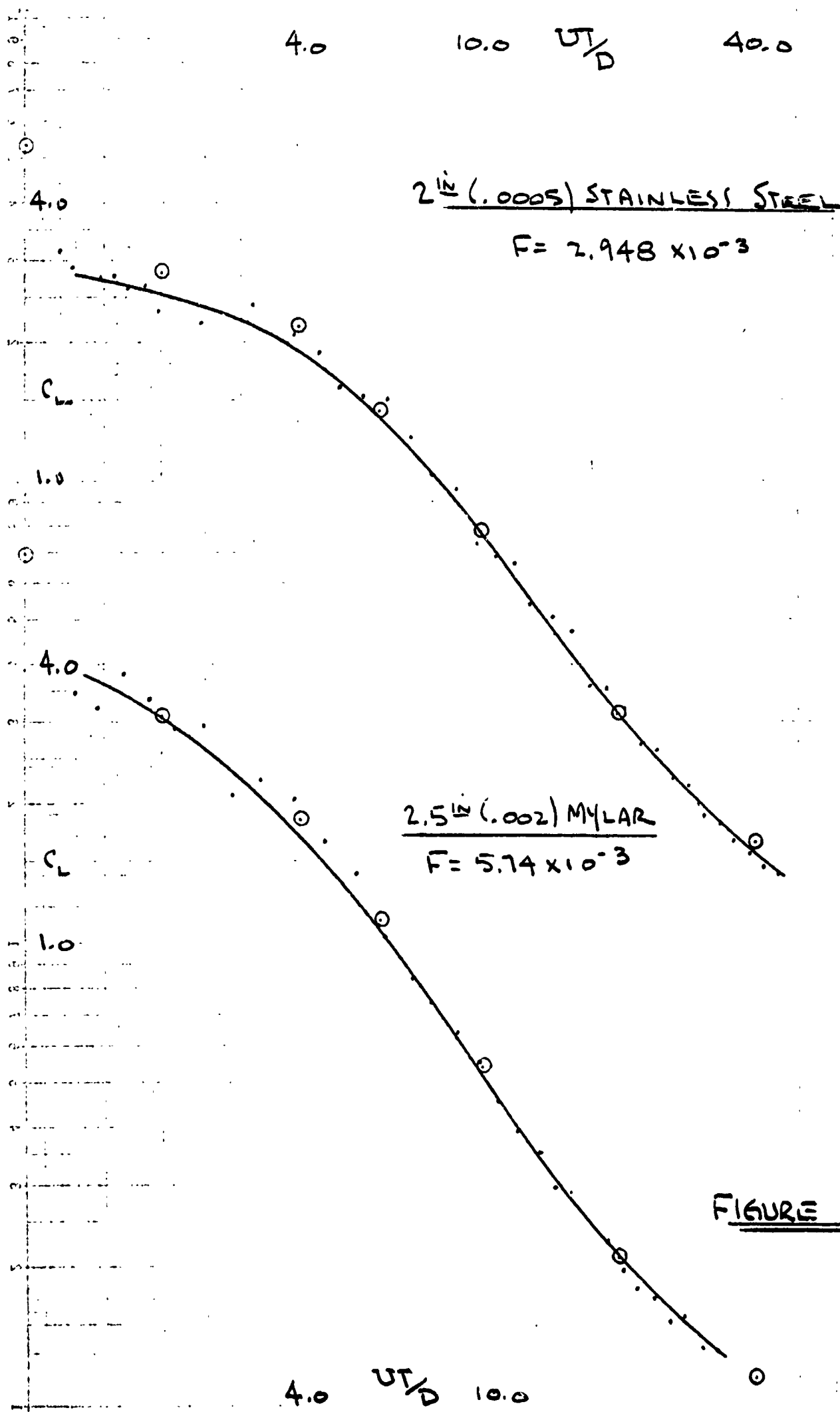


FIGURE 18(E)

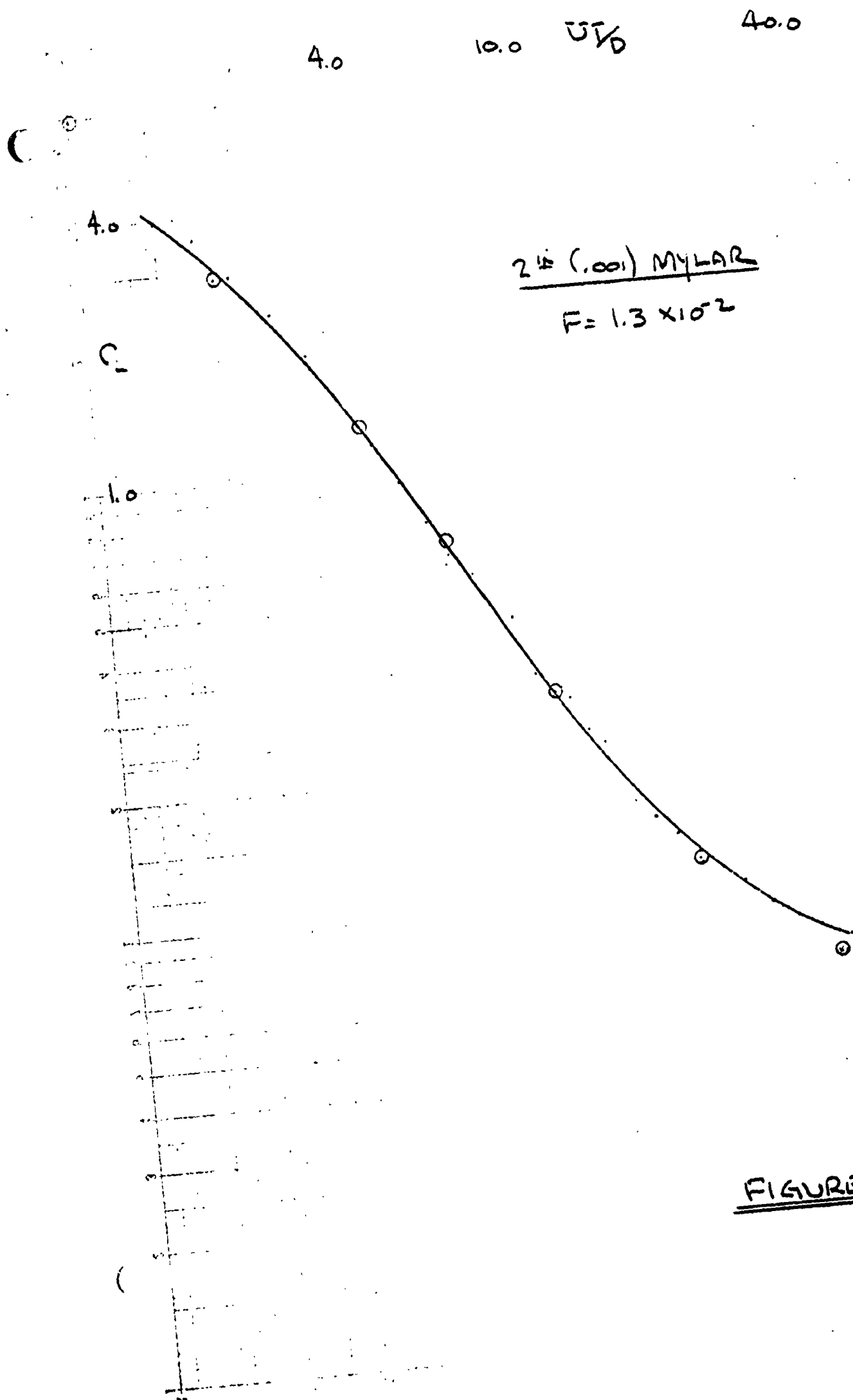


FIGURE 1B(F)

0

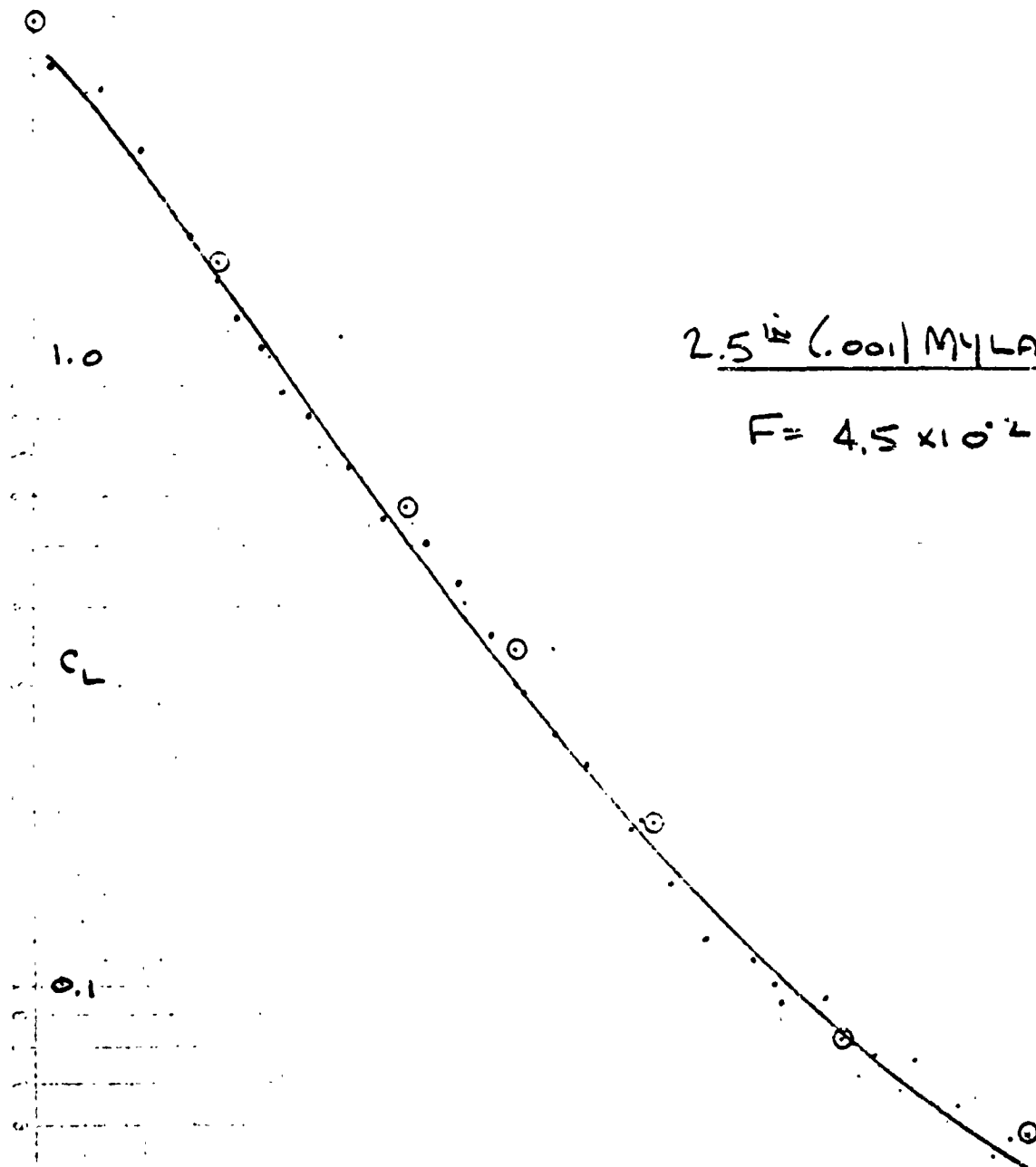


FIGURE 18 (G)

0

# Loss Coefficient vs Flexibility

+ ANALYTIC CORRELATION

△, ◇, ○, □ EXPERIMENTAL DATA

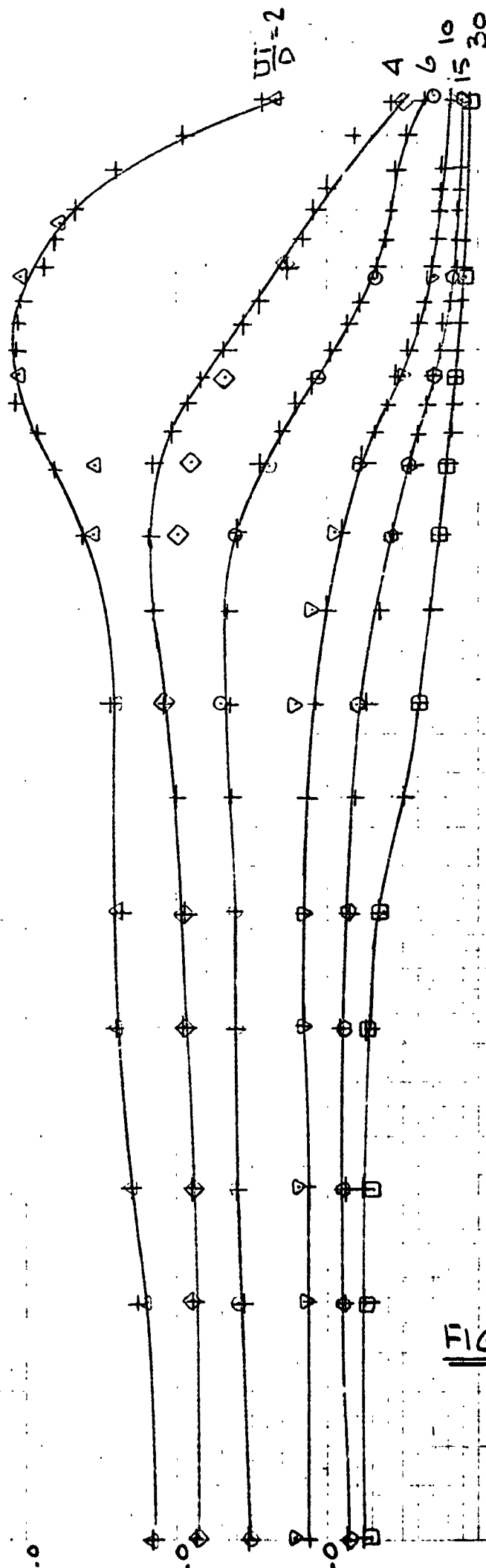
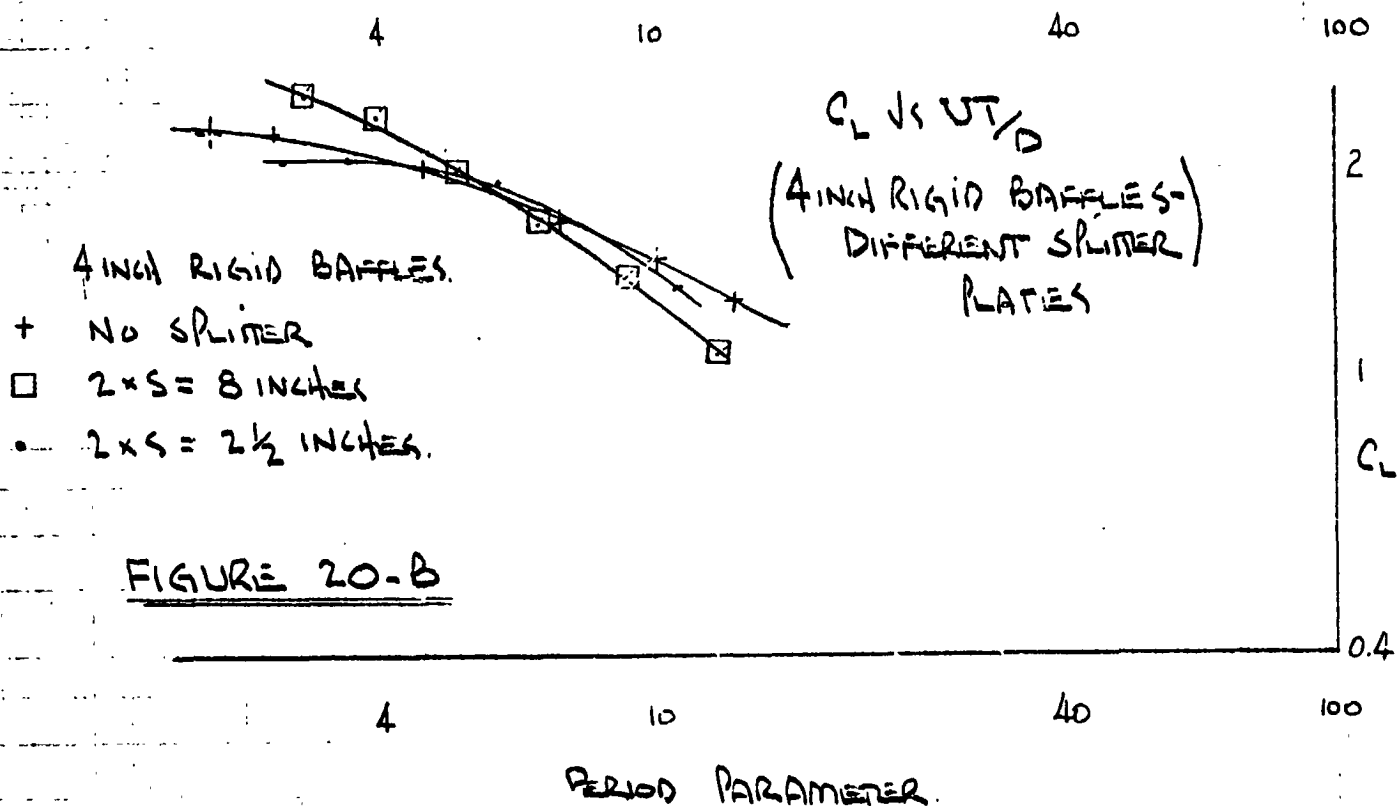
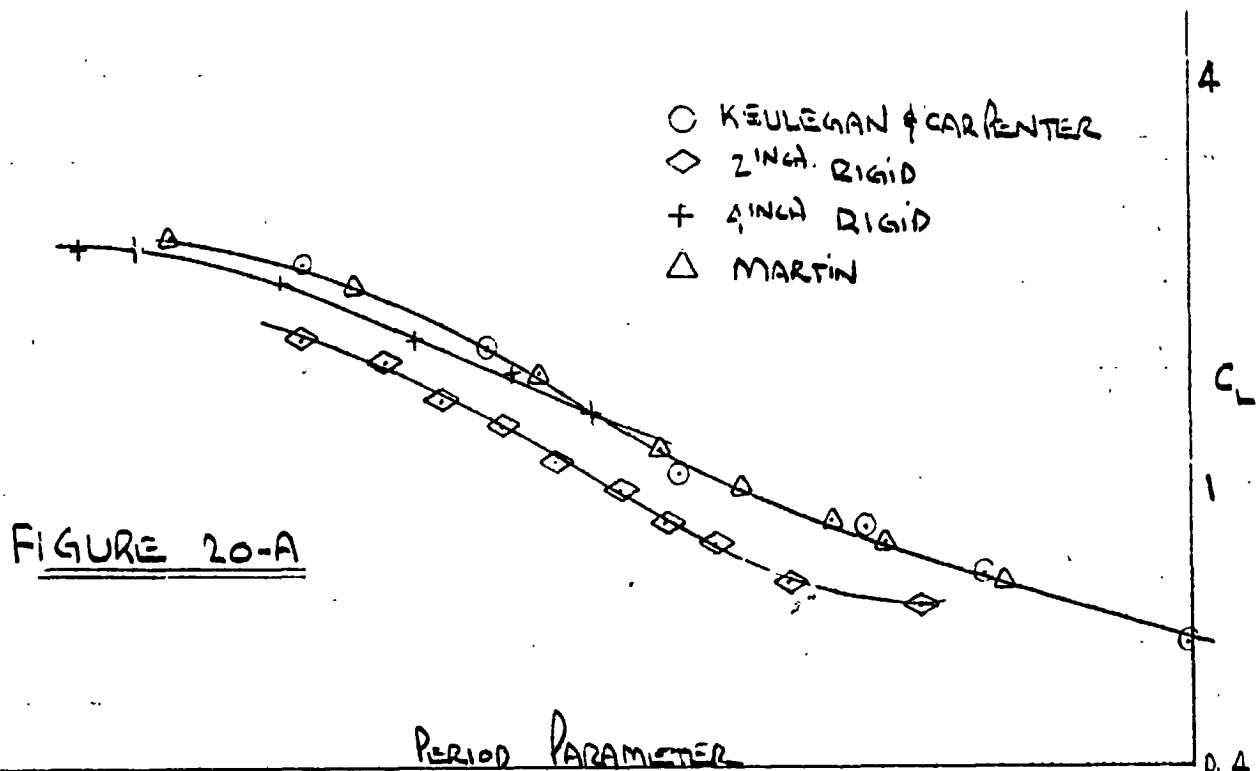


FIGURE 19

2 DASHES X TO DASH 2'S FOR 0.024  
SEMI-LOGS IN X AXIS

FLEXIBILITY, FA

... LOSS COEFFICIENT VS PERIOD PARAMETER.  
(RIGID BAFFLES - NO SPLITTER PLATES)



$C_L \text{ vs } \frac{UT}{D}$   
(SPLITTER RATE EFFECT)

4.0

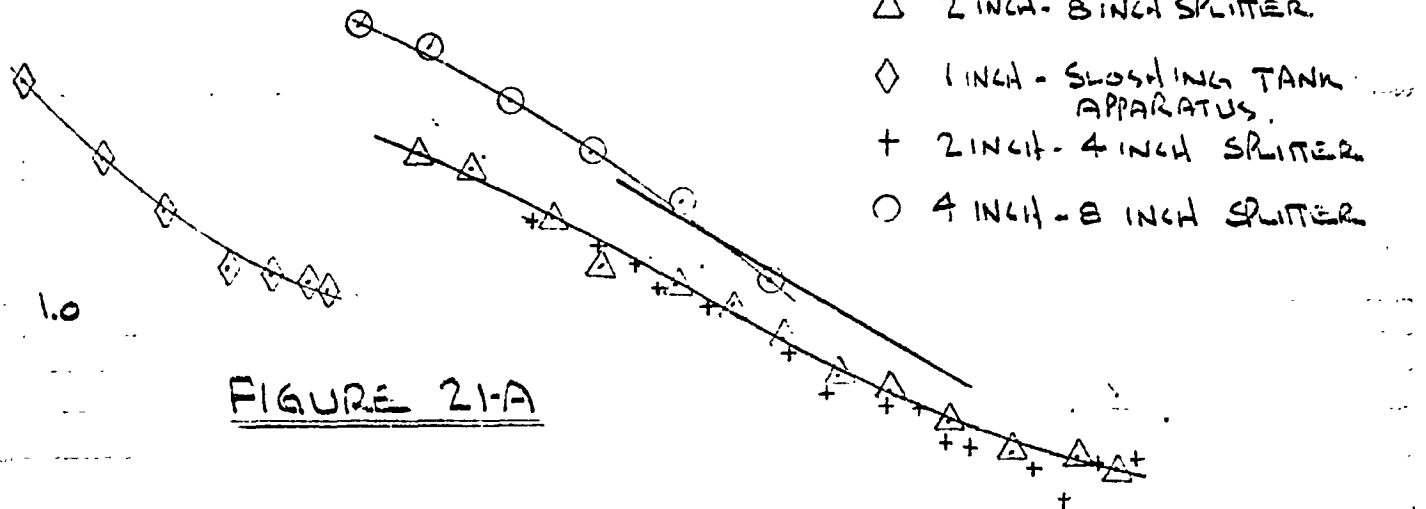


FIGURE 21-A

1.0 LOSS COEFFICIENT,  $C_L$

vs.  
PERIOD PARAMETER,  $\frac{UT}{D}$   
(FOR RIGID BAFFLES WITH  
SUPPORT BARS)

0.4

RIGID  
△ 1 INCH  
◇ 2  
○ 3  
◇ 4

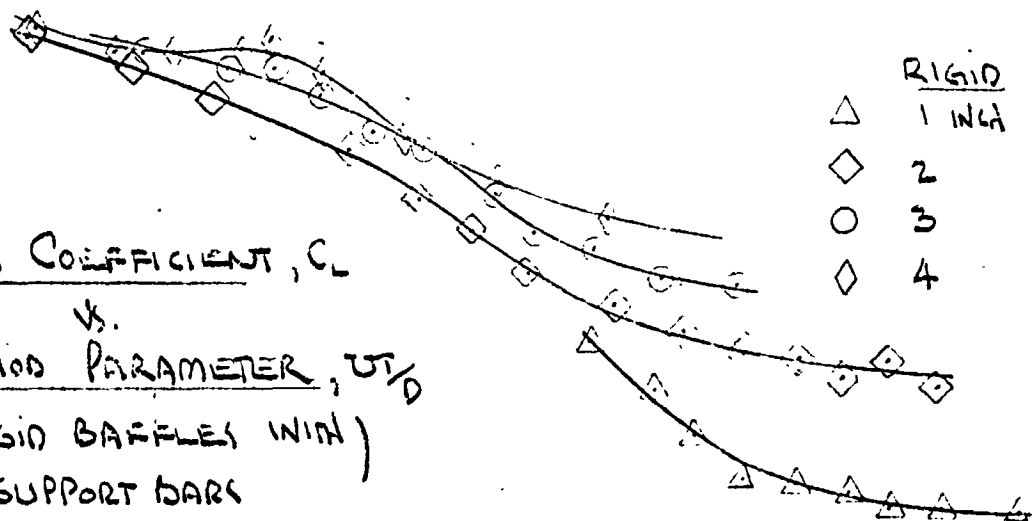
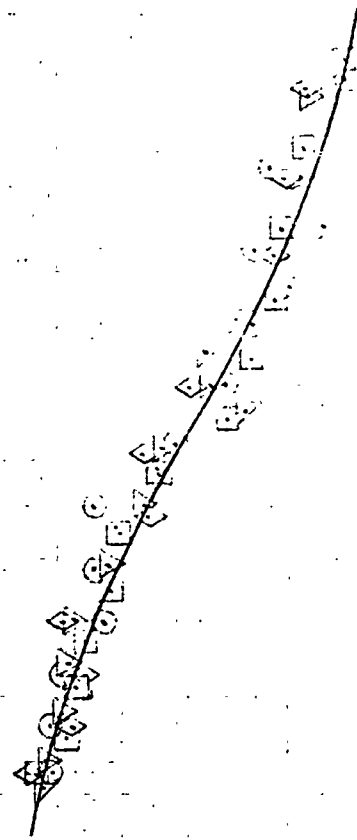


FIGURE 21-B

PERIOD PARAMETER,  $\frac{UT}{D}$

Loss Coefficient vs Period Parameter

TYPE III BARRIES - EFFECT OF TRAVEL (GAP)  
TO BAFFLE WIDTH RATIO,  $g/D$



3 INCH ALUMINUM ( $g_b/p = 2.7$ )

- 0.270
- ◇ 0.185
- 0
- ▽ 0
- ▽ 0.267

PERIOD PARAMETER

40.0

10.0

4.0

FIGURE 22

# Loss Coefficient vs Period Parameter - (Type III Barriers - Effect of Density)

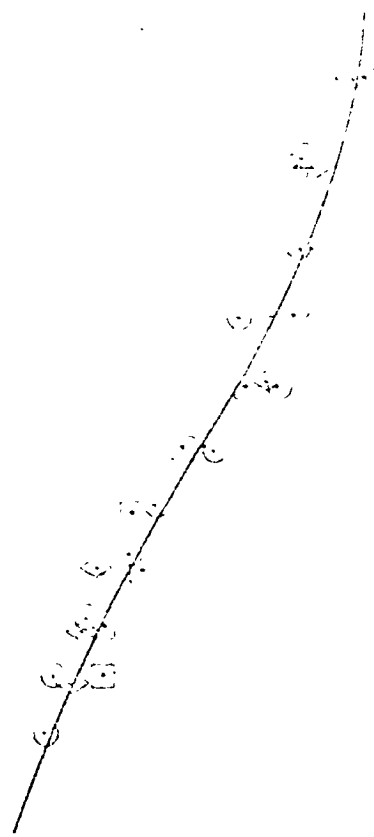


FIGURE 20

- 2.1 (Density = 2.1)
- 2.5 (Density = 2.5)
- ◇ 7.0 (Density = 7.0)



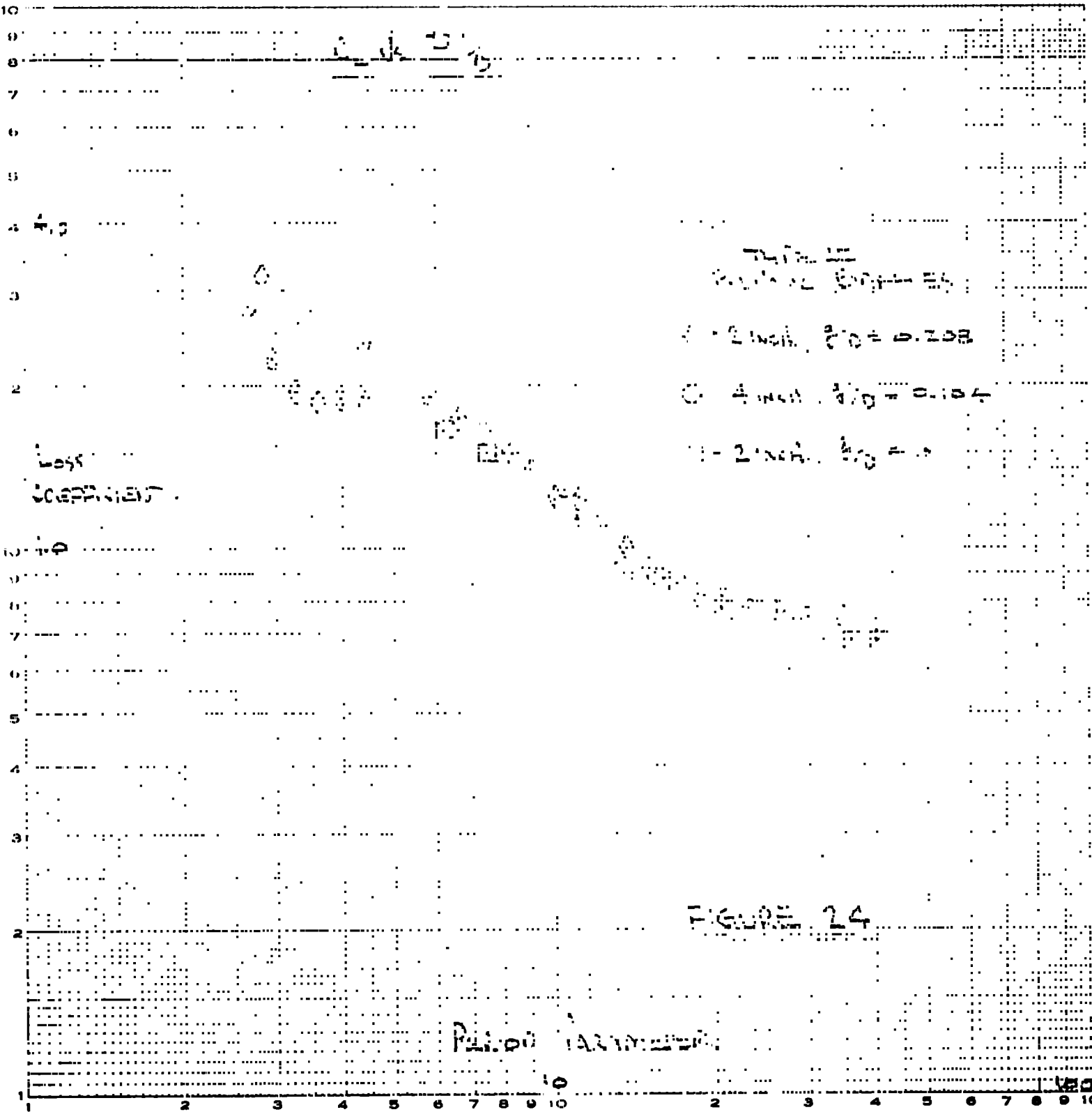


FIGURE 24

frame #1

#6

11

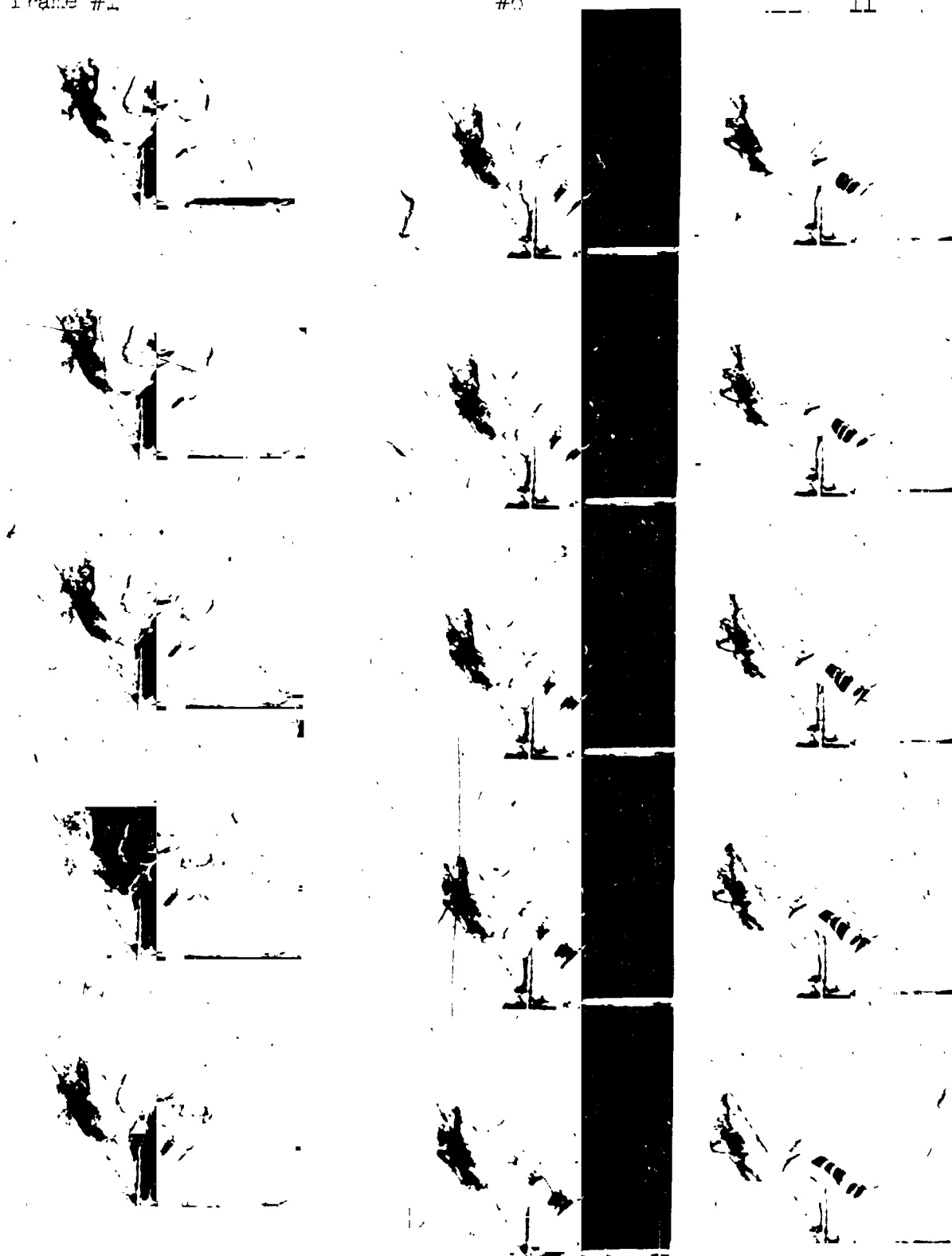


Figure 15 16 mm Motion Picture Sequence, 32 frames/second  
1 inch rigid baffle, 0.88 seconds/cycle  $UT/D = 1.60$   $F = 0$

frame #16

21

26

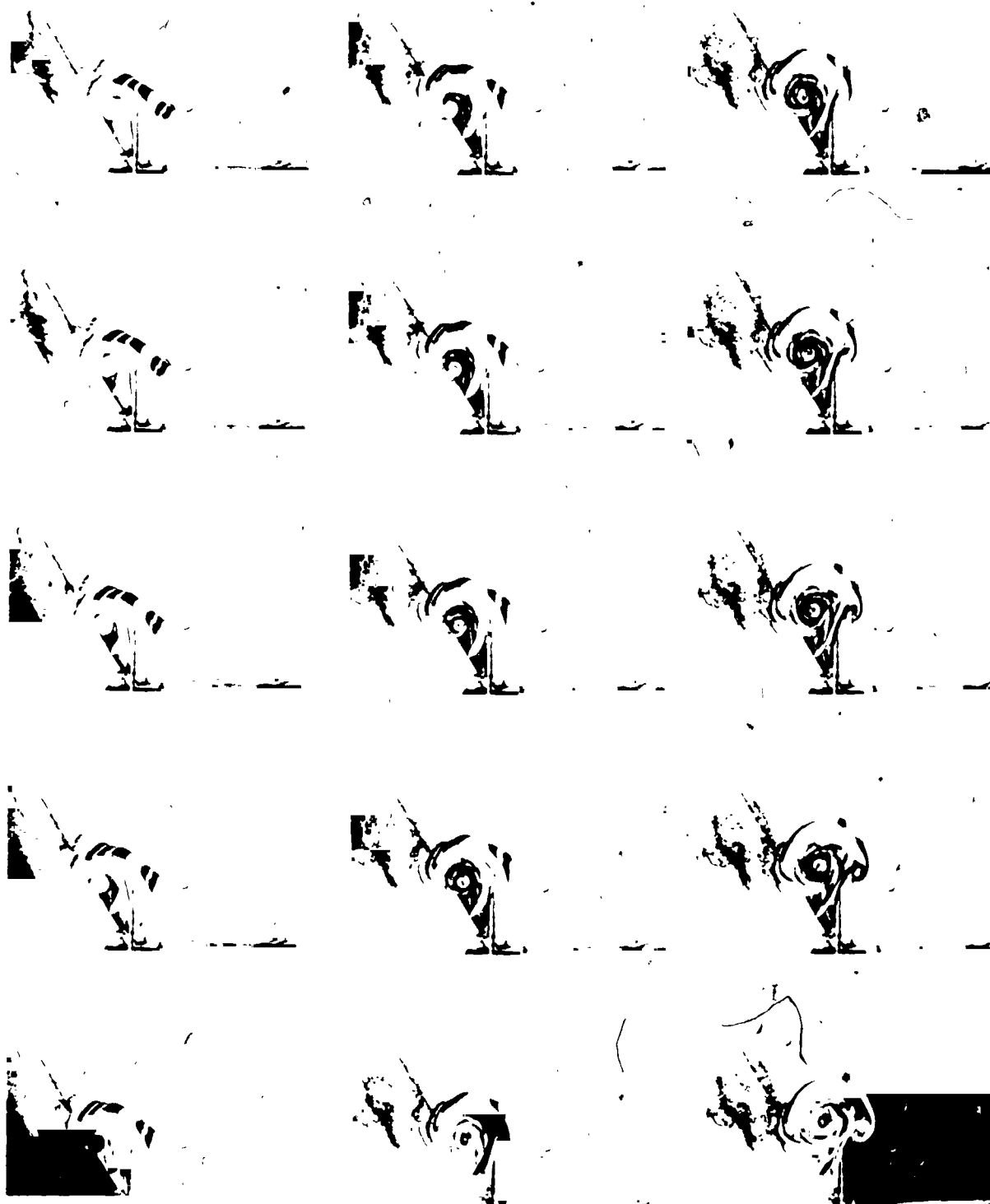


Figure 25, continued



# DISPLACEMENT vs TIME

RIGID BAFFLE  $U_{10} = 1.60$

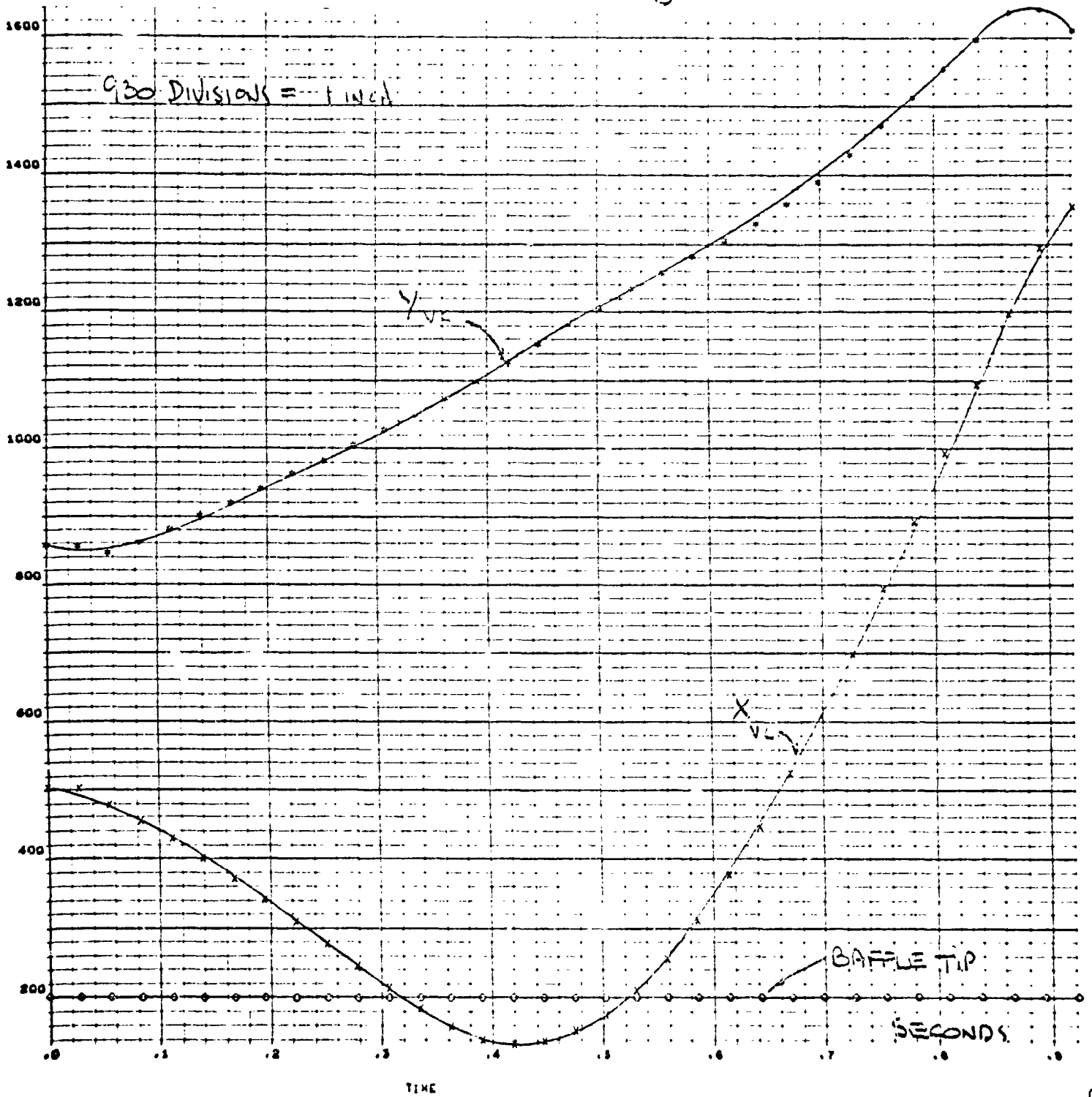


FIGURE 26

# VELOCITY vs TIME

RIGID BAFLE,  $U_{T/D} = 1.60$

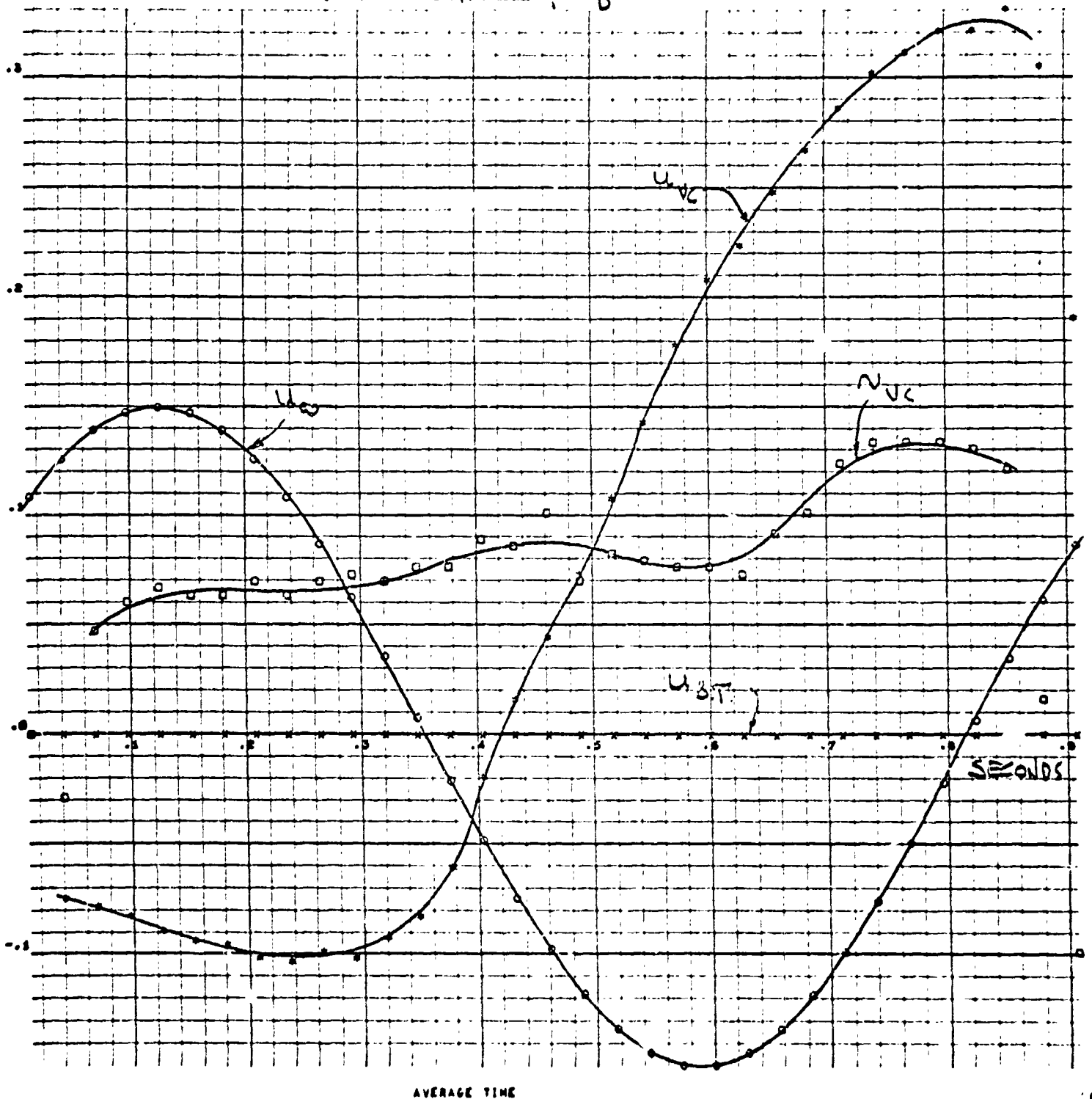


FIGURE 27

VORTEX CENTER X VS Y

RIGID BAFFLE,  $U_T/D = 1.60$

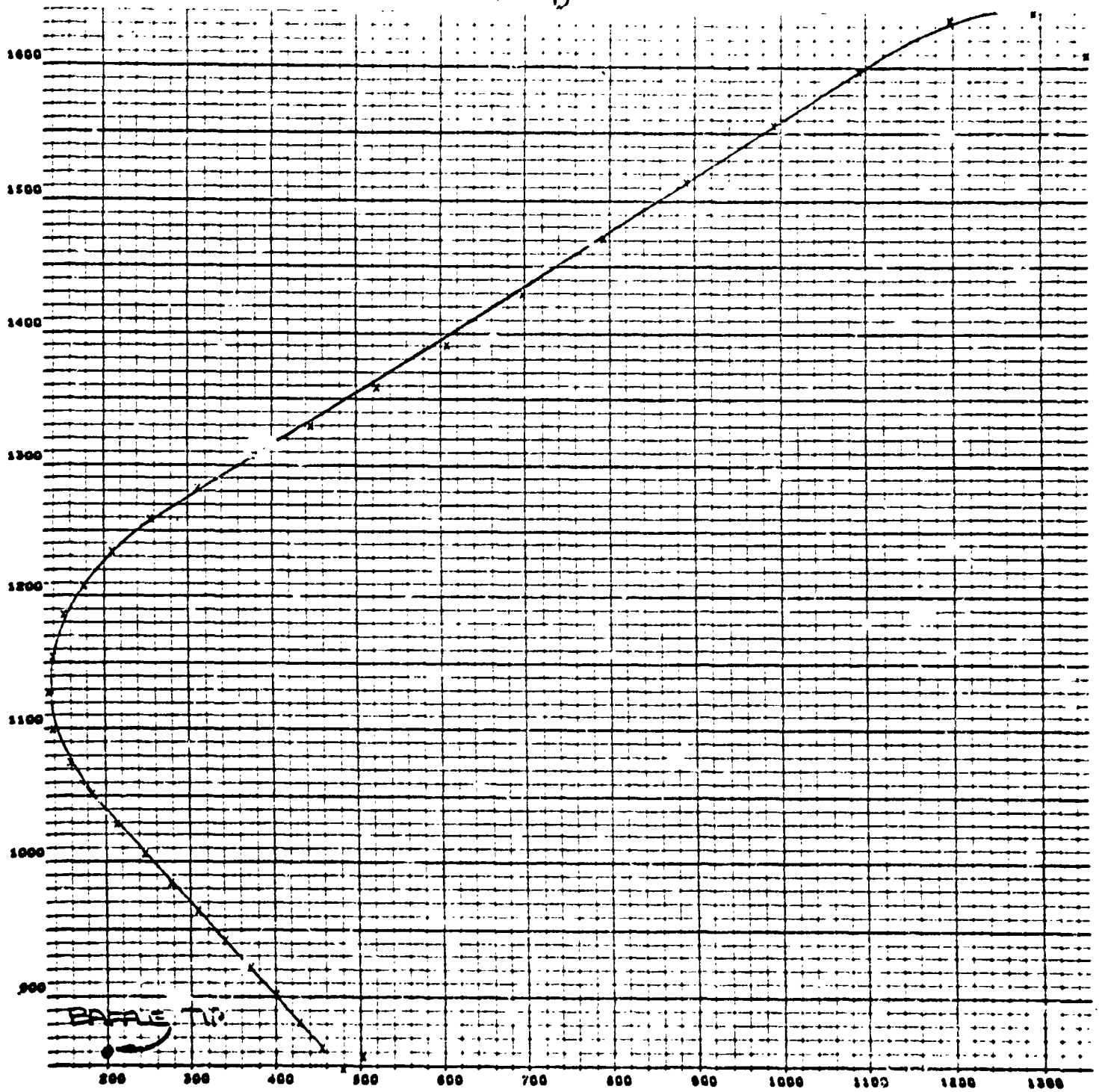


FIGURE 28

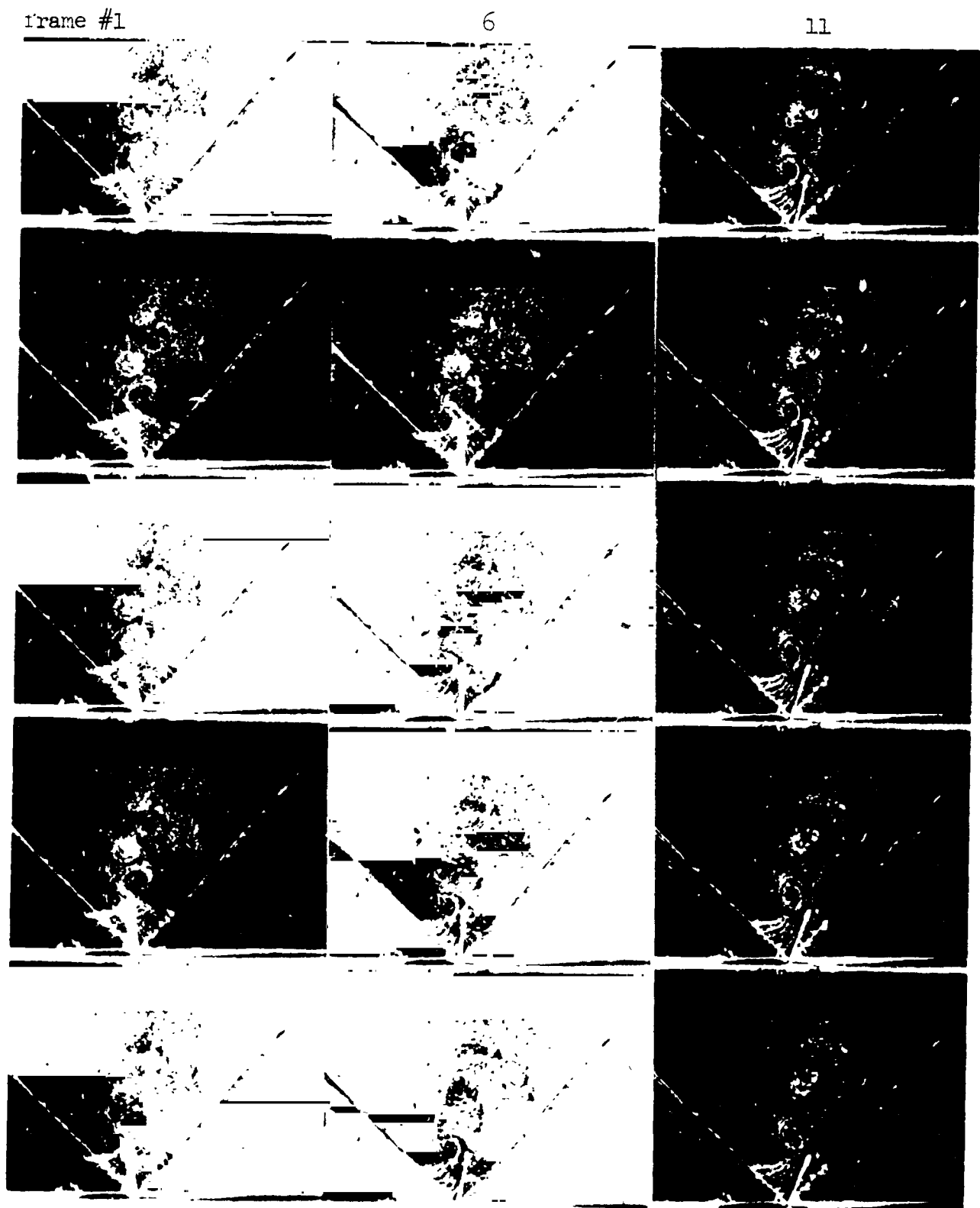


Figure 29 16 mm Motion Picture Sequence, 32 frames/second  
 Type I, 1 X .001 inch mylar baffle, 0.88 seconds/cycle  $UT/D = 0.79$ ,  
 $F = 0.137$



frame #16

21

26

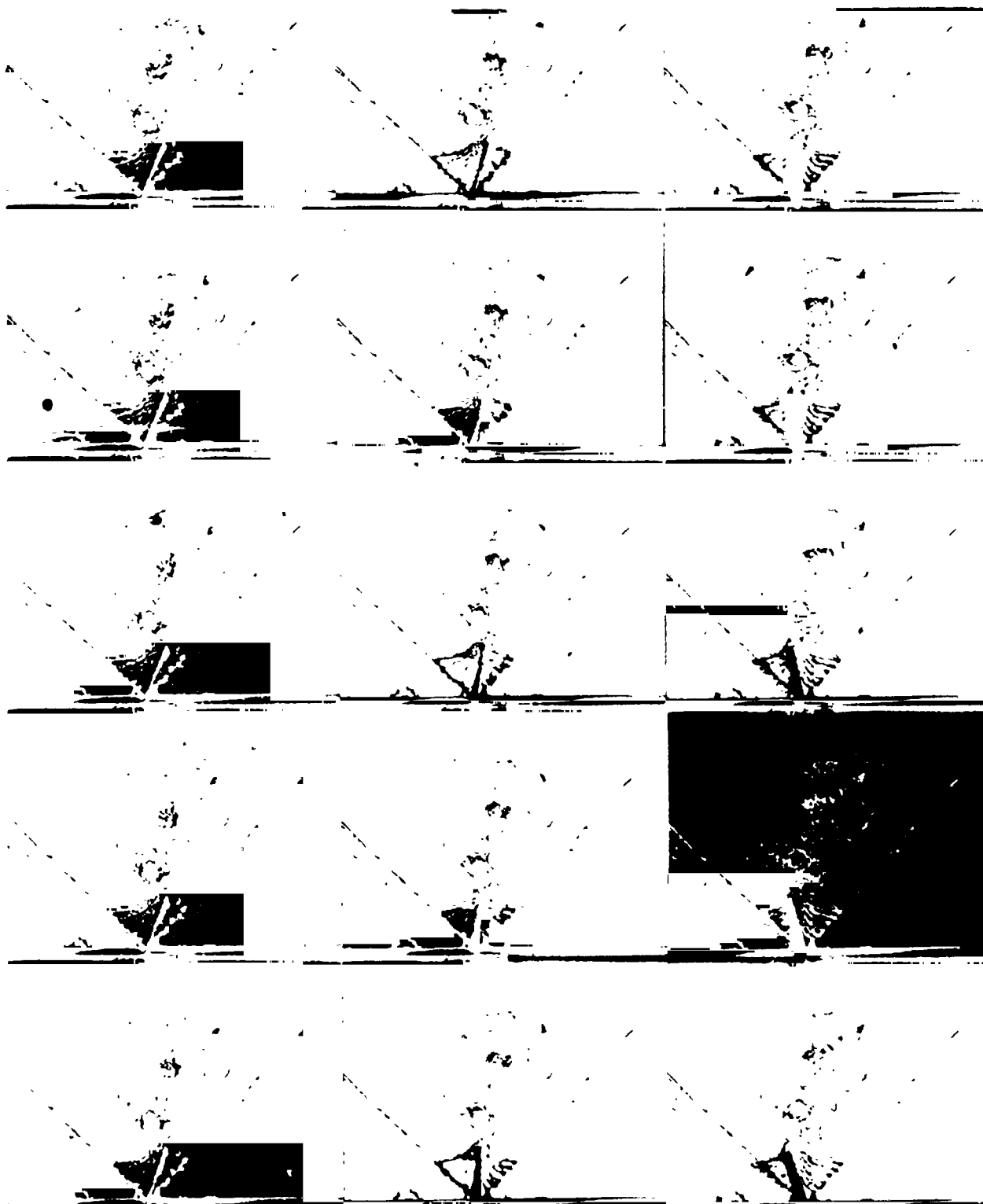


Figure 29, continued

frame #31

36

41

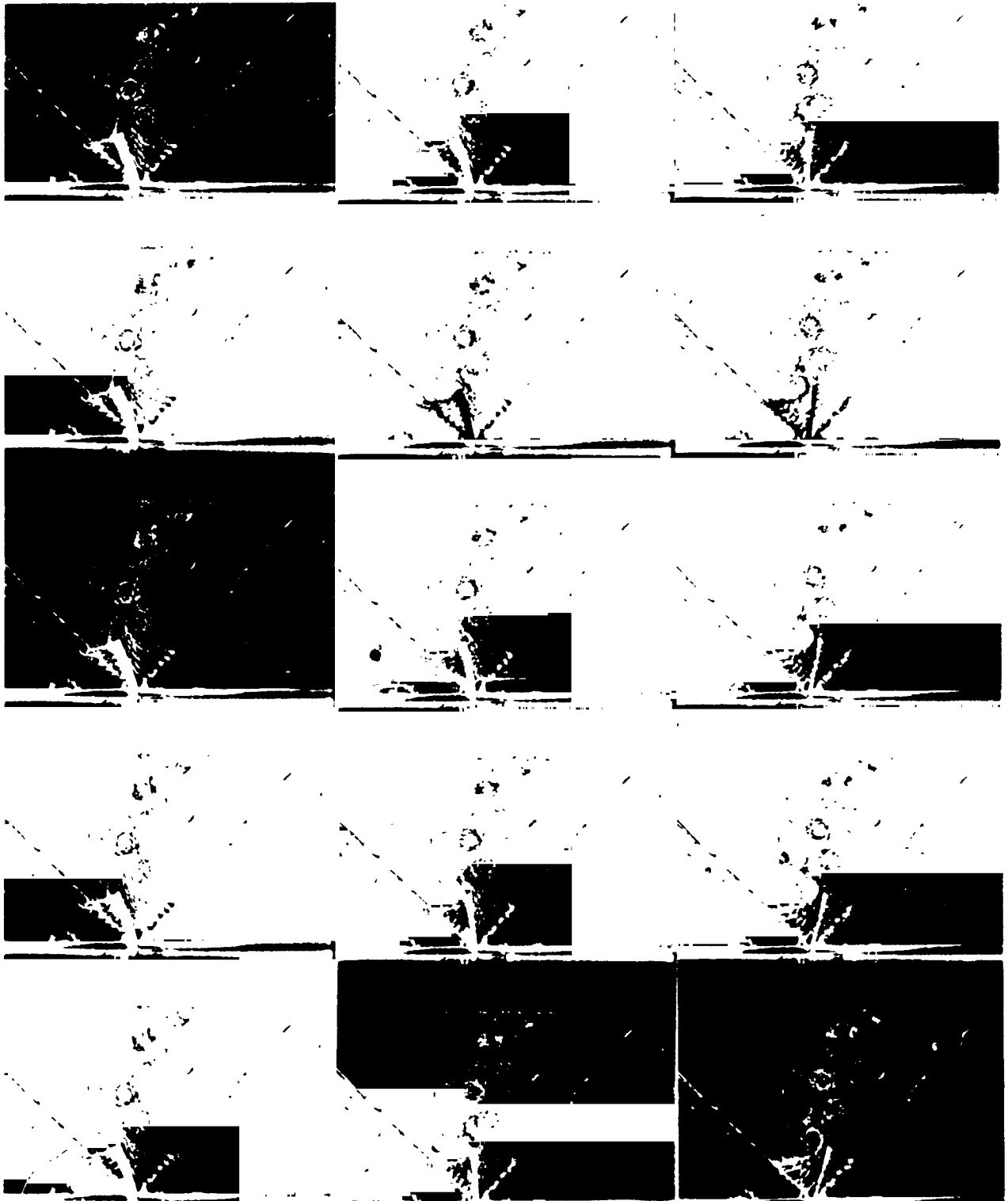


Figure 29, continued

frame #46

51

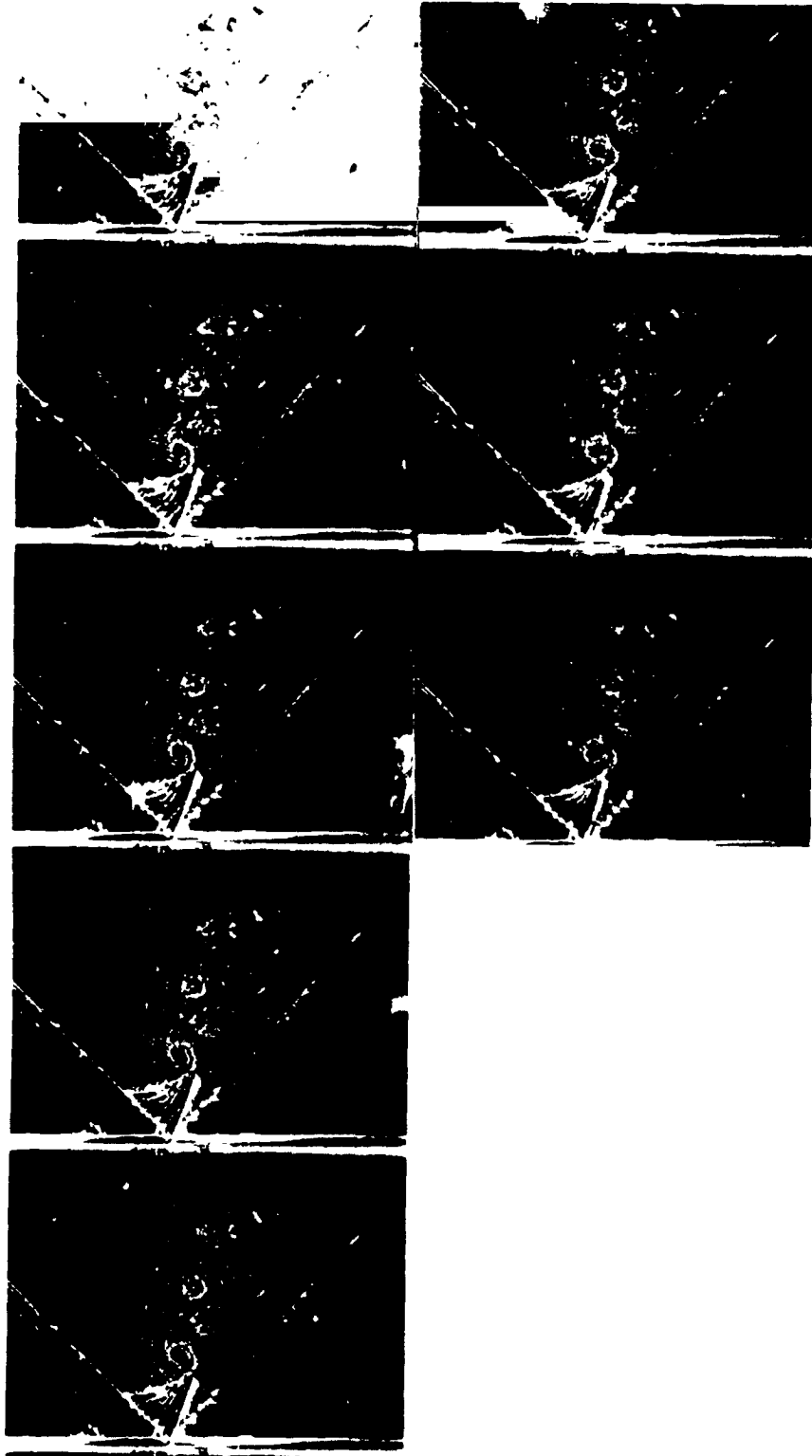


Figure 29, Continued

# DISPLACEMENT (x,y) vs TIME. (.001) MYLAR - $UT/D = 0.79$

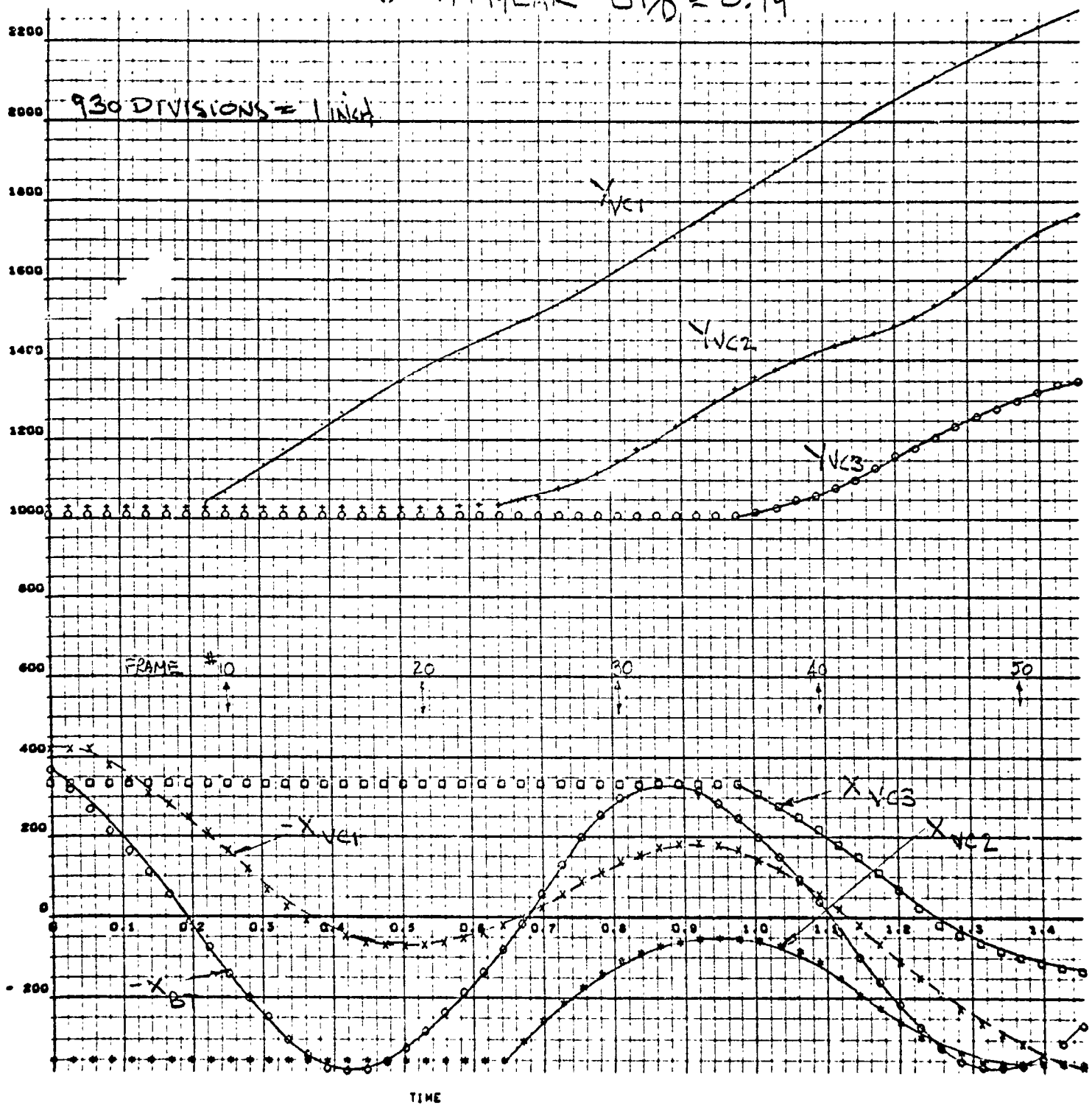


FIGURE 30

# VELOCITY VS TIME

(.001) MYLAR,  $U_{TD} = 0.79$

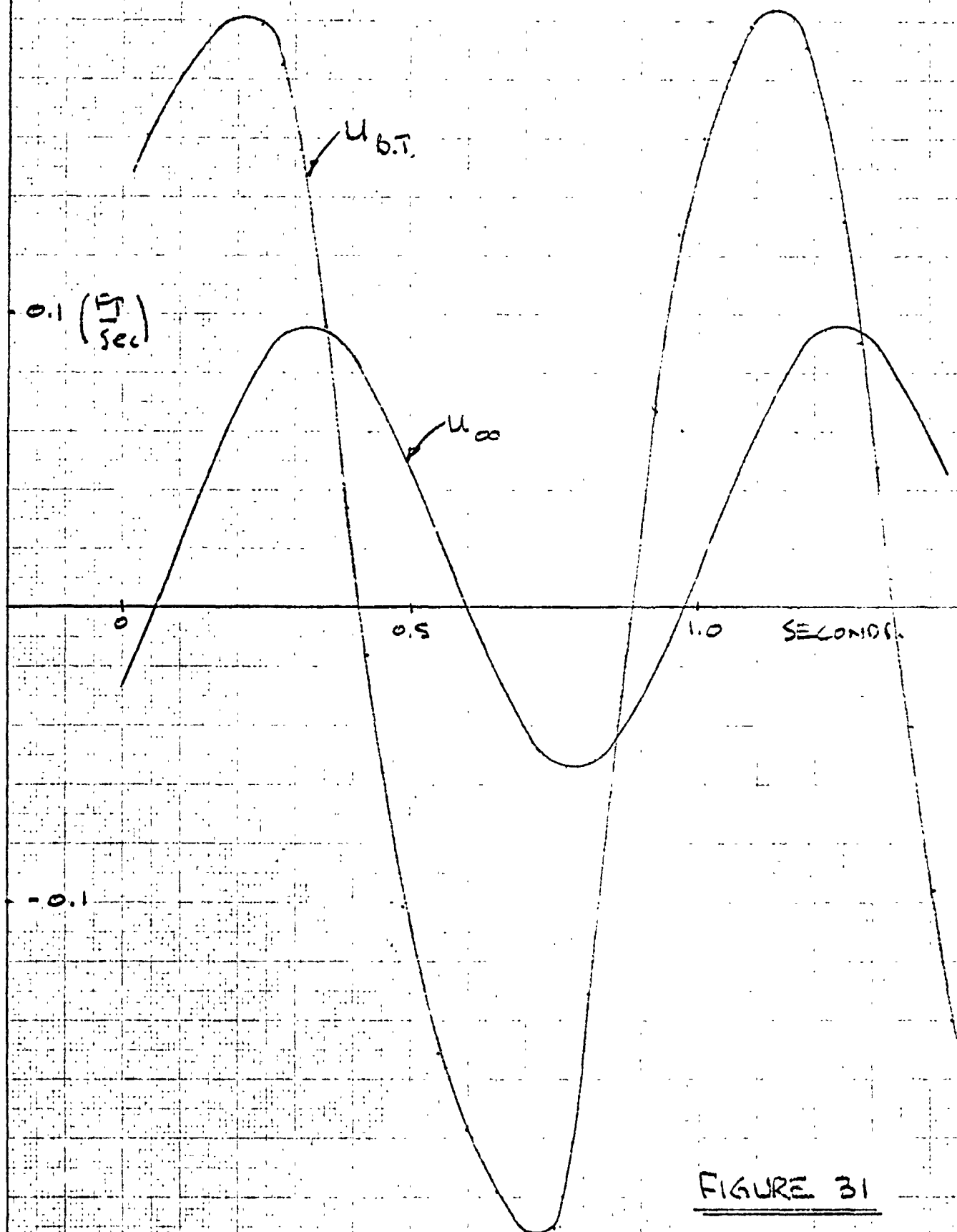


FIGURE 31

J

2. Division - 100

Q. IS THE MIRROR

... CASE OF FIGURE 29

1. The first step is to identify the problem or question that needs to be answered. This involves understanding the context and the specific requirements of the task.

7-10-6

2002-2003

FRAME# 8

BATTLE TIP ✓  
(AT MAX. 4)

-FRANCESCO

FIGURE 32

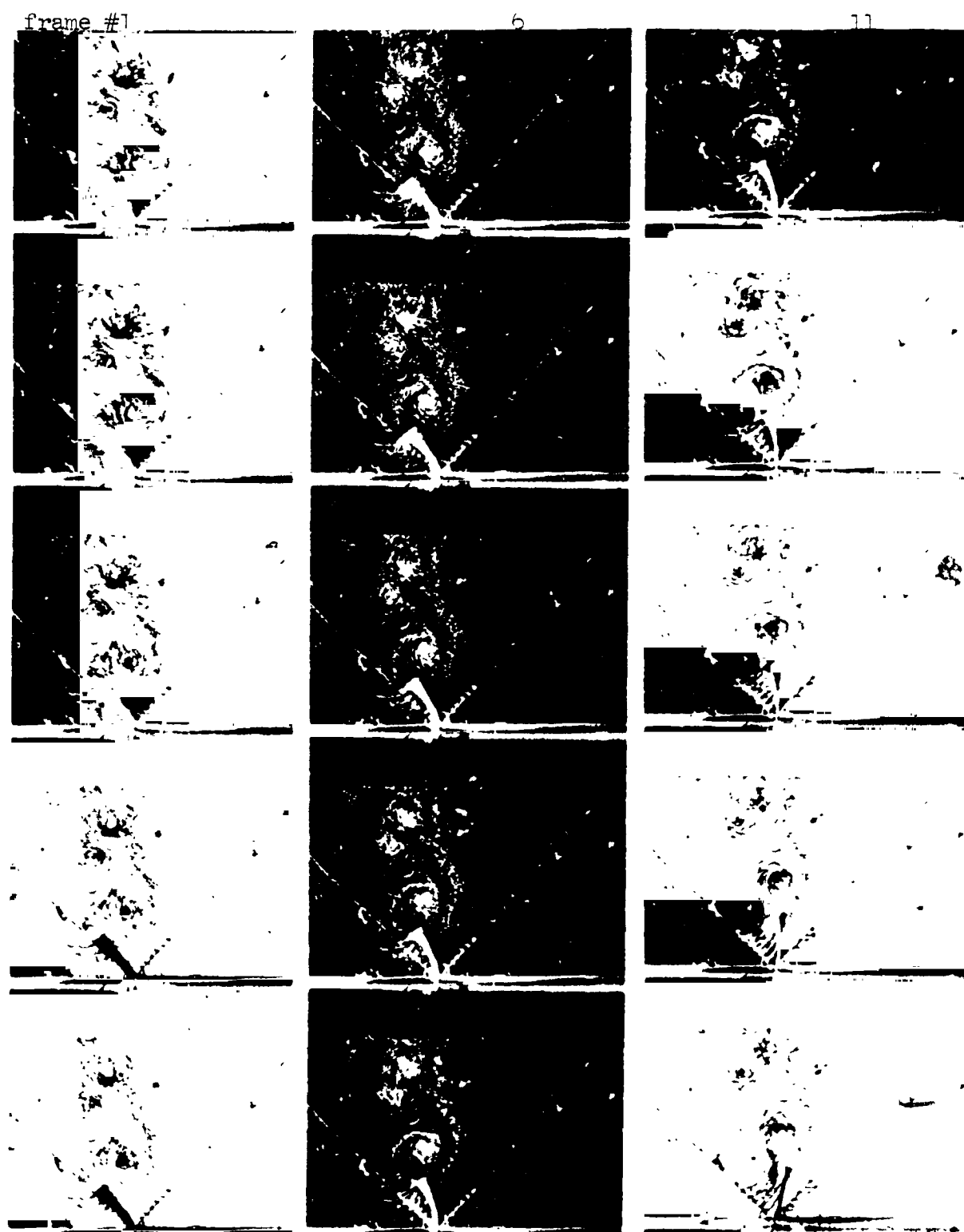


Figure 33 16 mm Motion Picture Sequence, 32 frames/second  
 Type I, 1 X .001 inch mylar baffle, 0.88 seconds/cycle  $UT/D = 1.80$   
 $F = 0.137$

frame #16

21

26

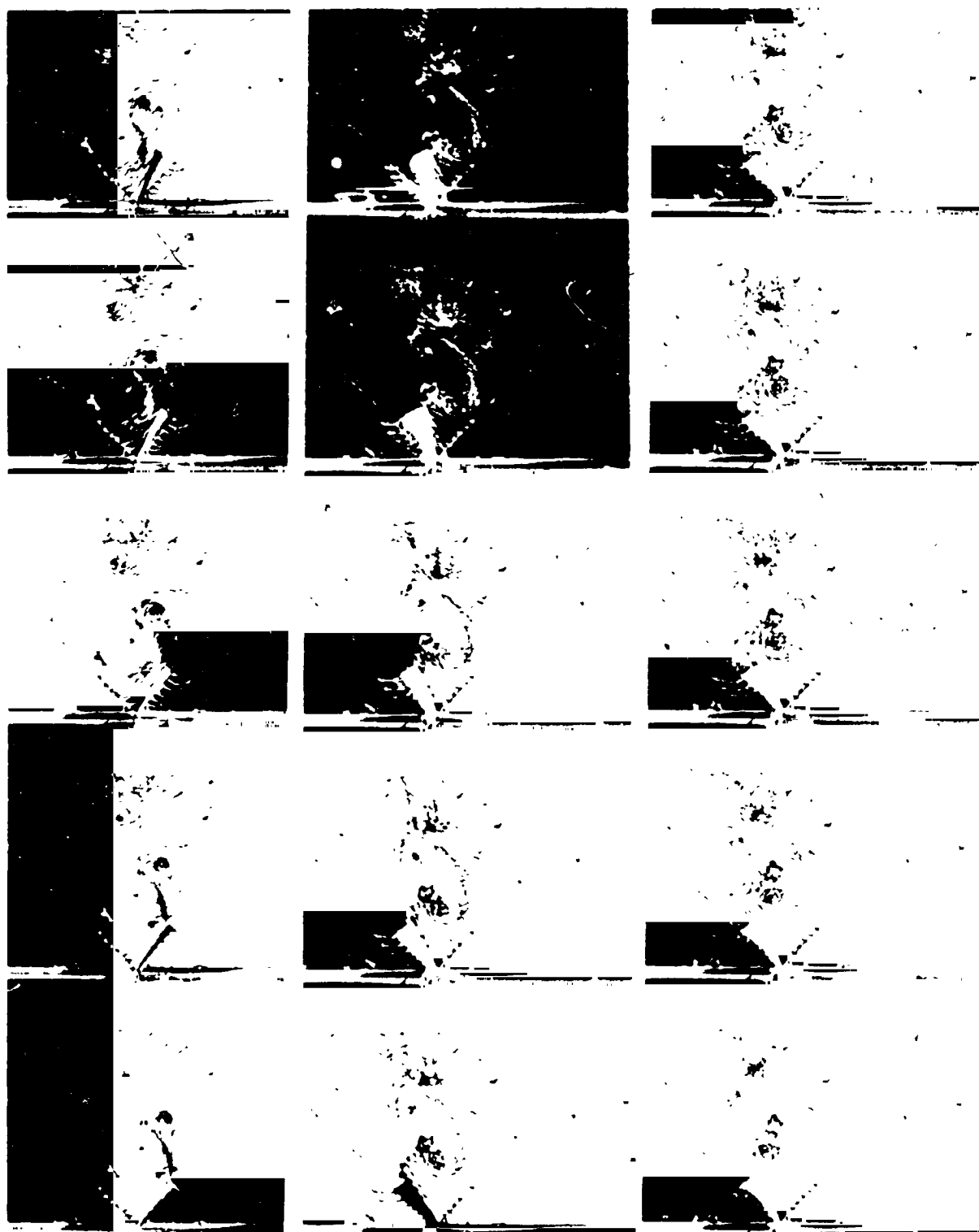


Figure 33, continued



frame #31

36

41

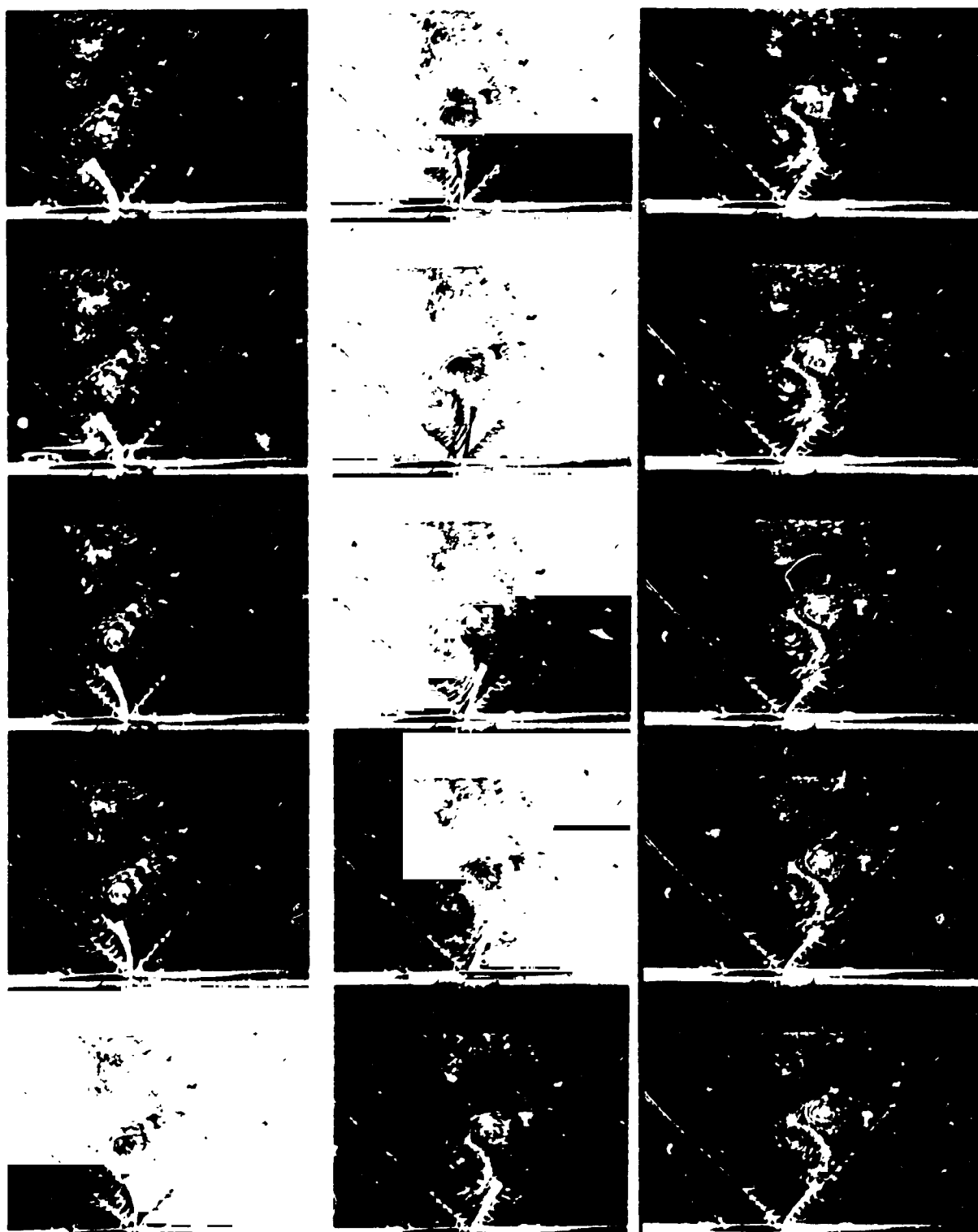


Figure 33, continued

# DISPLACEMENT (x & y) VS TIME.

(.001) MYLAR,  $UT/D = 1.80$

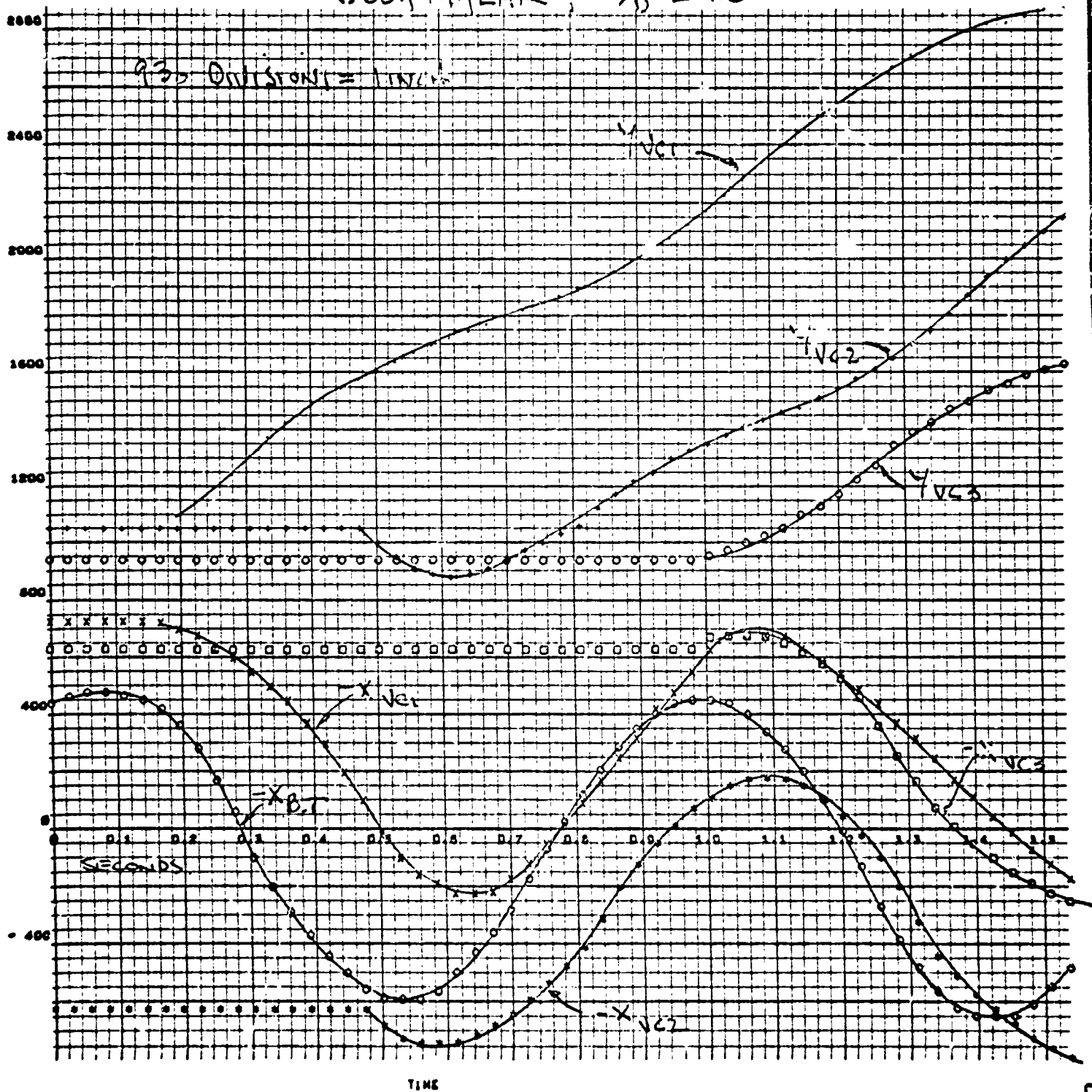


FIGURE 34

# VELOCITY VS TIME

(.001) MYLAR

PERIOD PARAMETER = 1.30

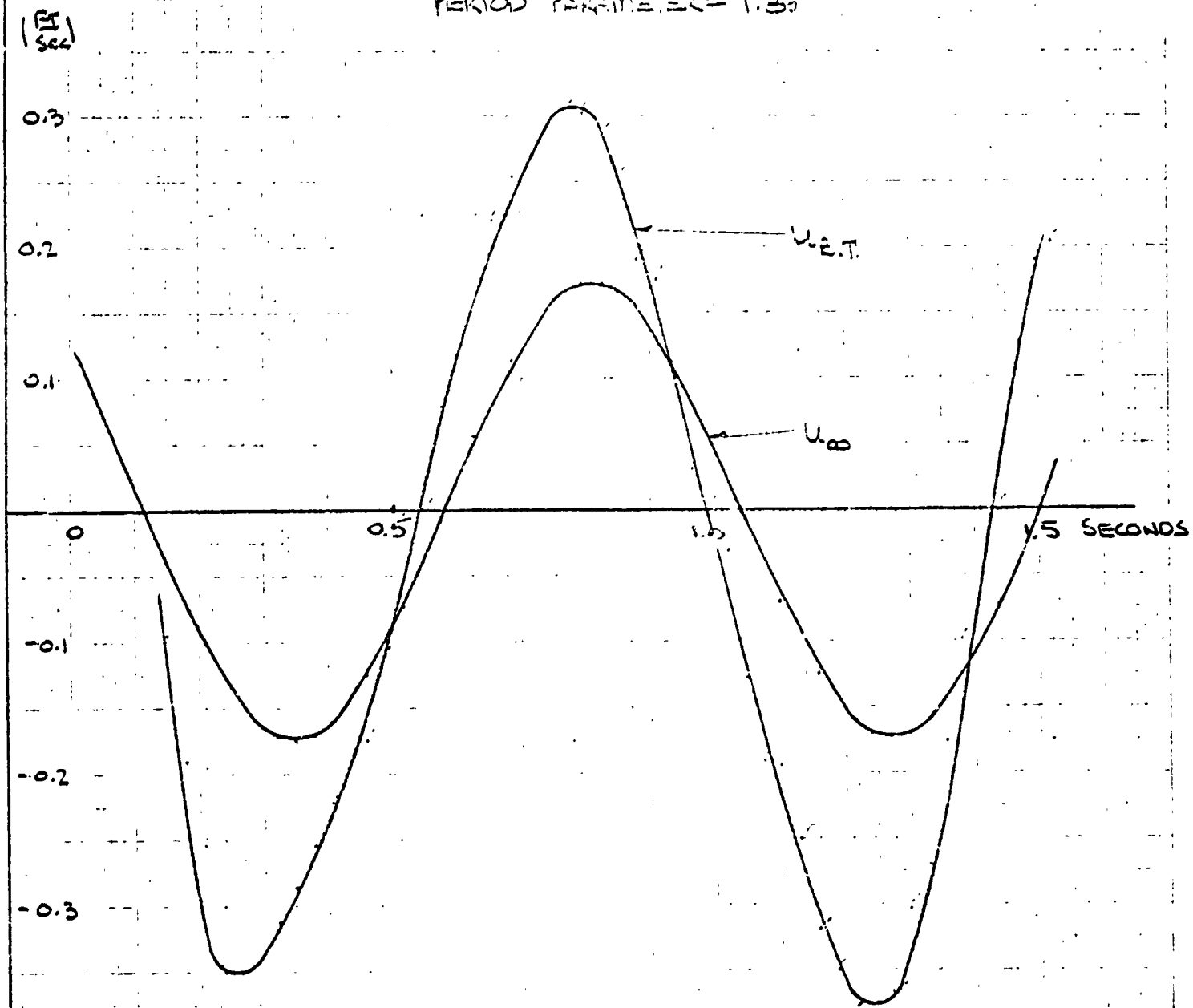


FIGURE 35

BUFFLE TIP AND  
 VORTEX CENTER  
 0.001 MYLAR,  $U_{\infty} = 1.80$

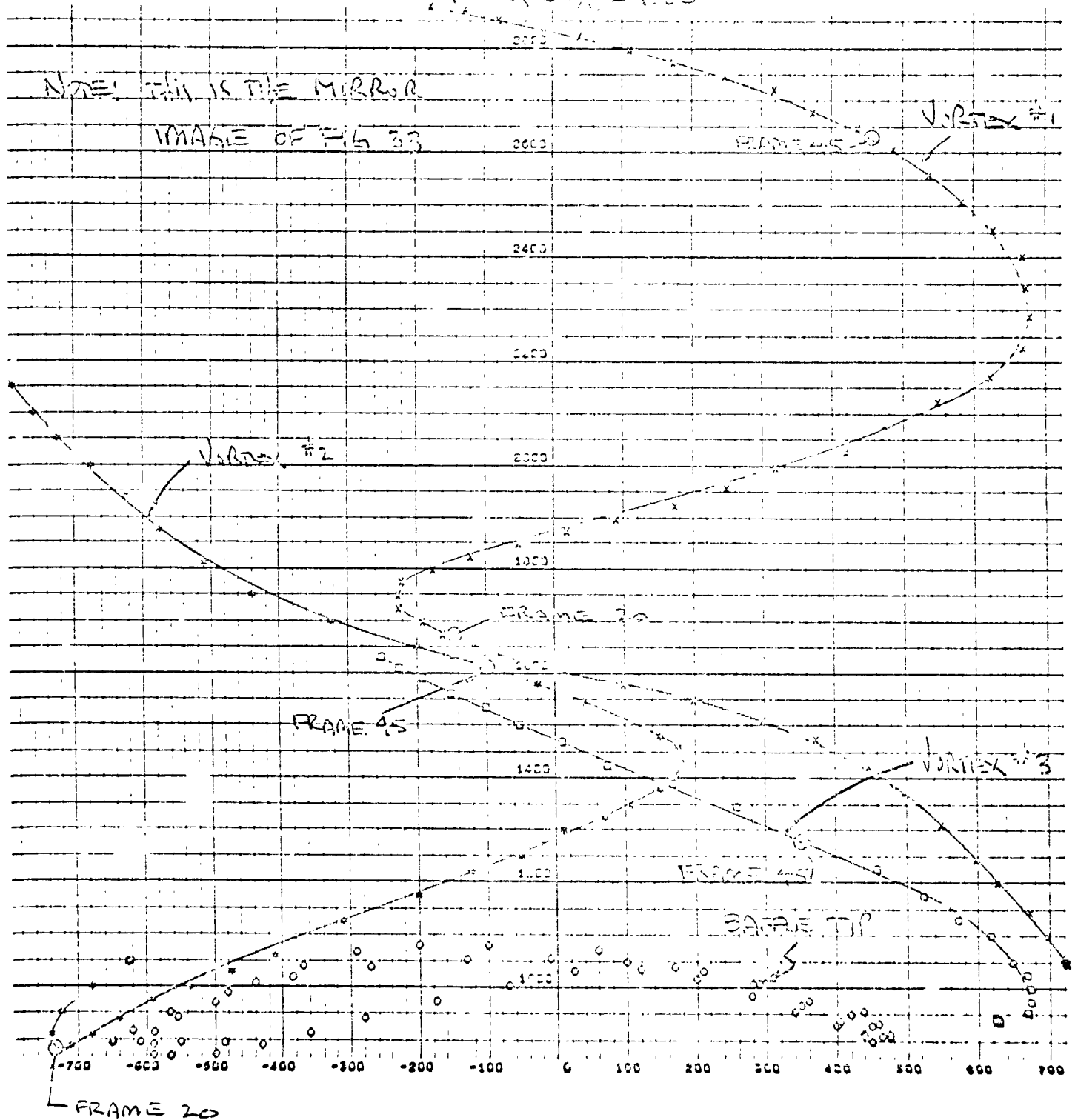


FIGURE 36

Frame #1

6

11

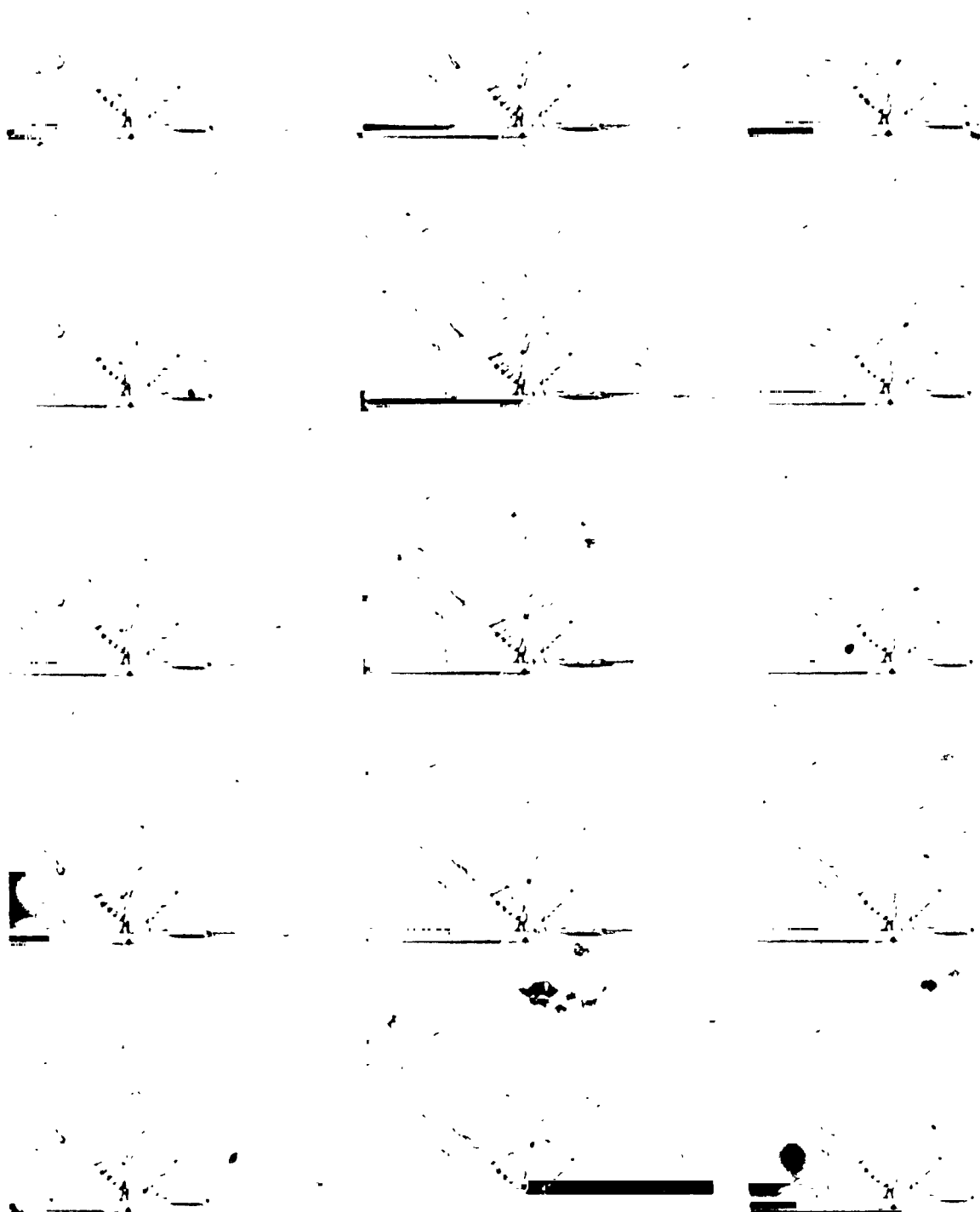


Figure 37 16 mm Motion Picture Sequence, 32 Frames/Second  
Type I, 1 X .001 inch stainless steel baffle, 0.88 seconds/cycle  
 $UI/D = 0.79$ ,  $F = .00365$

frame #16

21

26

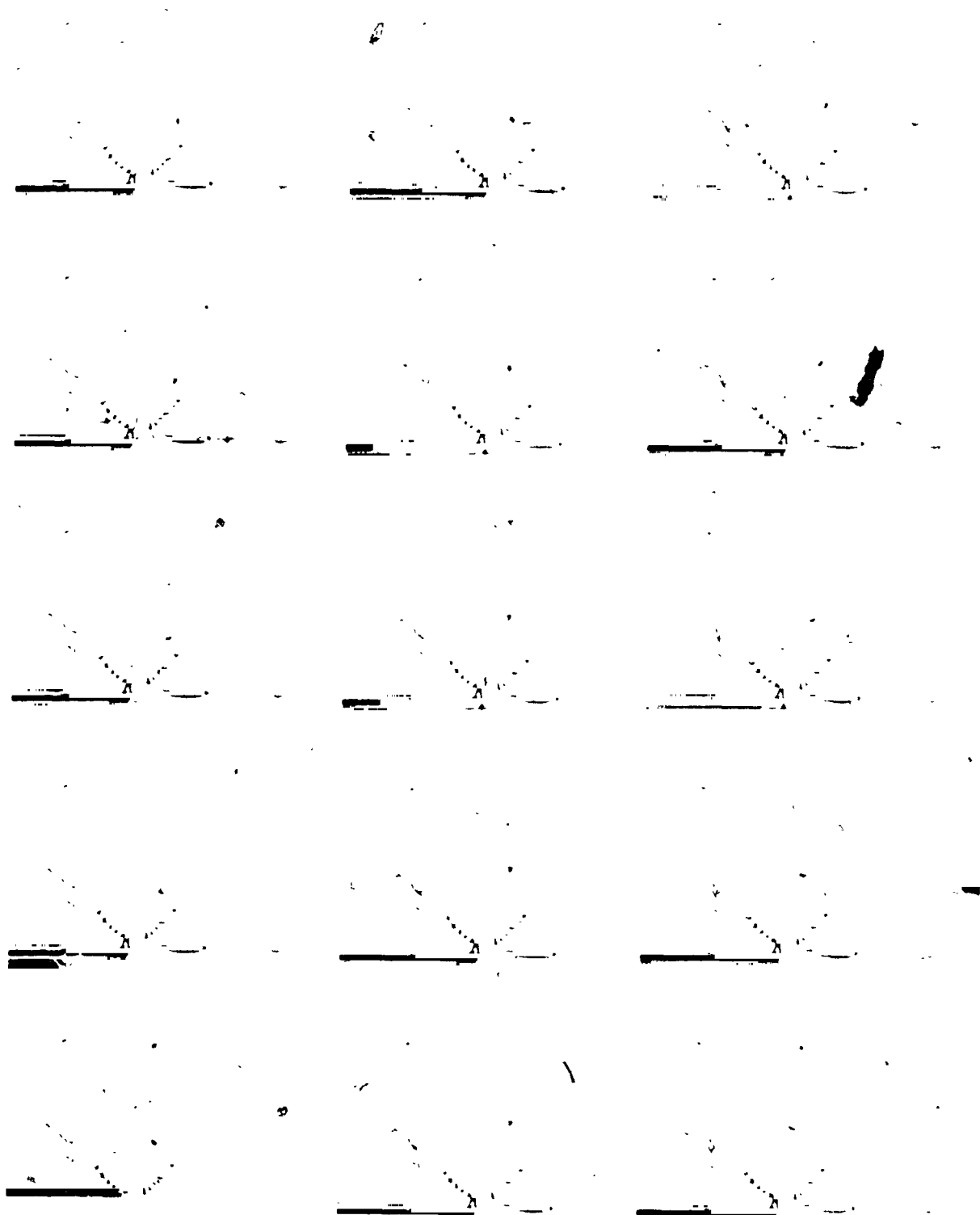


Figure 37, continued

frame #31

36

41

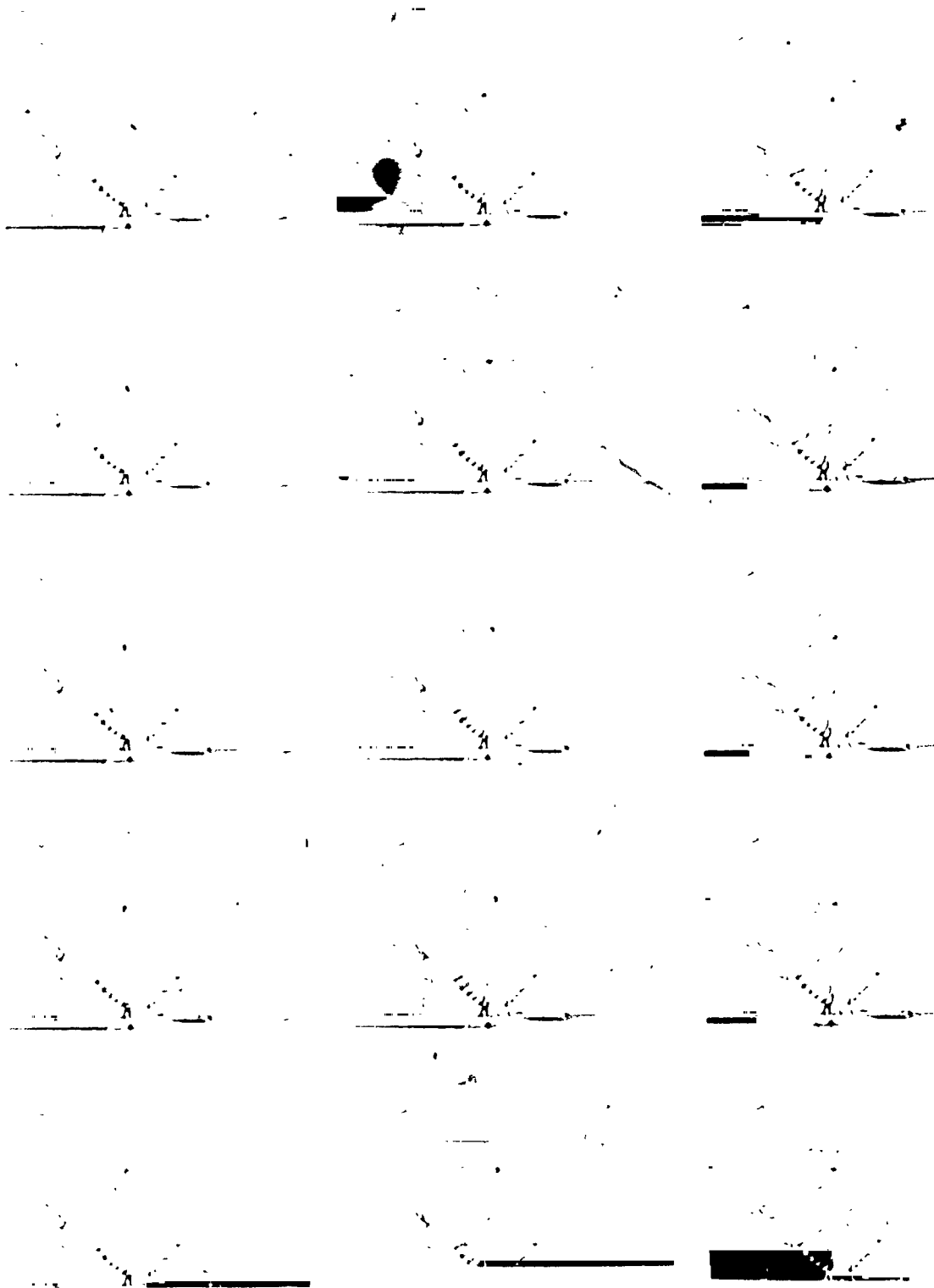


Figure 37, continued

frame #46

51

56



Figure 37, Continued



DISPLACEMENT (x4) vs TIME  
 (001) STAINLESS STEEL,  $UT_D = 0.79$

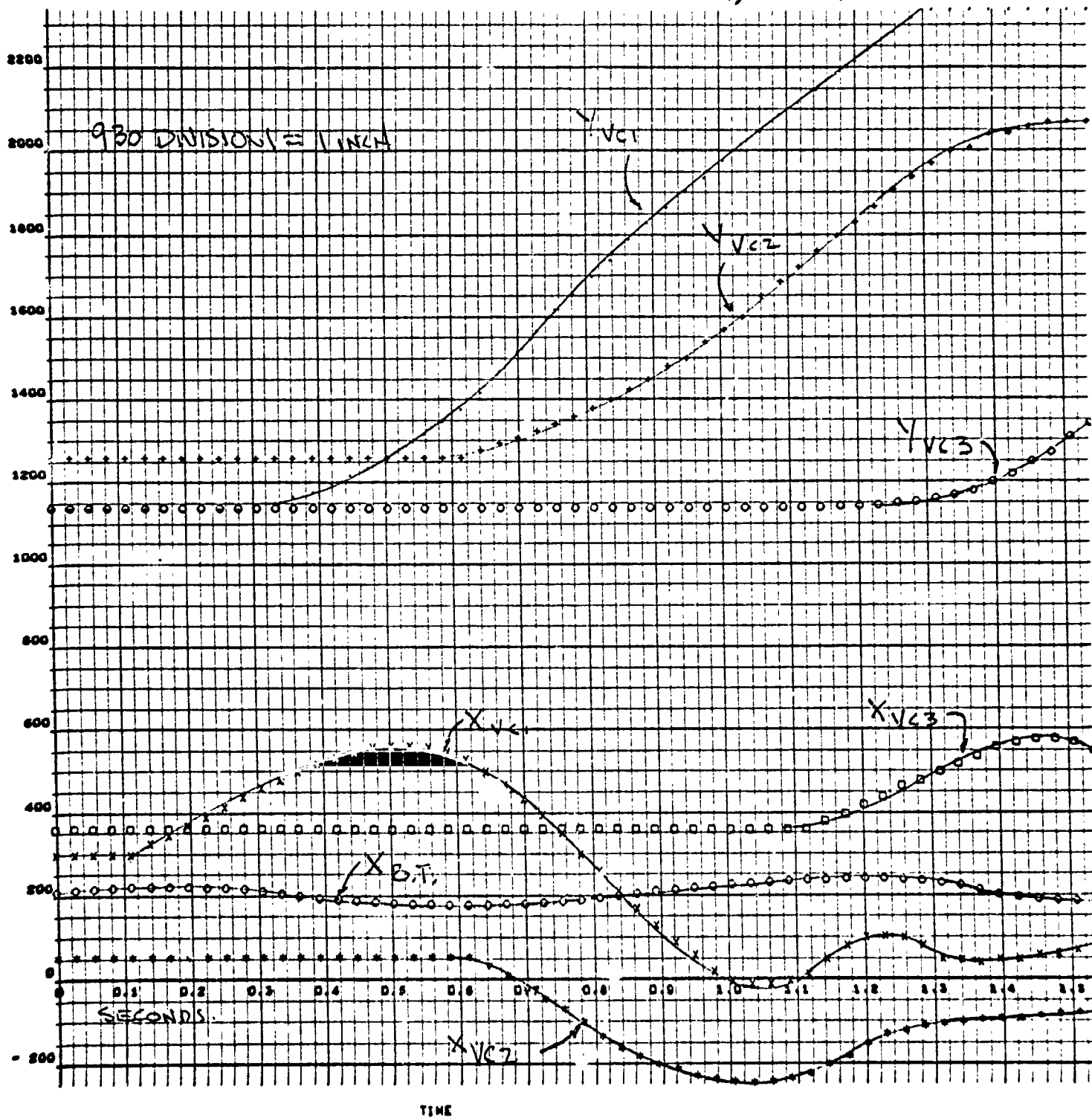


FIGURE 38

# VELOCITY VS TIME

(.001) STAINLESS STEEL

PERIOD PARAMETER = 0.79

FT/SEC

VELOCITY,  $\frac{FT}{SEC}$

0.1

0

0

0.5

1.0

1.5

SECONDS

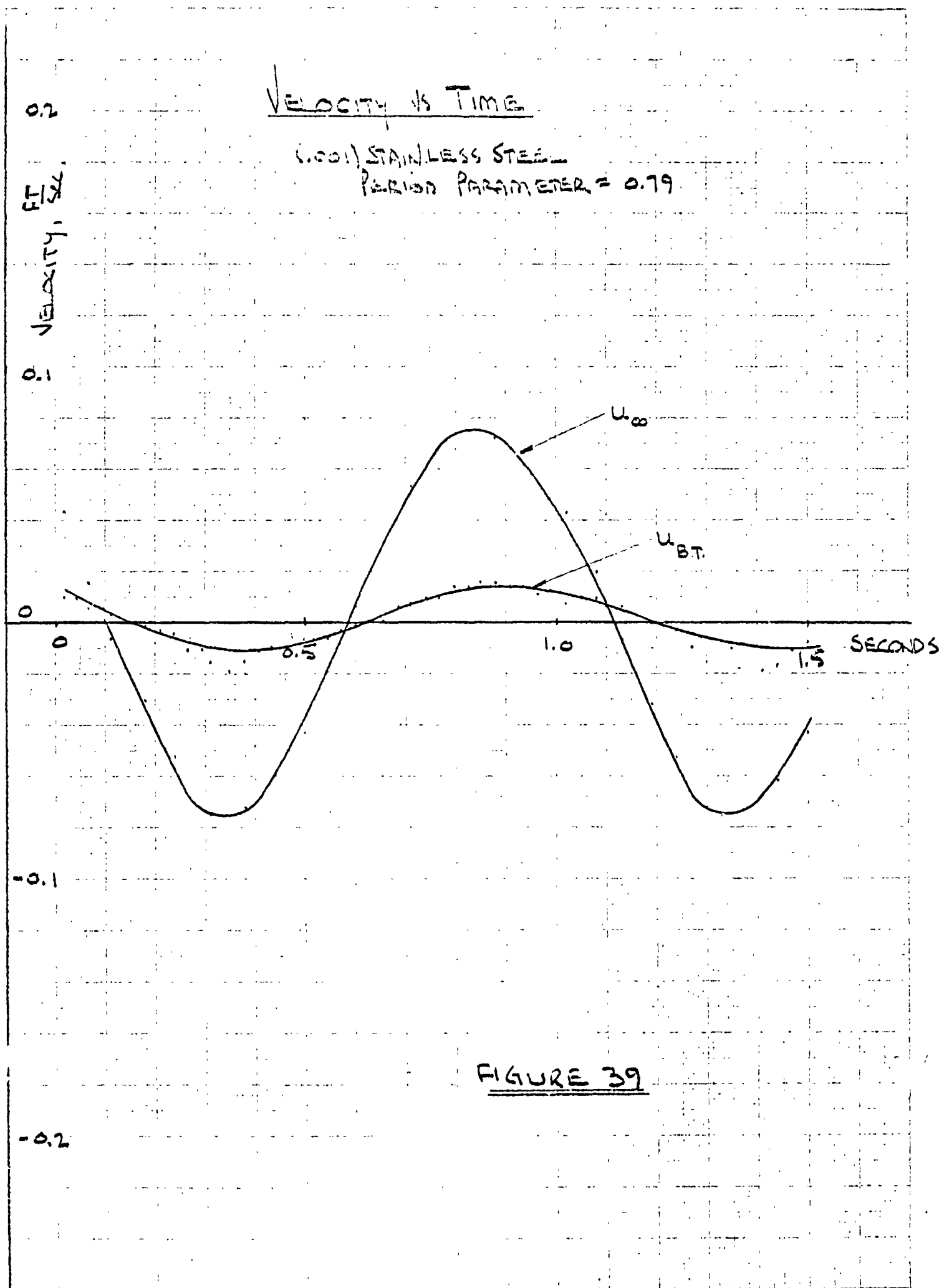
$u_{\infty}$

$u_{BT}$

-0.1

-0.2

FIGURE 39



# BAFFLE TIP AND

## VORTEX CENTER X VS Y

(C-001) STAINLESS STEEL,  $UT/D = 0.79$

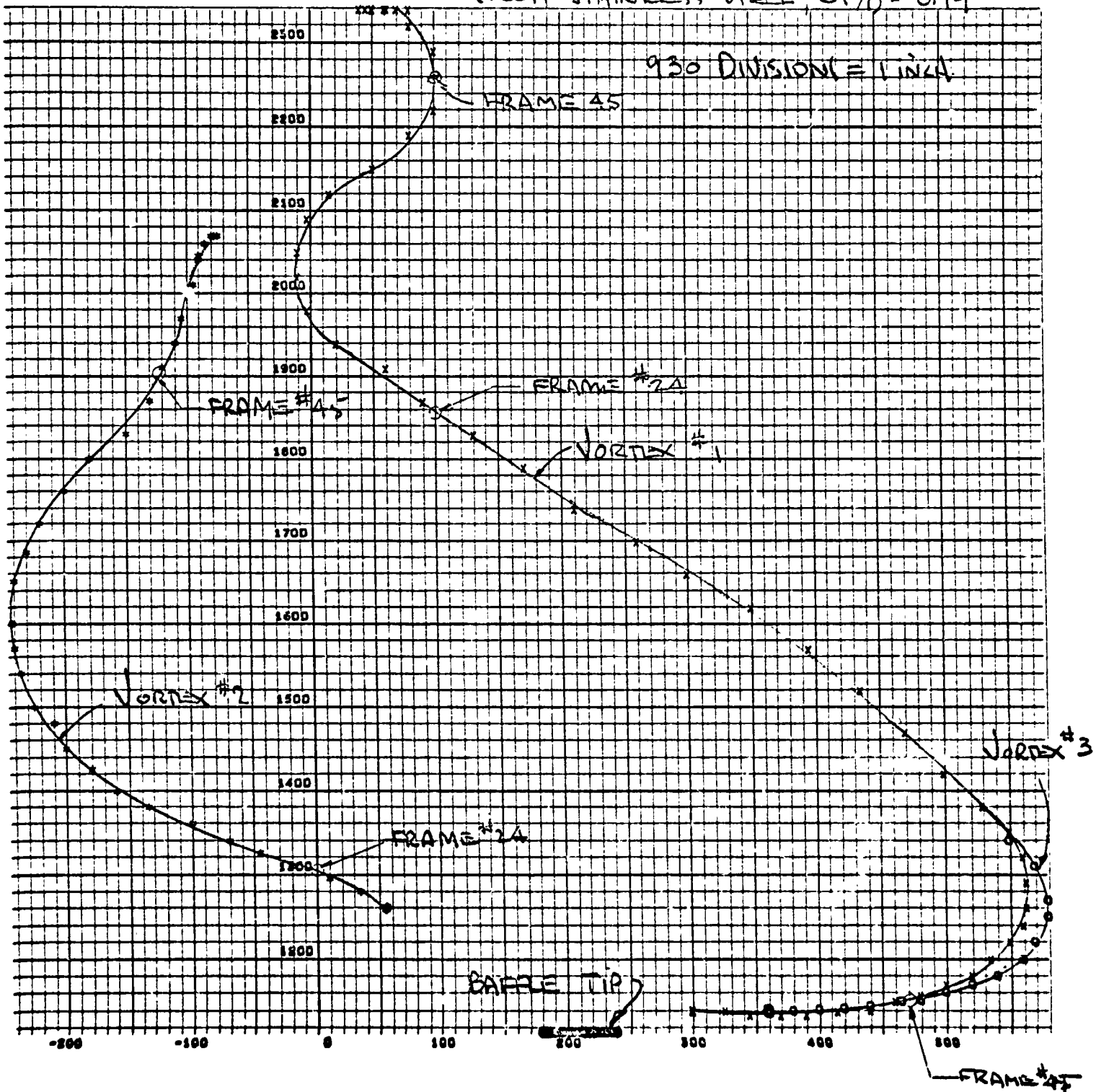


FIGURE 40

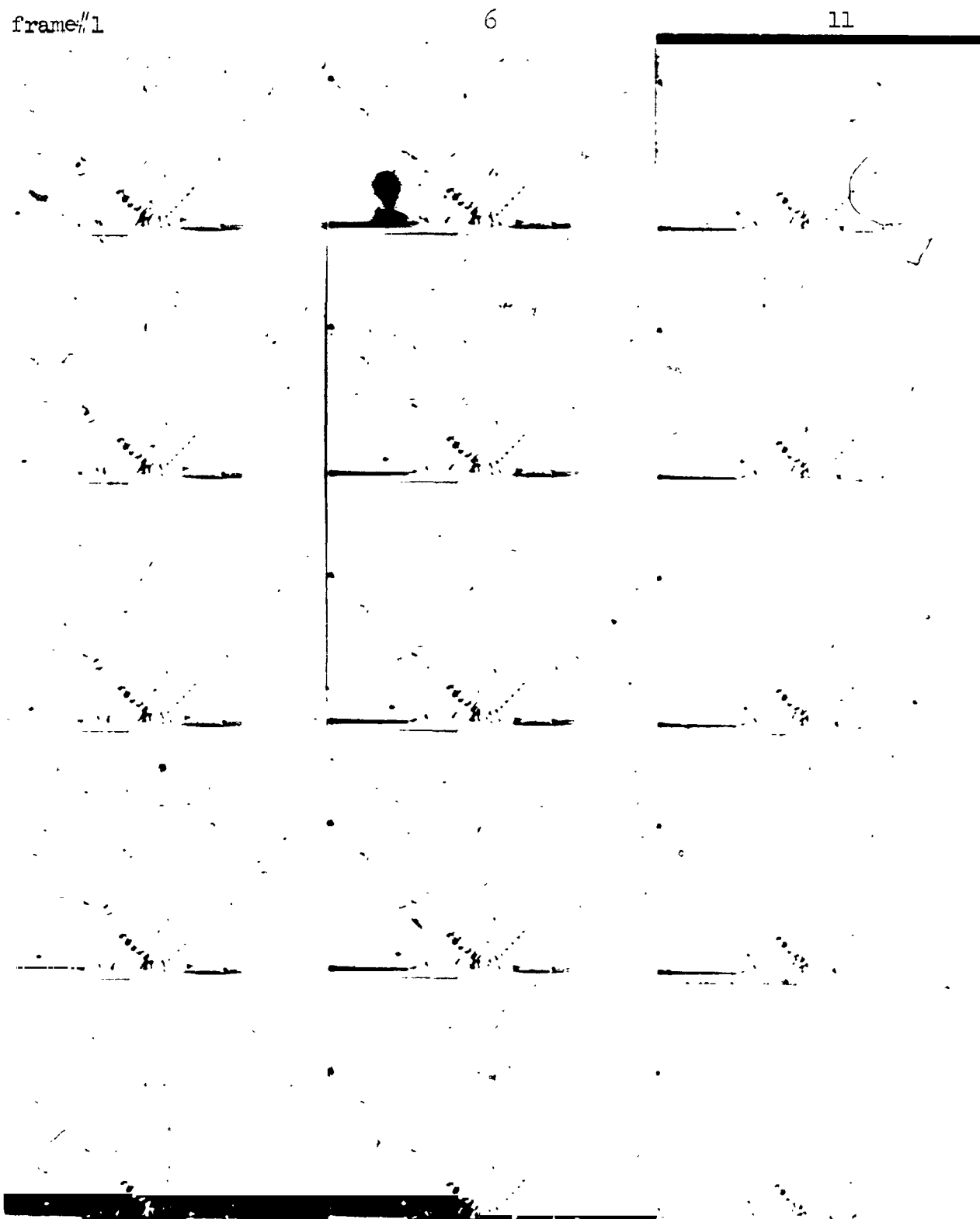


Figure 41 16 mm Motion Picture Sequence, 32 frames/second  
 Type I, 1 X .001 inch stainless steel baffle, 0.88 seconds/cycle  
 $UT/D = 1.80$ ,  $F = .00365$

frame #16

21

20

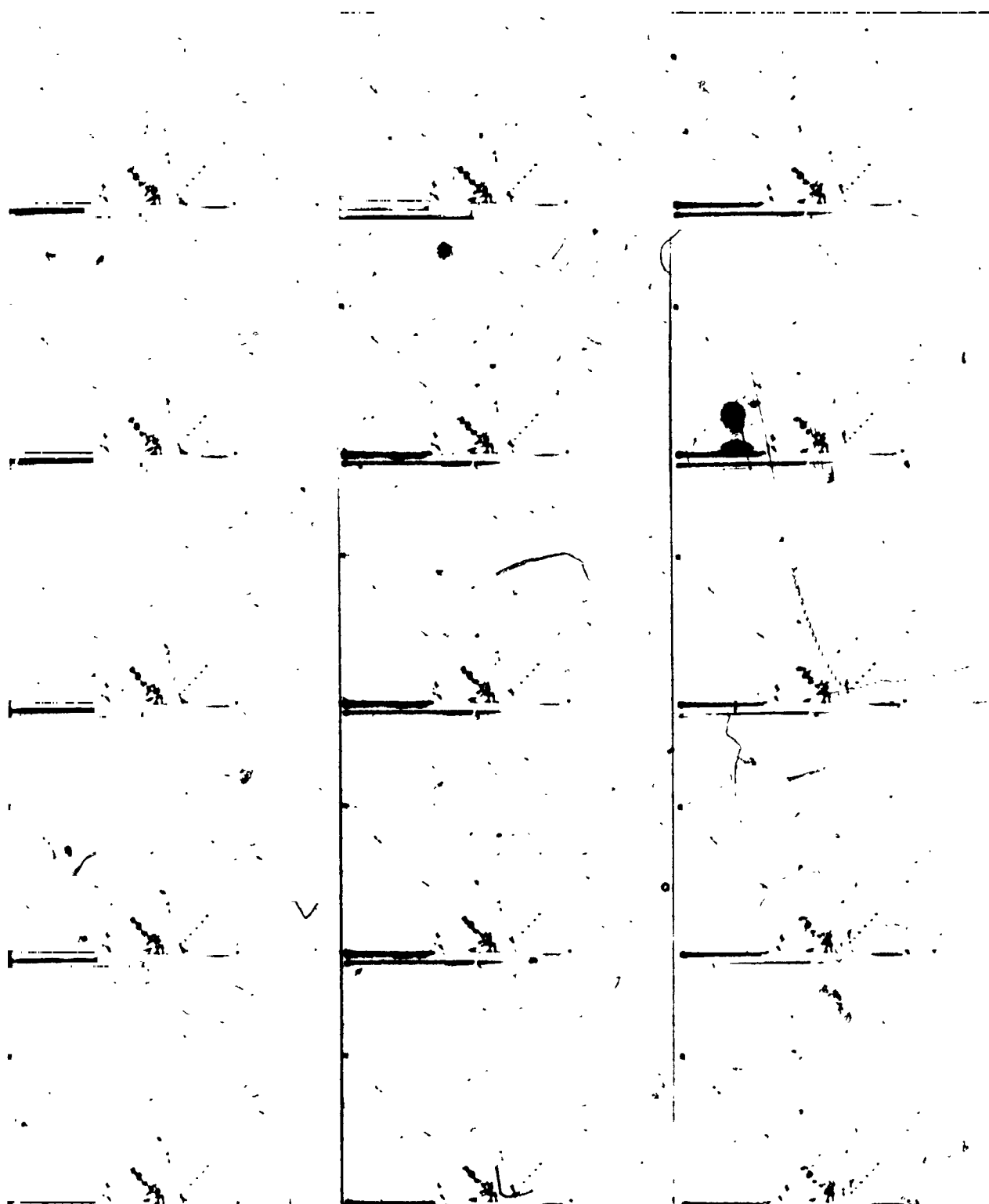


Figure 41, Continued

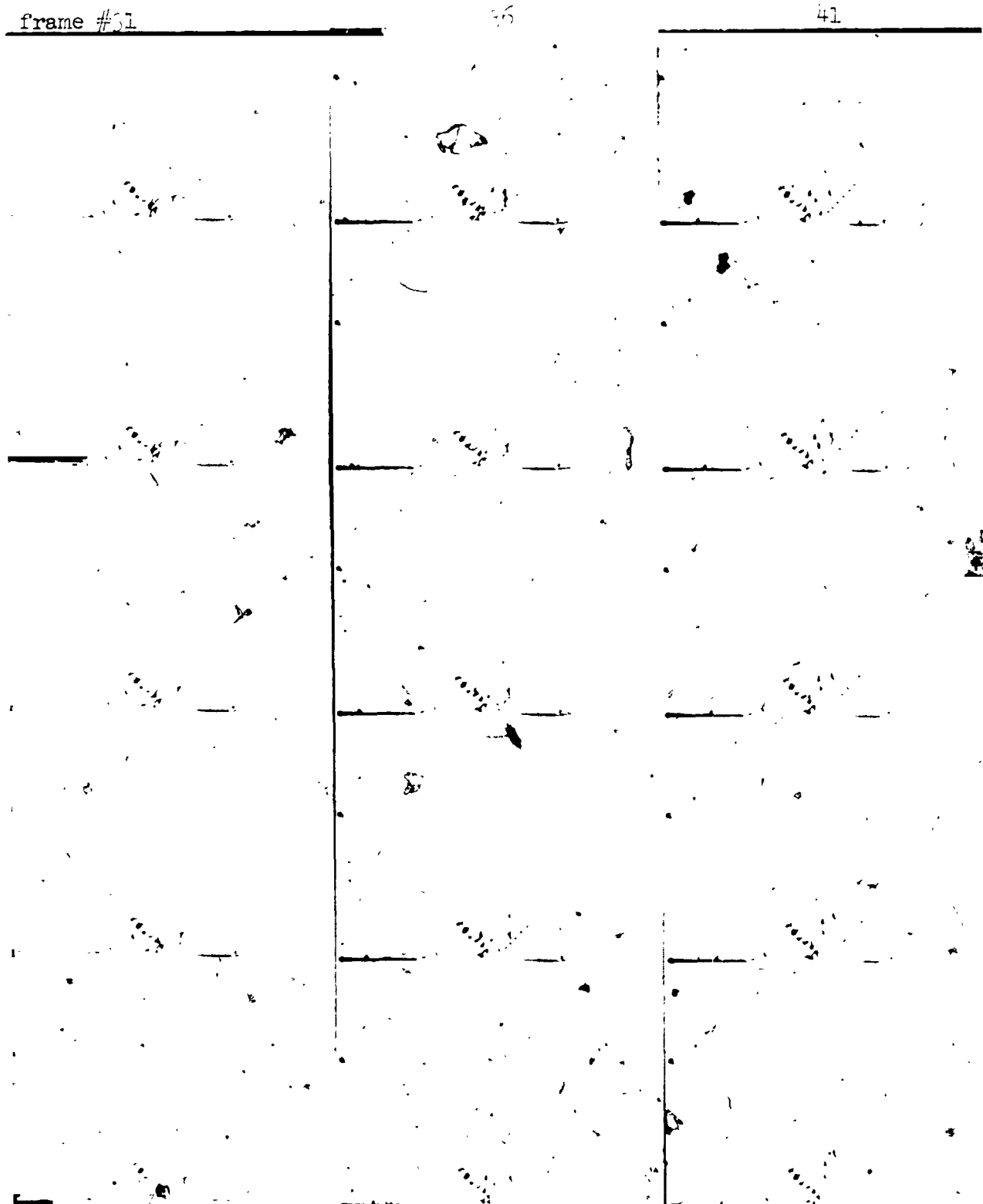


Figure 41, continued

frame #46

51

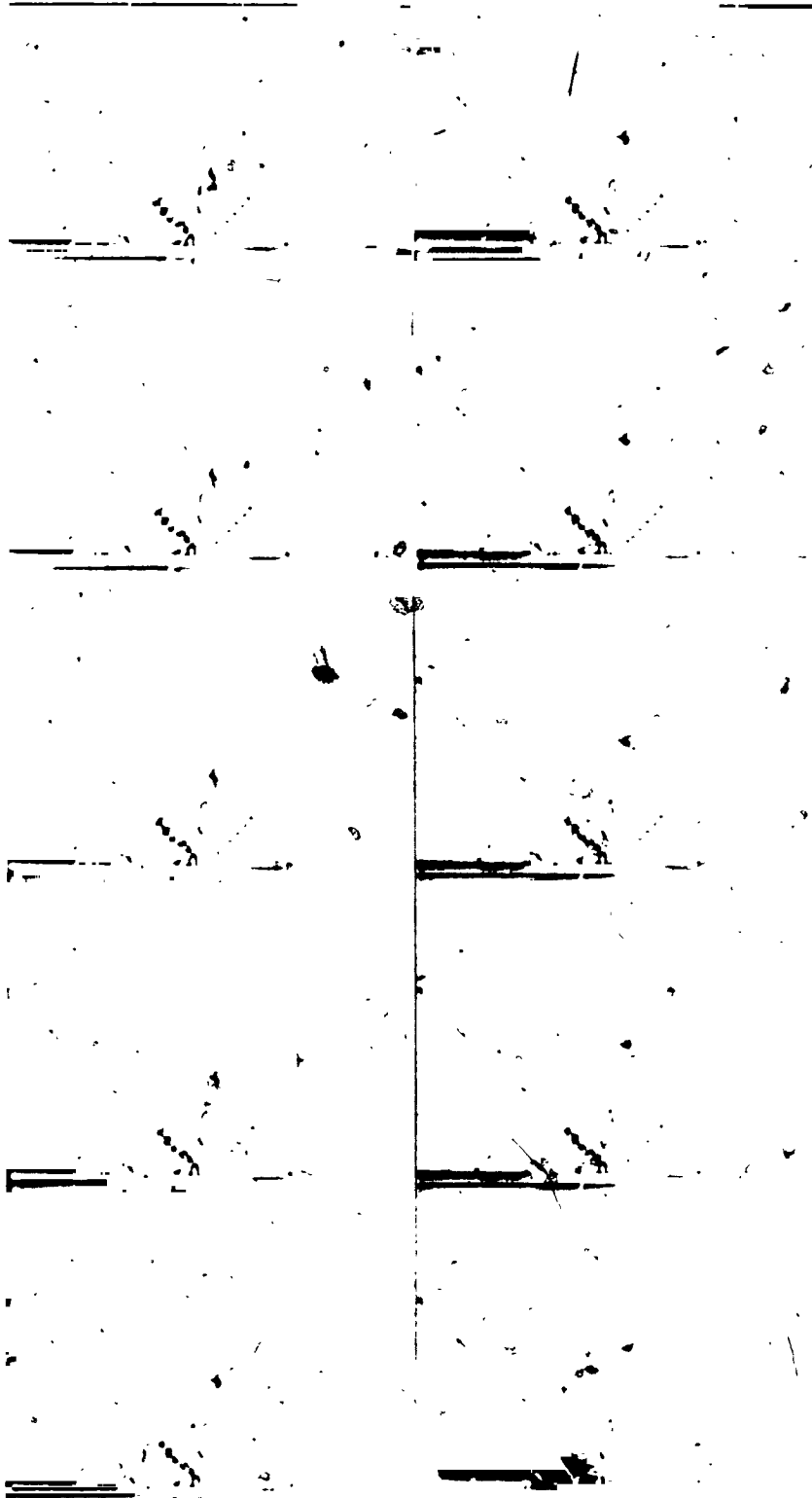


Figure 41, Continued

# DISPLACEMENT (x & y) VS TIME (.001) STAINLESS STEEL - $UT/D = 1.80$

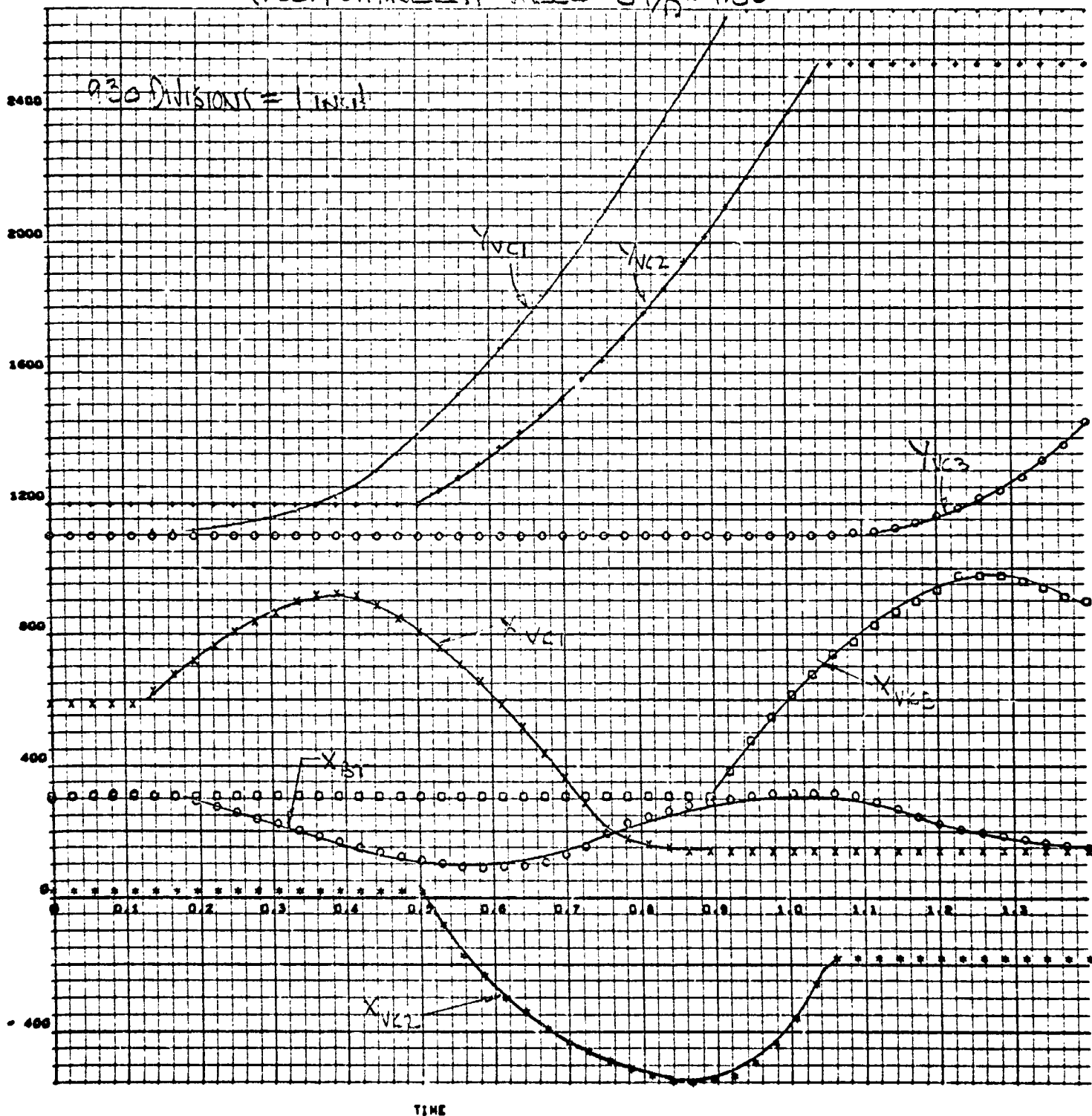


FIGURE 42



VELOCITY VS TIME

(.001) STAINLESS STEEL

PERIOD PARAMETER = 1.80

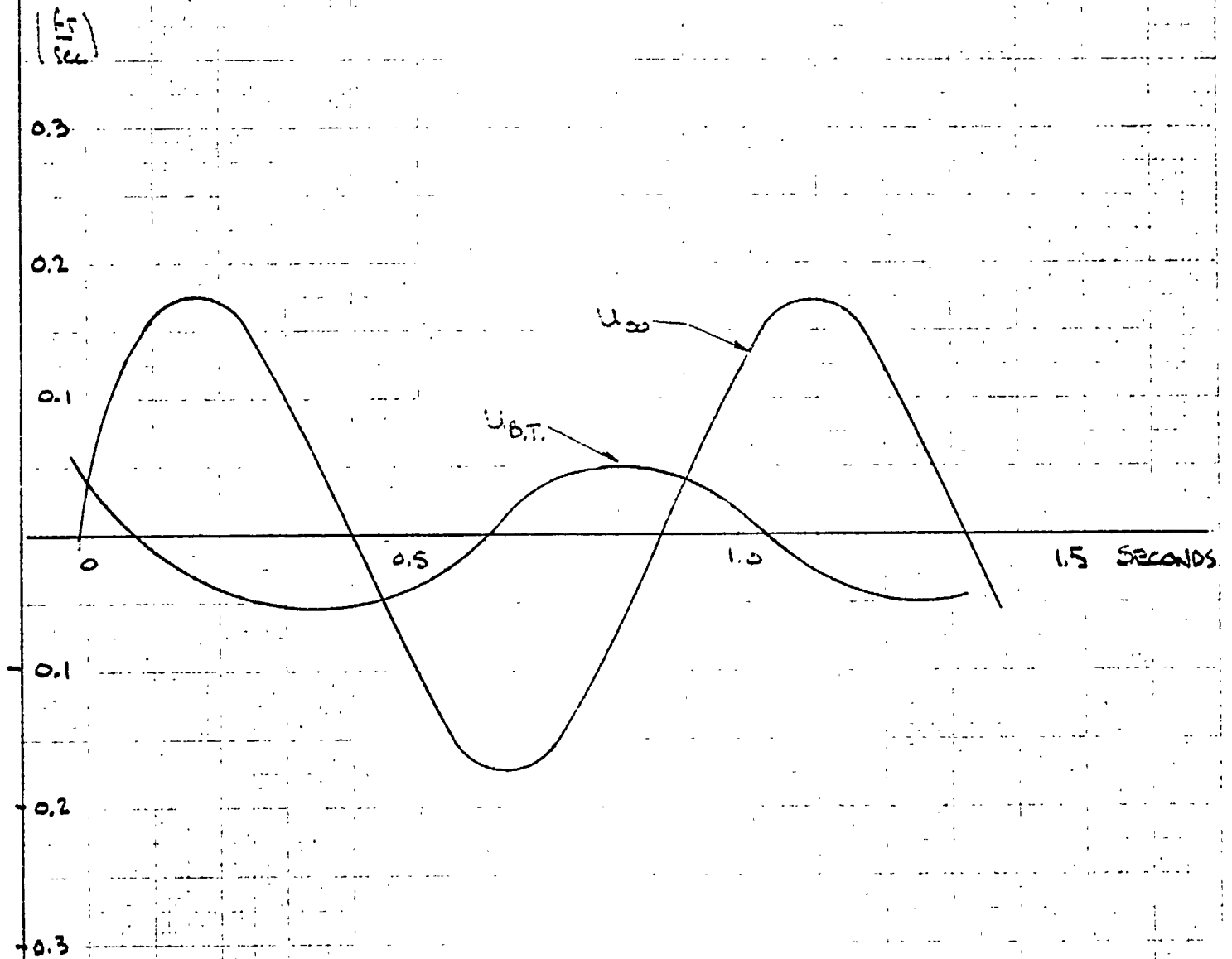


FIGURE 43

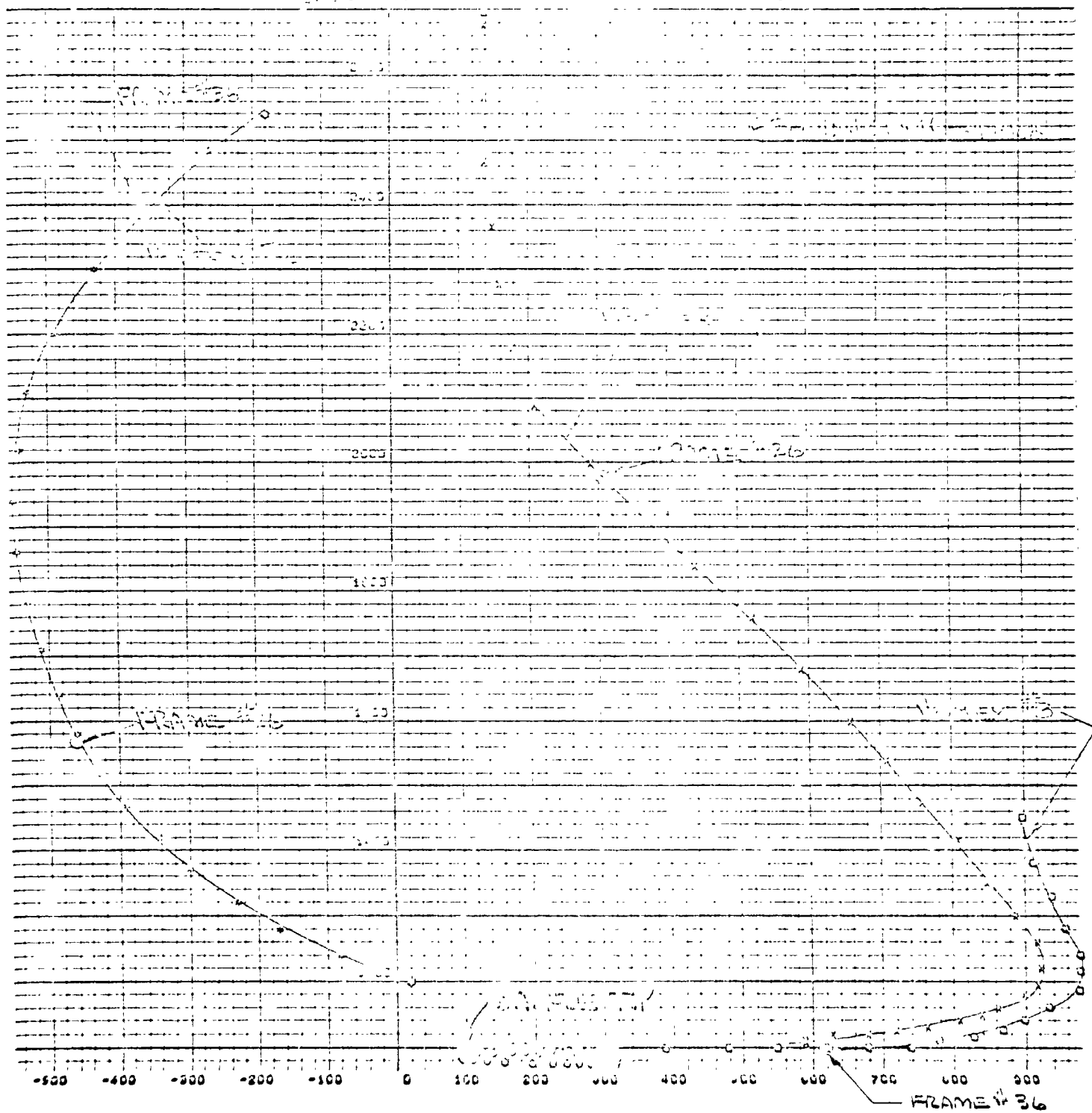


FIGURE 1.4

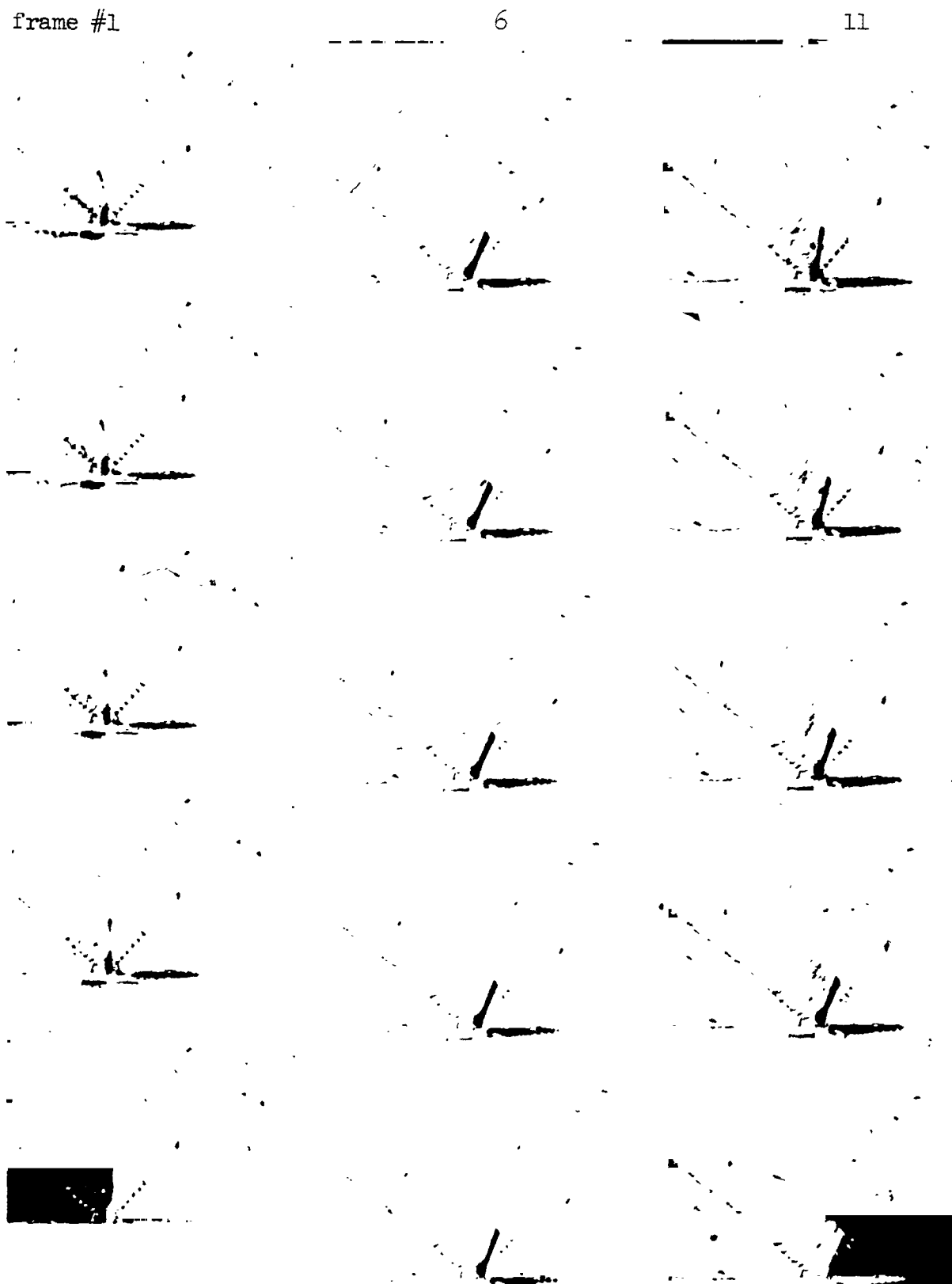


Figure 45 16 mm Motion Picture Sequence, 32 Frames/Second  
 Type II, 1 inch baffle, 0.88 seconds/cycle,  $UT/D = 1.80$ ,  
 $F = 0.164$

frame #16

21

26

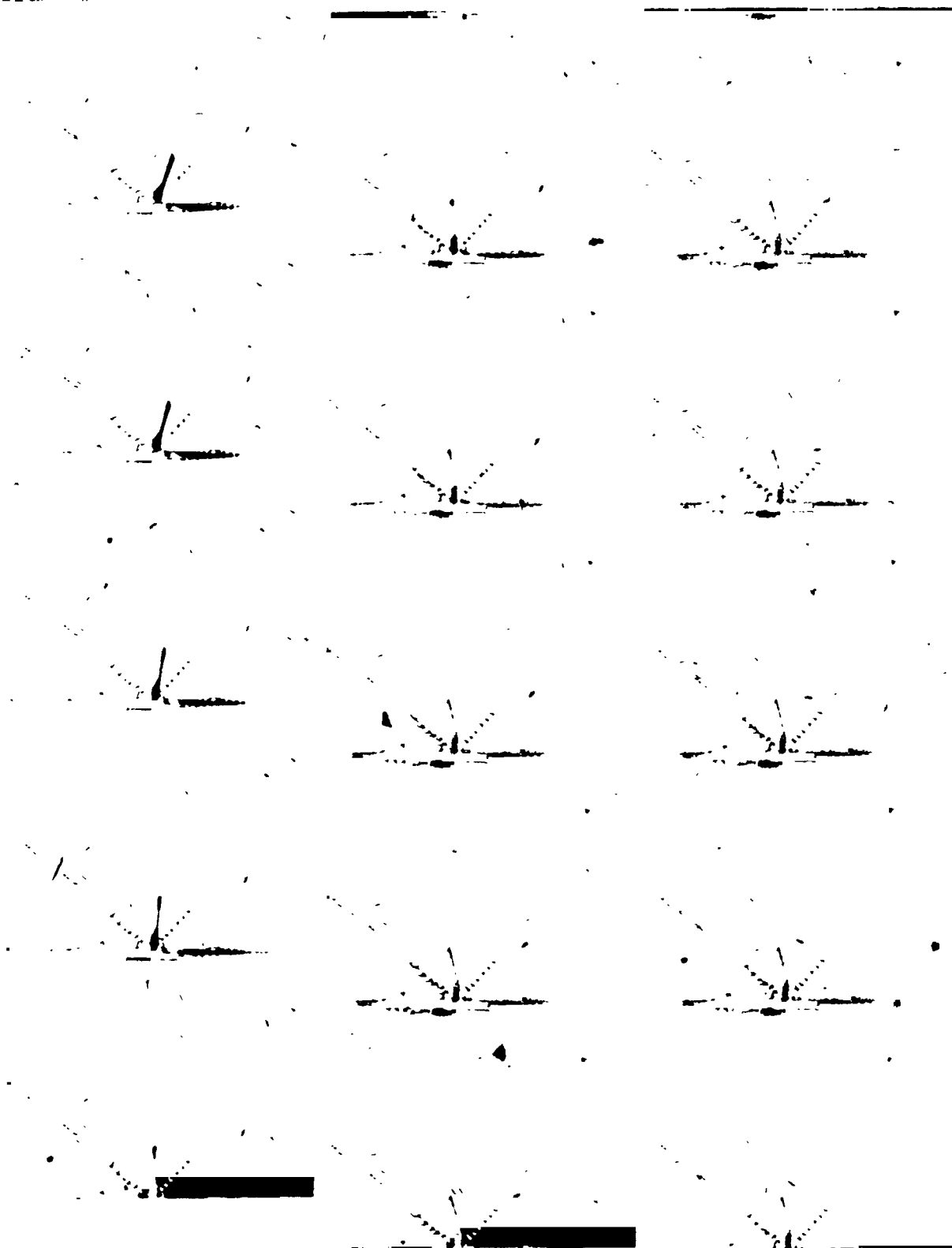


Figure 45, continued

frame #31

36

41

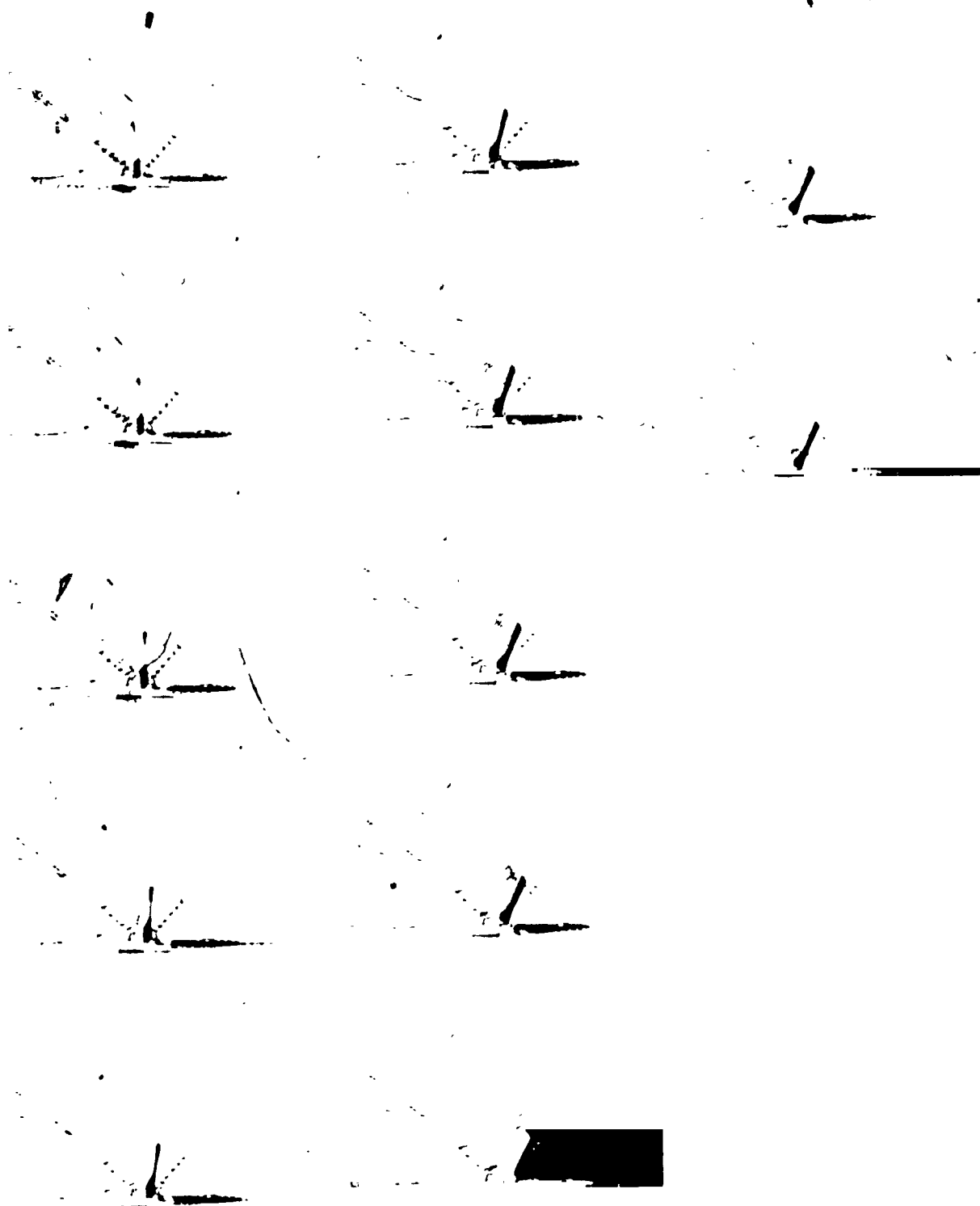


Figure 45, continued

# DISPLACEMENT VS TIME

TYPE II BAFFLE, SPRING SET 2,  $U_T/D = 1.80$

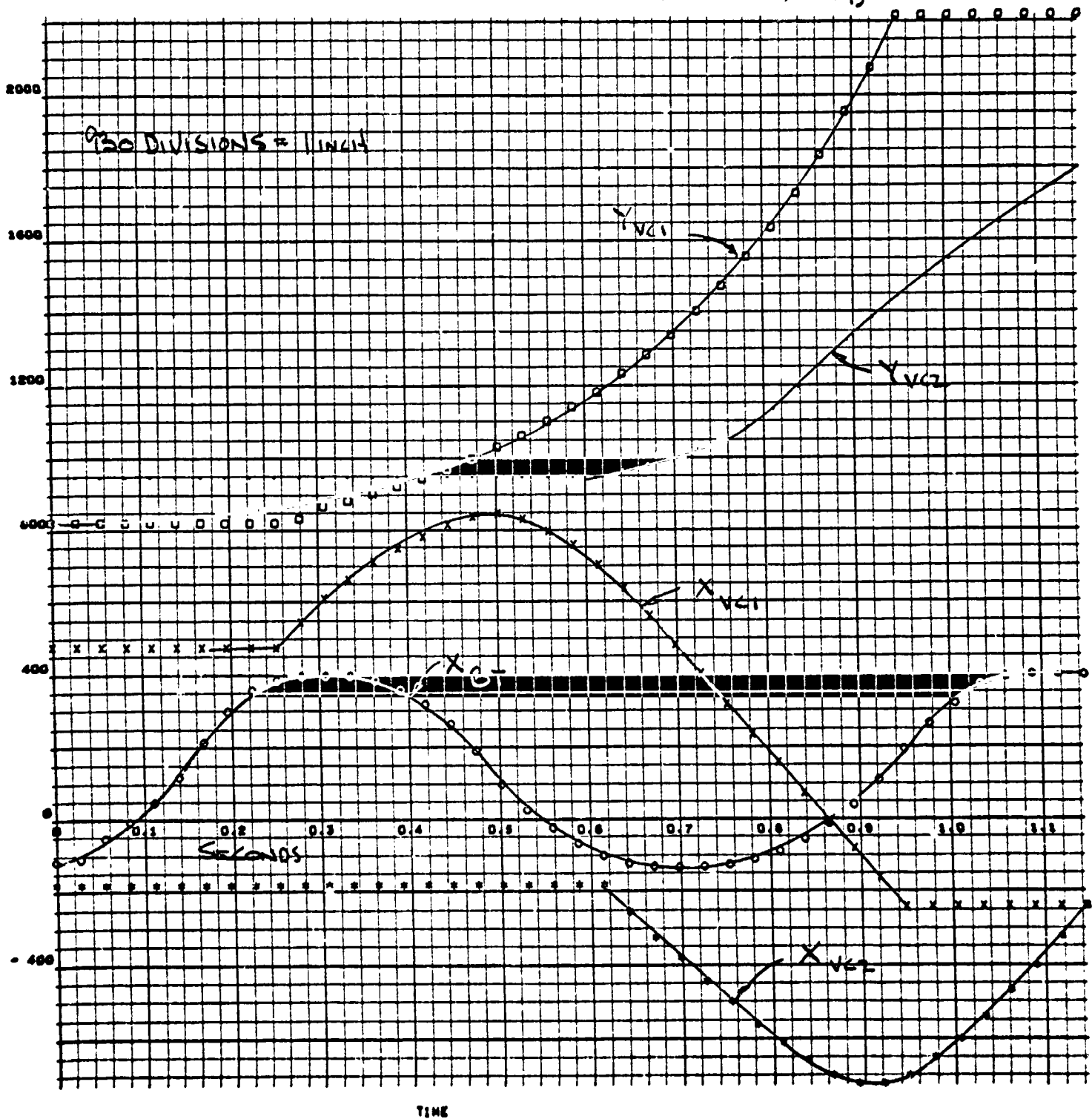


FIGURE 46

# VELOCITY VS TIME

TYPE II BARRIE,  $\frac{U_T}{D} = 1.80$ .  
SPRING SET 2.

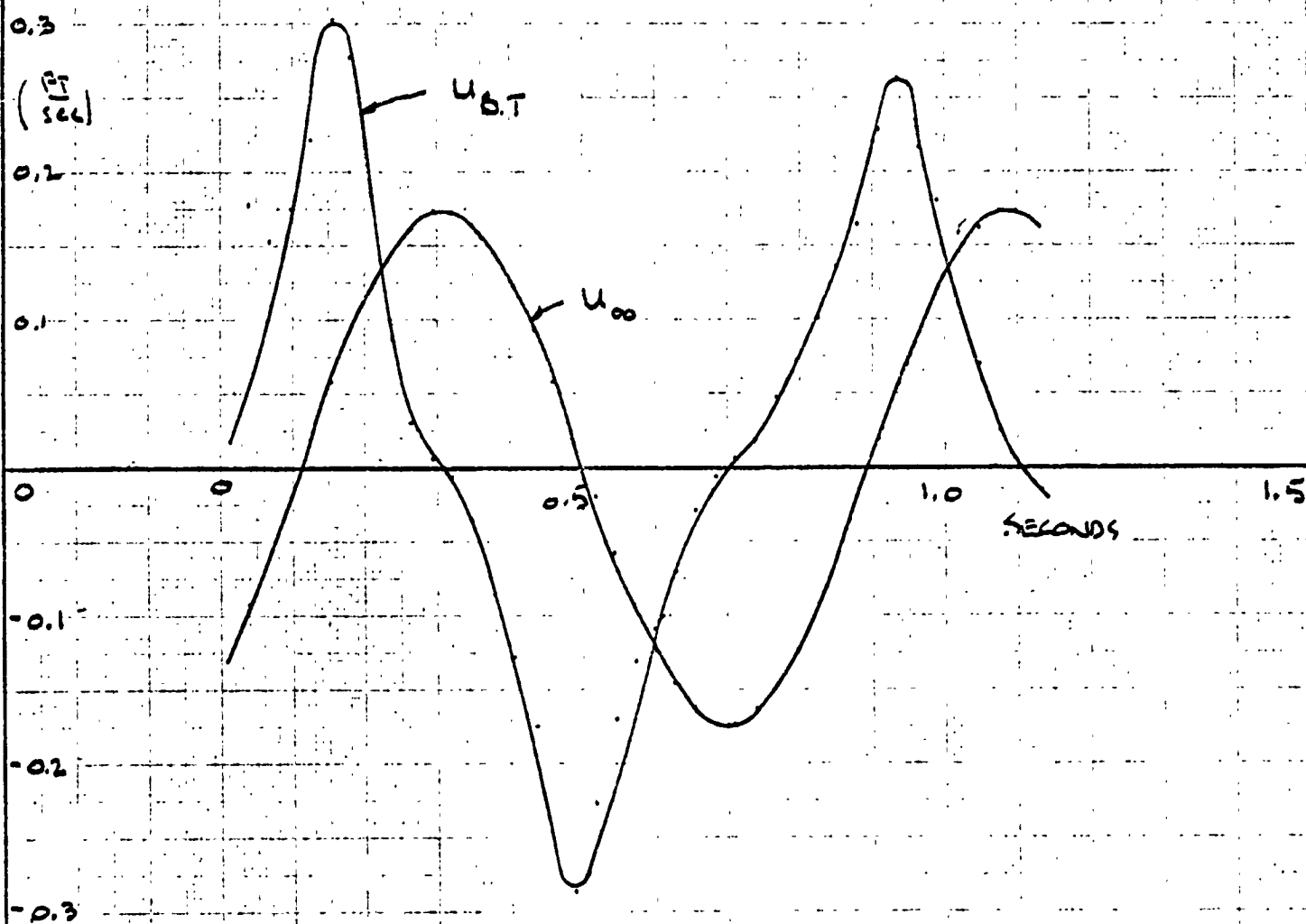


FIGURE 47

BAFFLE TIP AND  
VORTEX CENTER X VS Y  
TYPE II BAFFLE, SPRING SET 2,  $UT/D = 1.80$

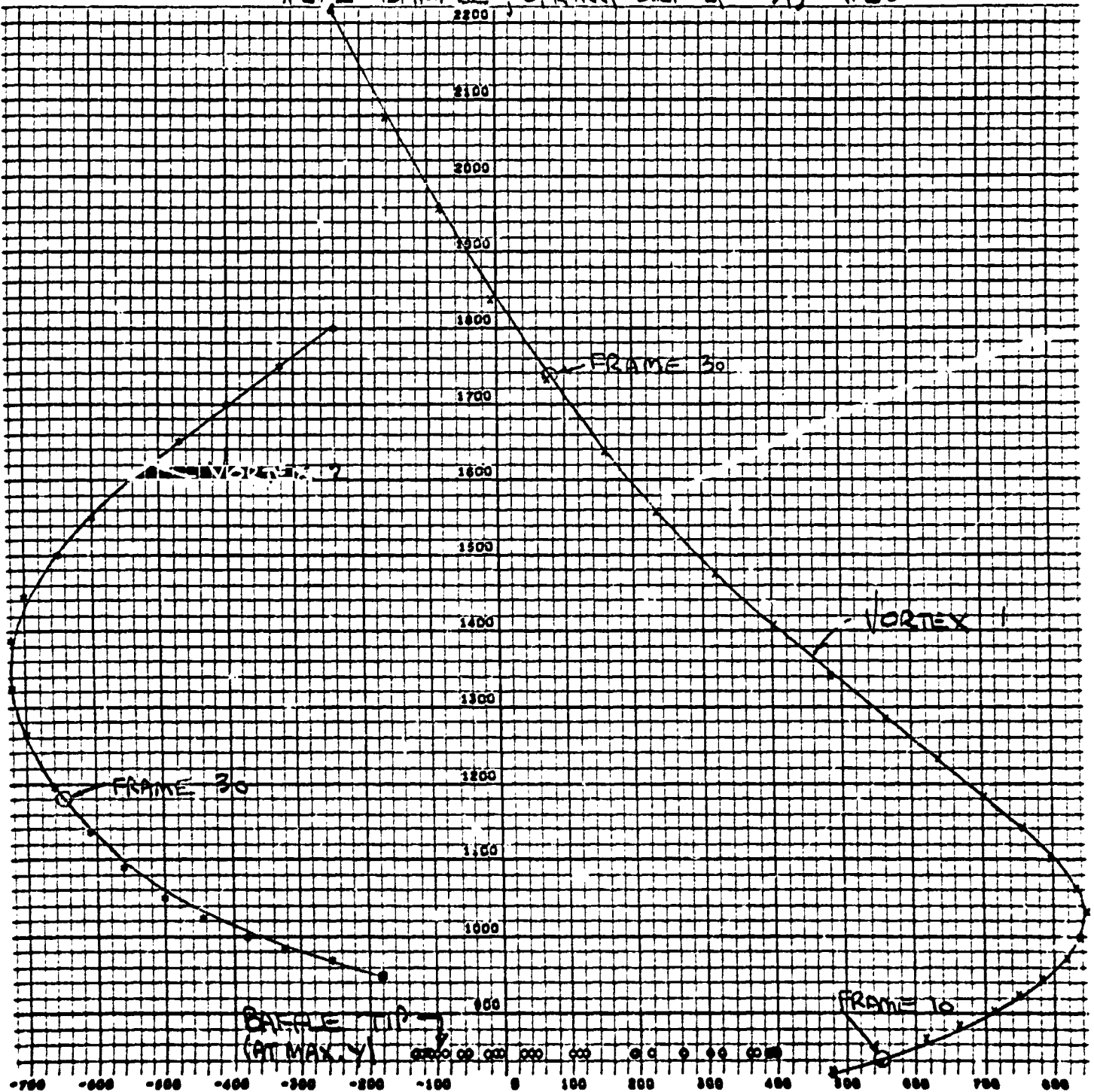


FIGURE 48



# Flexion Baffle Data

DISPLACEMENT - IN

VS

TIME

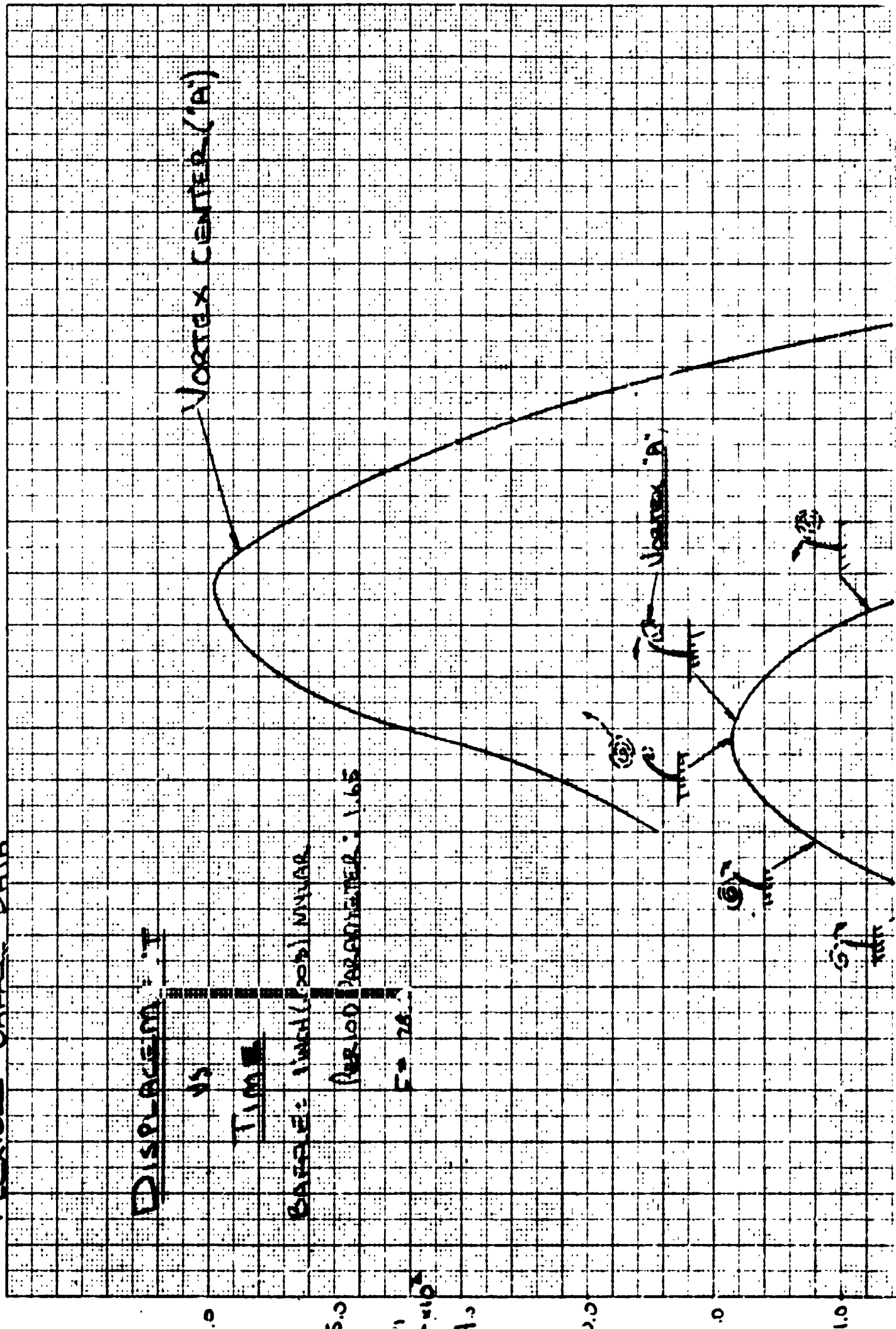
BAFFLE: 1 INCH (20) MINOR

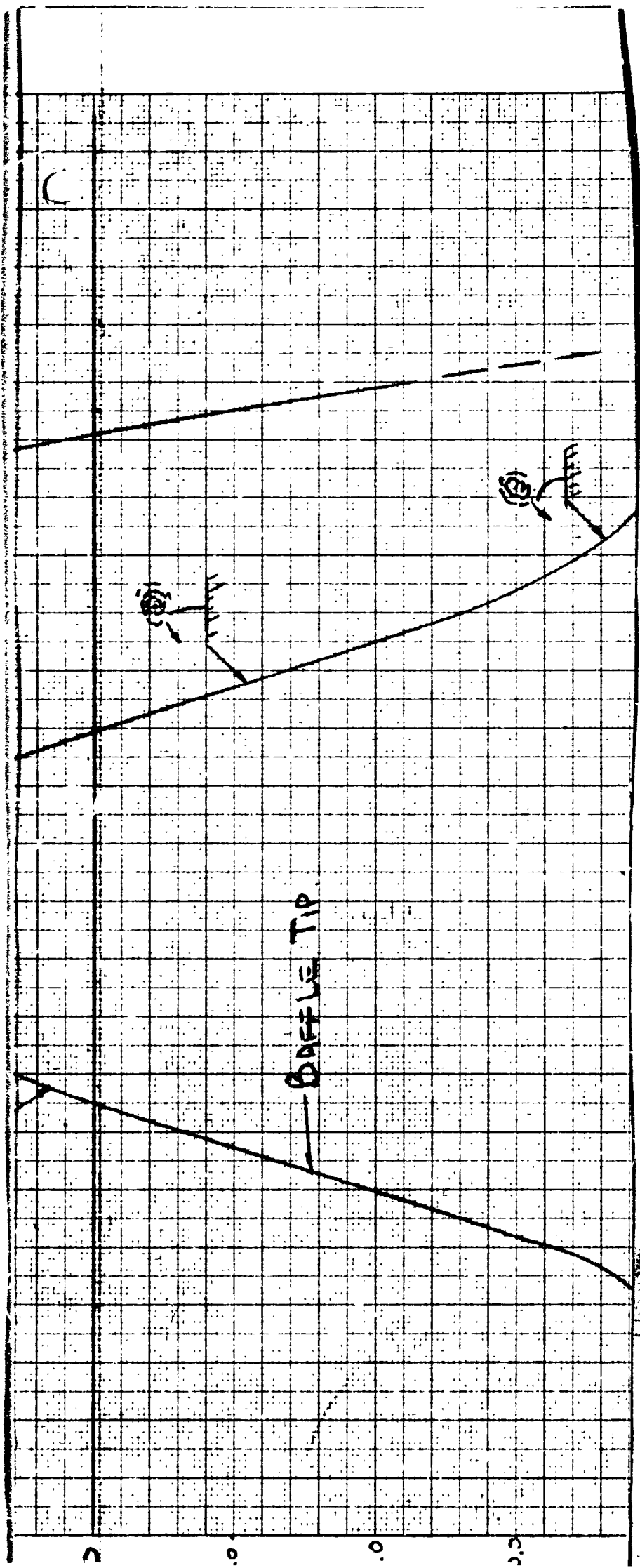
PERIOD PARAMETER: 1.65

$E = 28 \times 10^6$

Vortex Center (in)

Vortex "A"





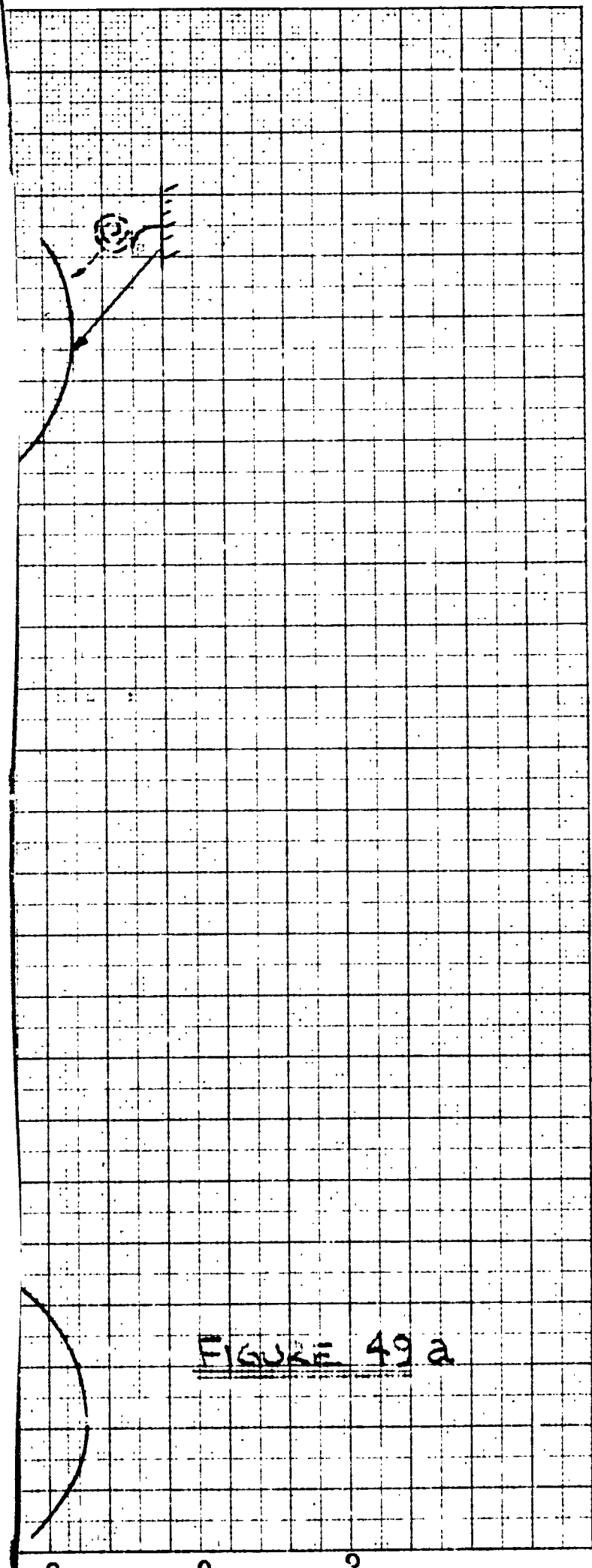


FIGURE 49 a

# VELOCITY vs TIME

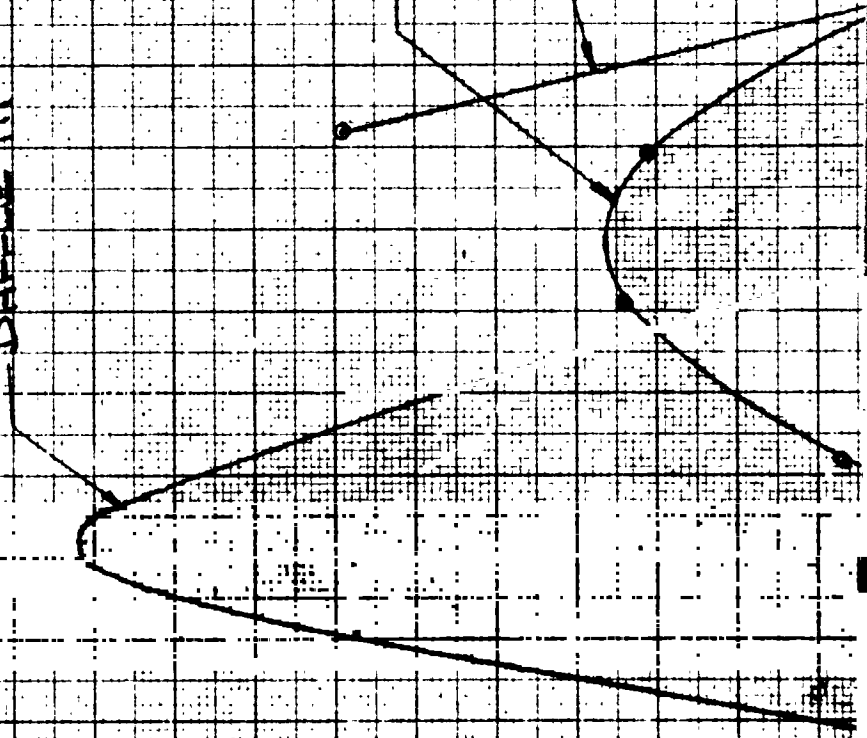
BAFFLE: 1 INCH (0.0254 M) DIA

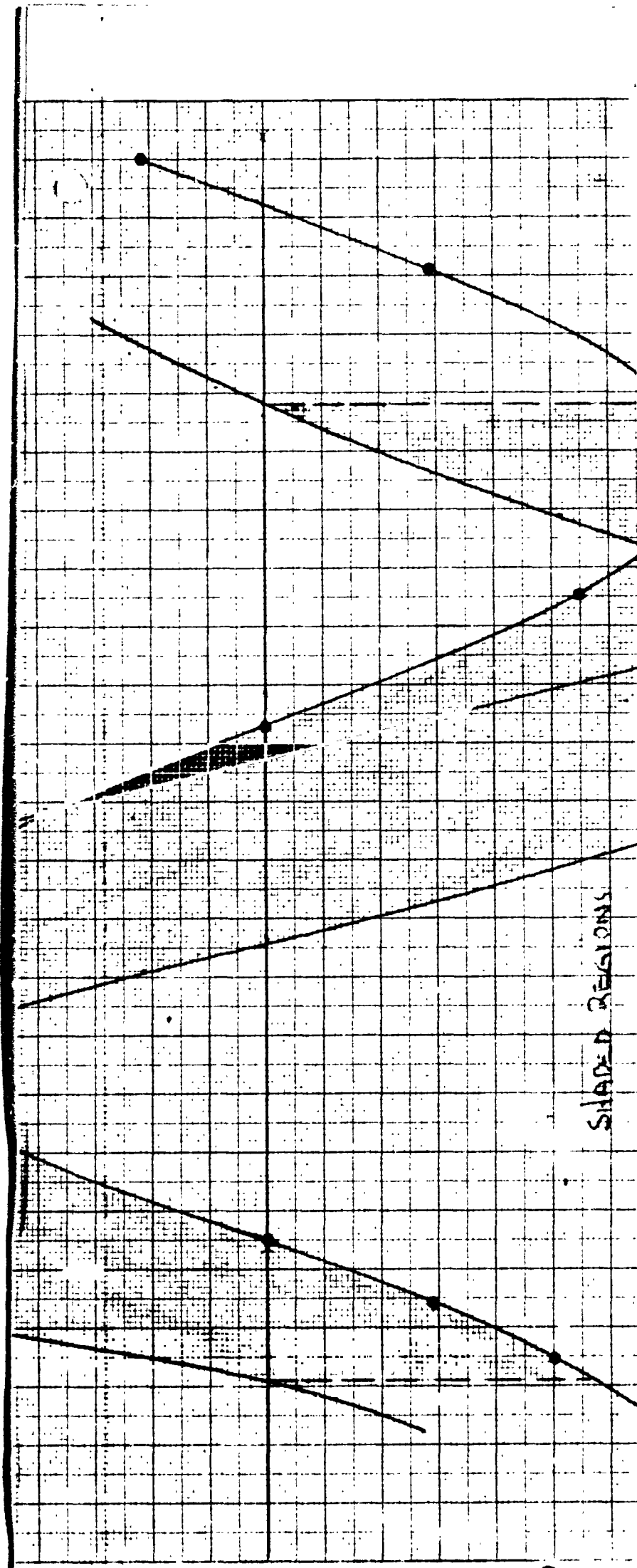
PERIOD: 1.165

BAFFLE TIP

FLUID AT BAFFLE TIP

VORTEX CENTER





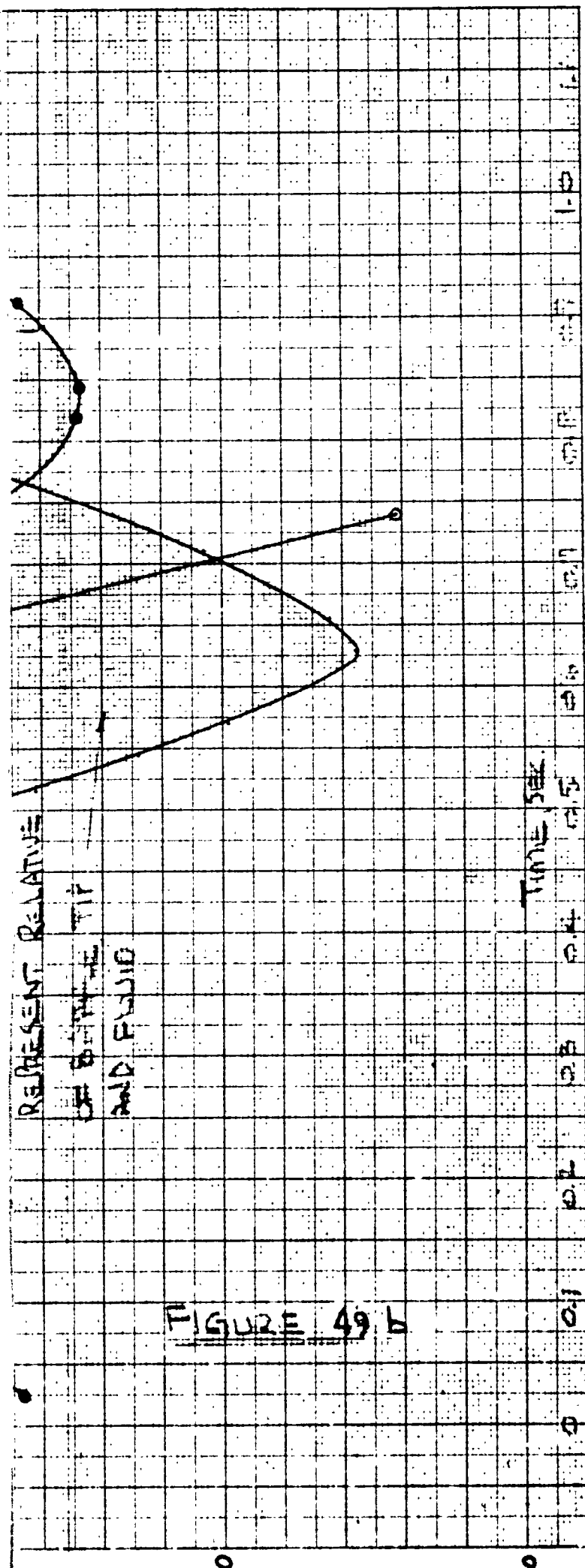


FIGURE 49 b

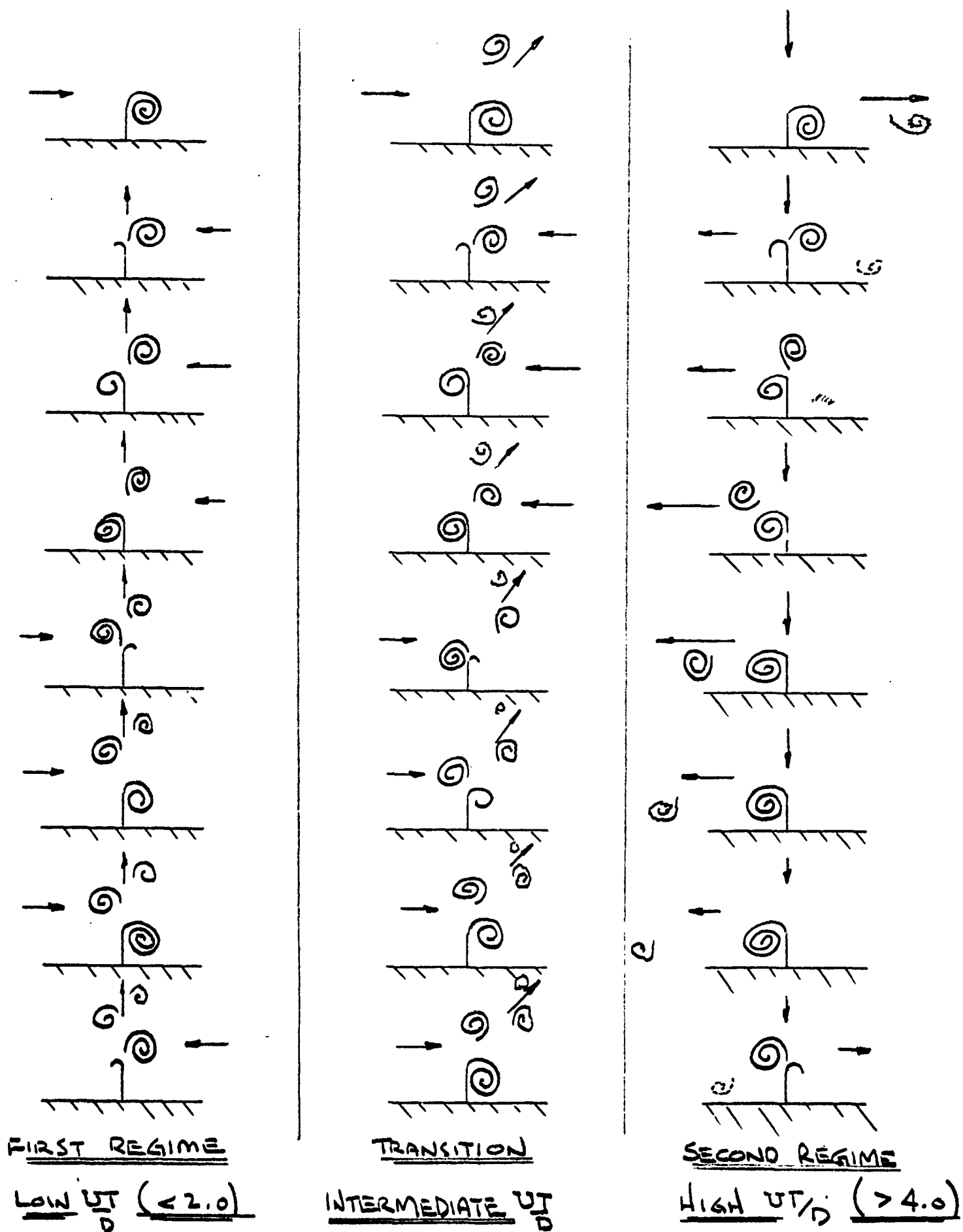
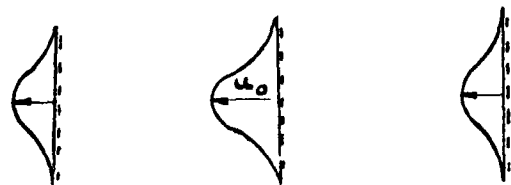
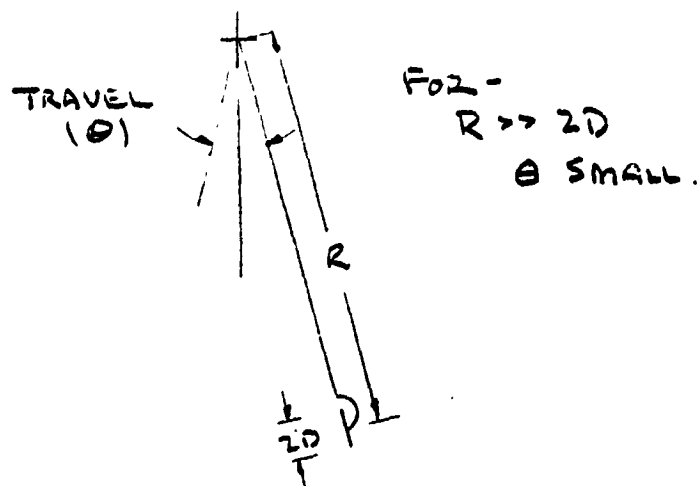
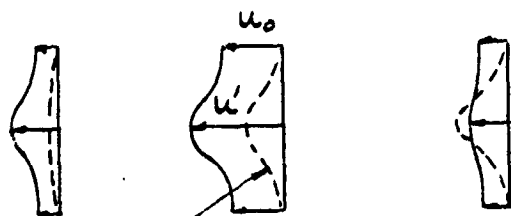


FIGURE 50



(1ST SWING)  
 ABSOLUTE VELOCITY  
 PROFILES AT TIME  
 FORMED



(RETURN SWING)  
 VELOCITY PROFILE  
 THAT BAFFLE SEES  
 (RELATIVE TO PARTICLES)

PARTICLE POSITION

FIGURE 50 (a)

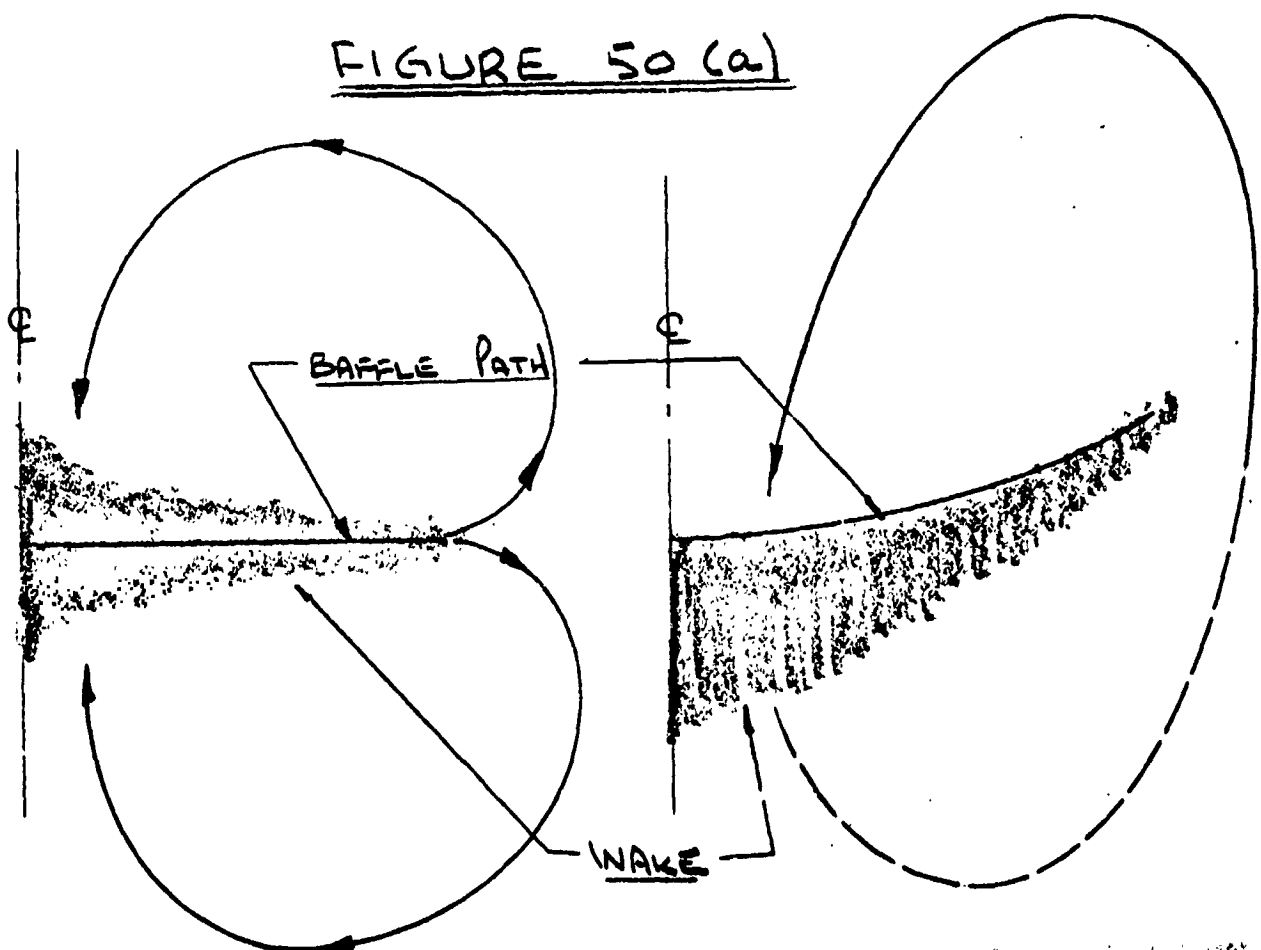
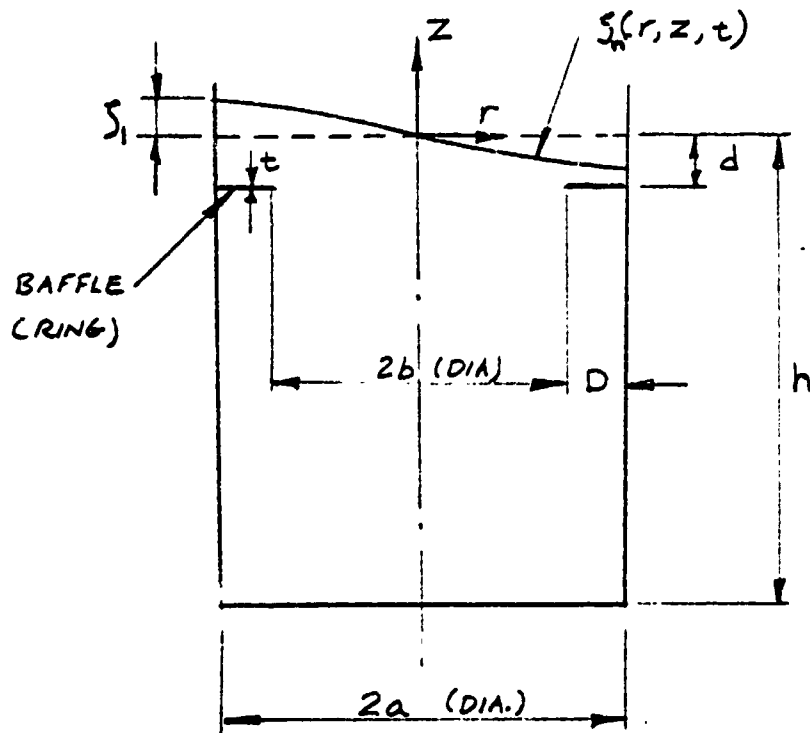


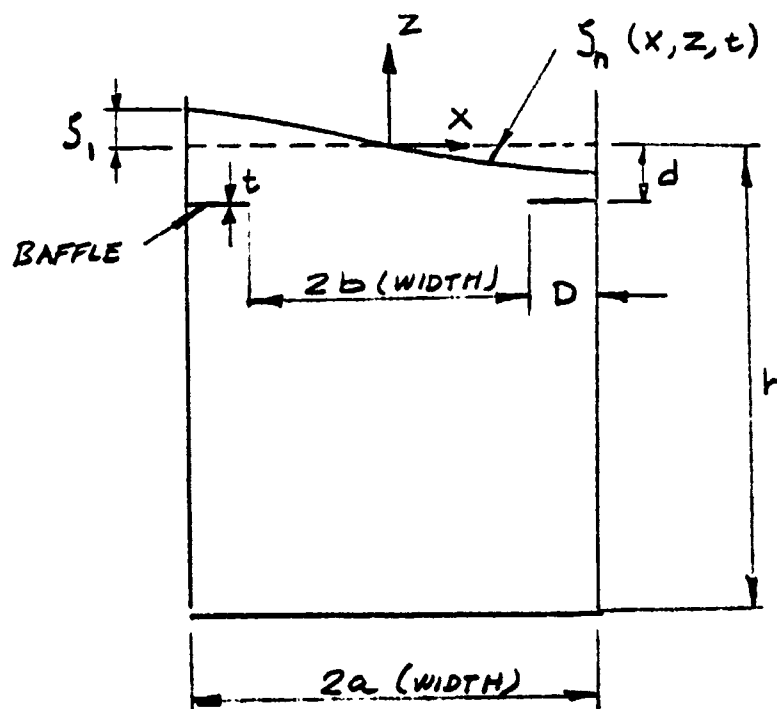
FIGURE 50 b, c (WAKE, RADIUS ARM)



FIG. 51 TANK CONFIGURATIONS



CIRCULAR  
CYLINDRICAL  
TANK



RECTANGULAR  
TANK  
LENGTH = L

FIG. 52. MAXIMUM STRESS IN CANTILEVER  
BAFFLES WITH UNIFORM LOADING.

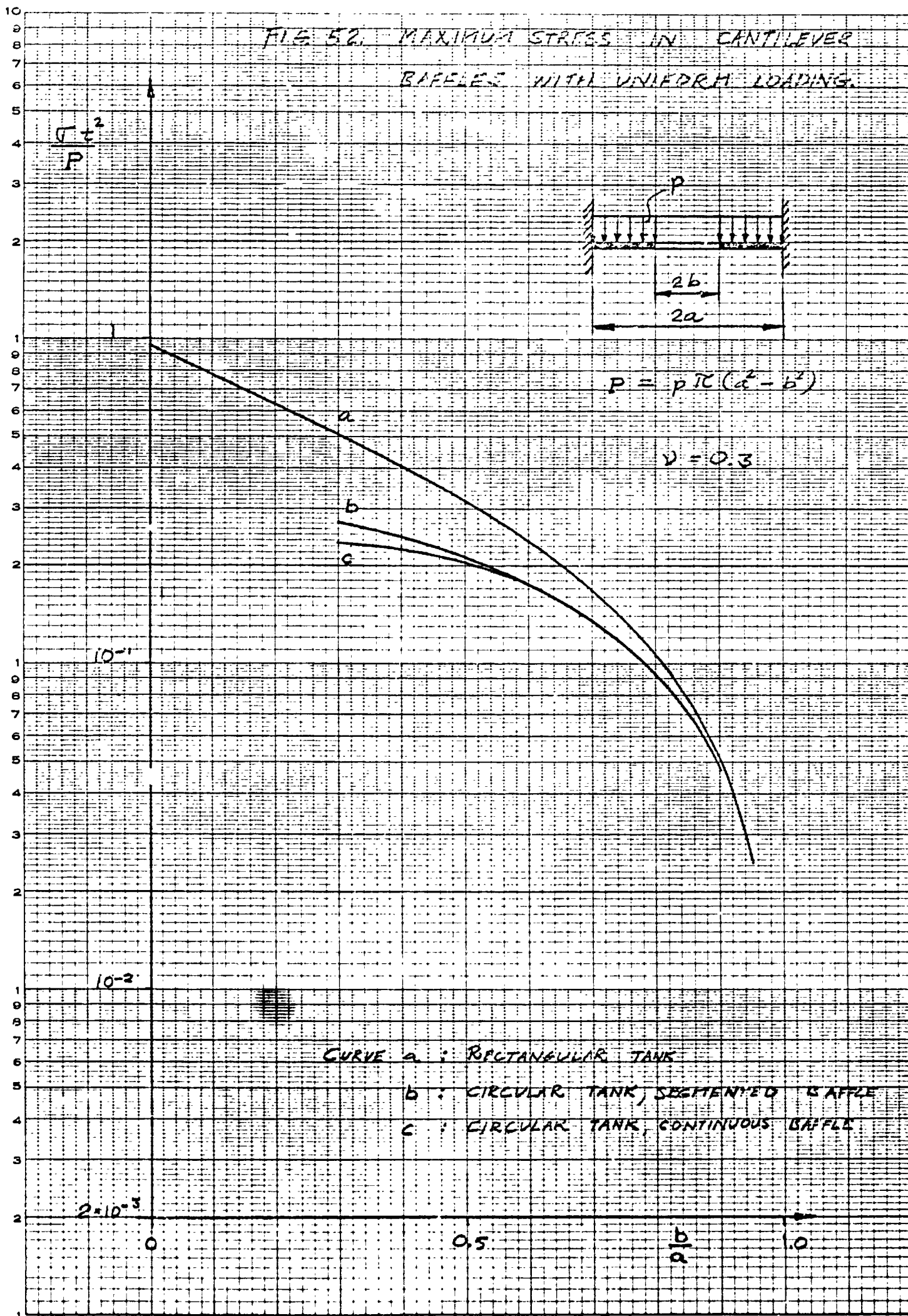


FIG. 53. T.P. DEFLECTION, CANTILEVER

BAFFLE WITH UNIFORM LOADING

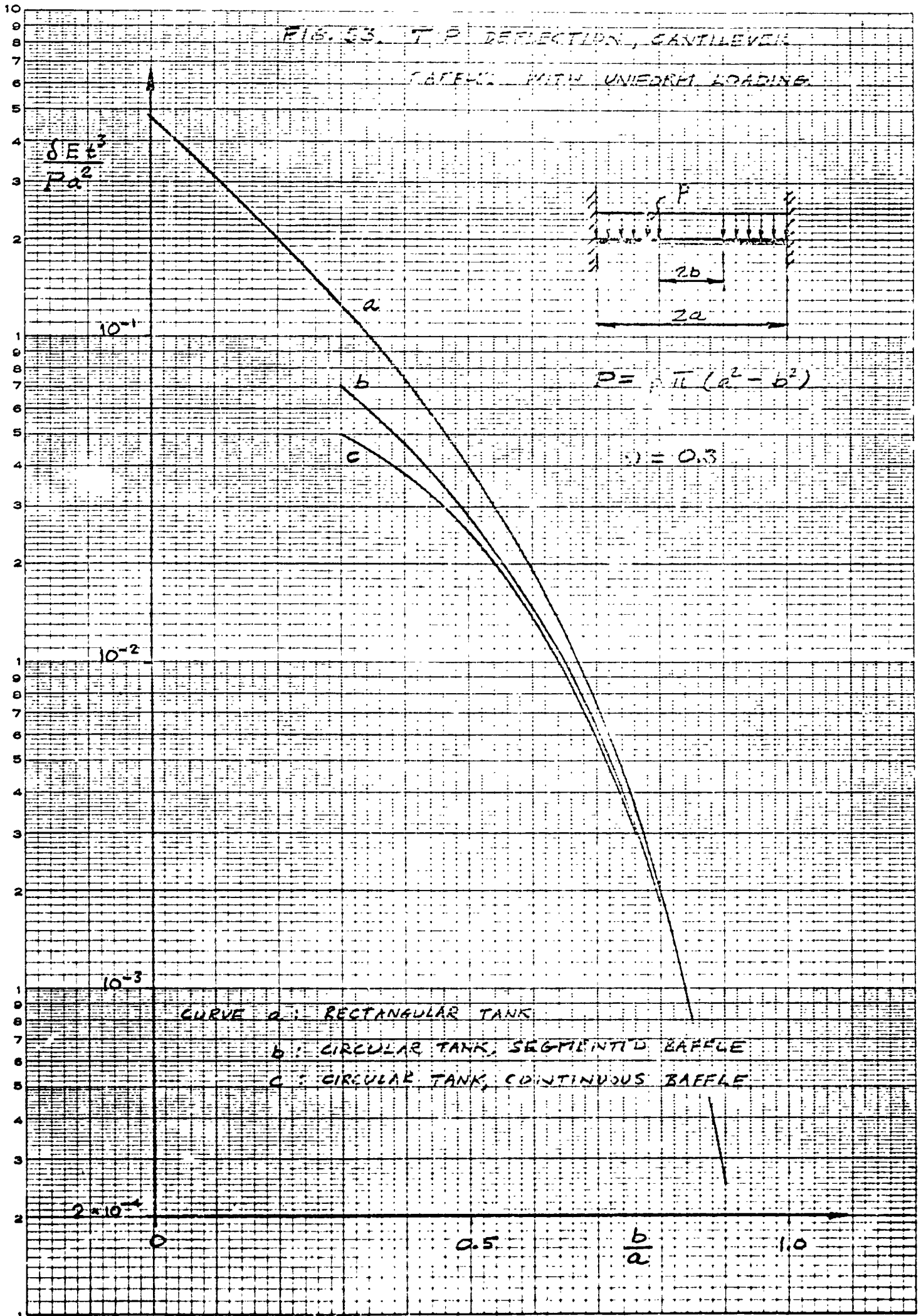
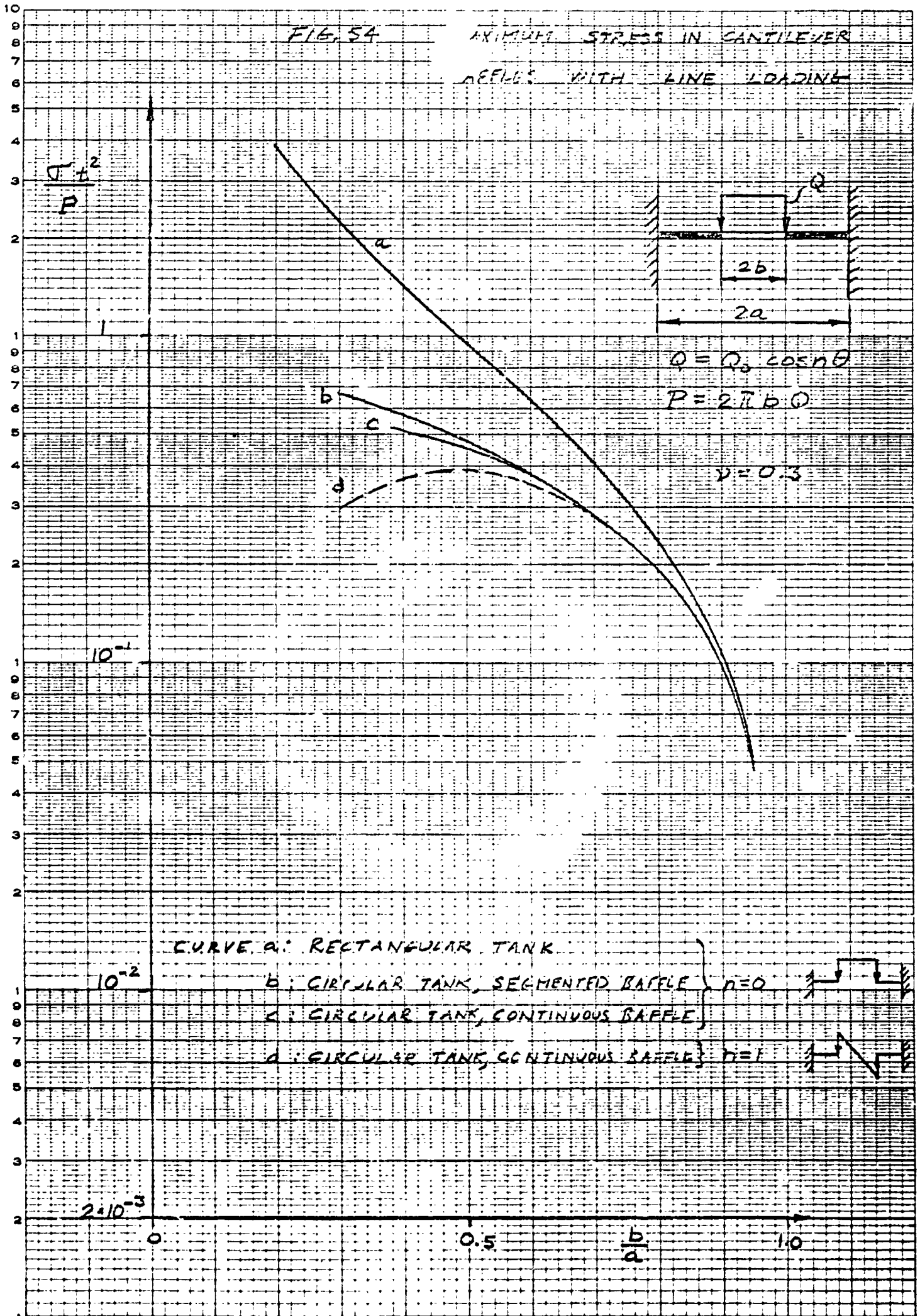


FIG. 54

MAXIMUM STRESS IN CANTILEVER  
REFLECTS WITH LINE LOADING



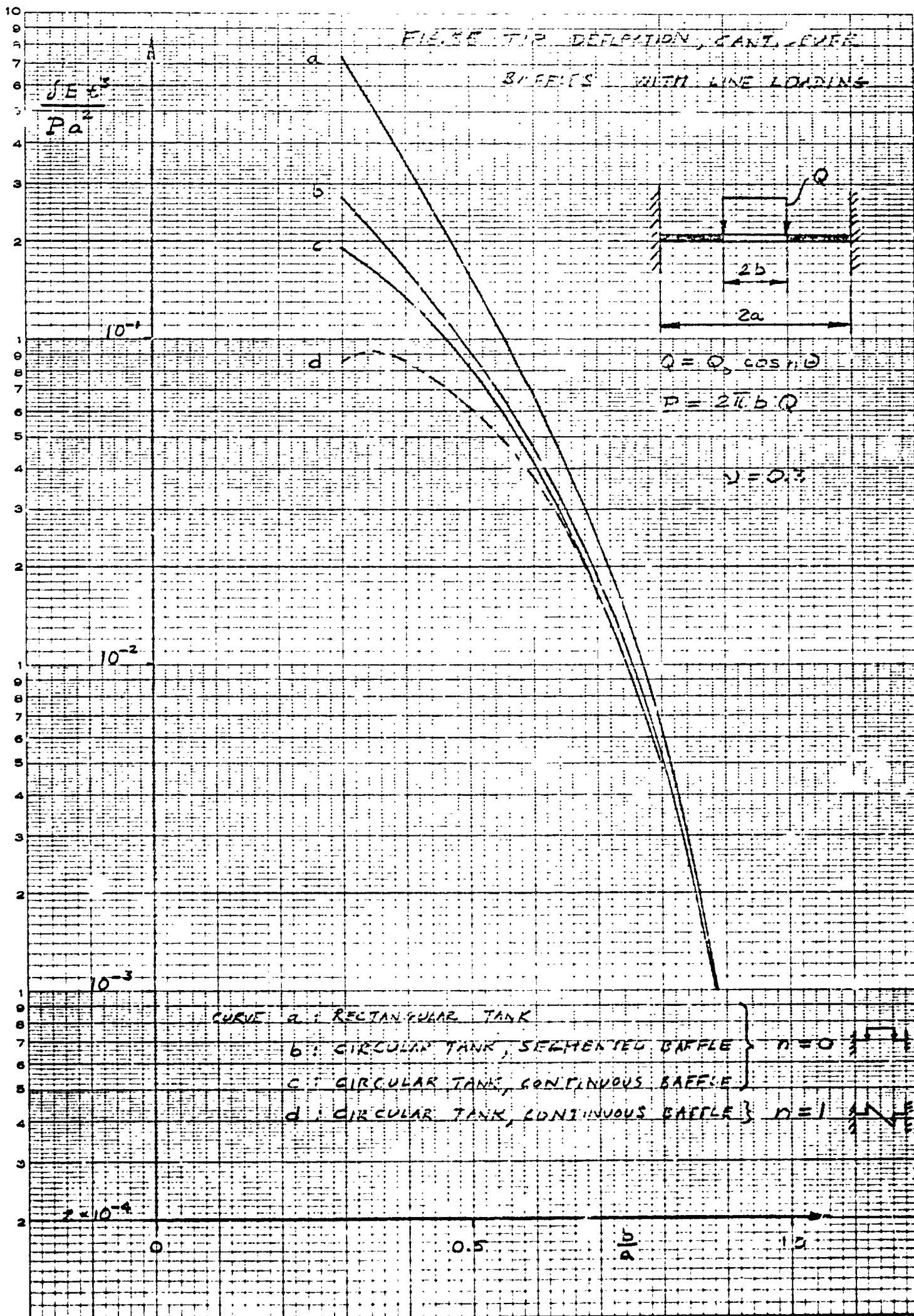




FIG. 36

RELATIVE TIP DEFLECTION

$$\frac{\delta}{\delta_{50}} = f\left(\frac{L}{50}\right)$$

1.0

0.5

0

0

0.5

1.0

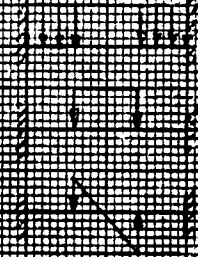
1.5

$\frac{\delta}{\delta_{50}}$  =  $\frac{\text{TIP DEFLECTION OF CURVED DUTCH}}{\text{TIP DEFLECTION OF STRAIGHT DUTCH}}$

CURVED DUTCH UNIFORM LOAD

W LINE LOAD

W LINE LOAD



$$C_L = A(F_A) \left[ \frac{U_I}{D} \right]^{B(F_A)} - J(F_A) e^{-(E(F_A) \frac{U_I}{D})} + H(F_A) e^{\left[ \frac{1}{G(F_A) U_I} \right]}$$

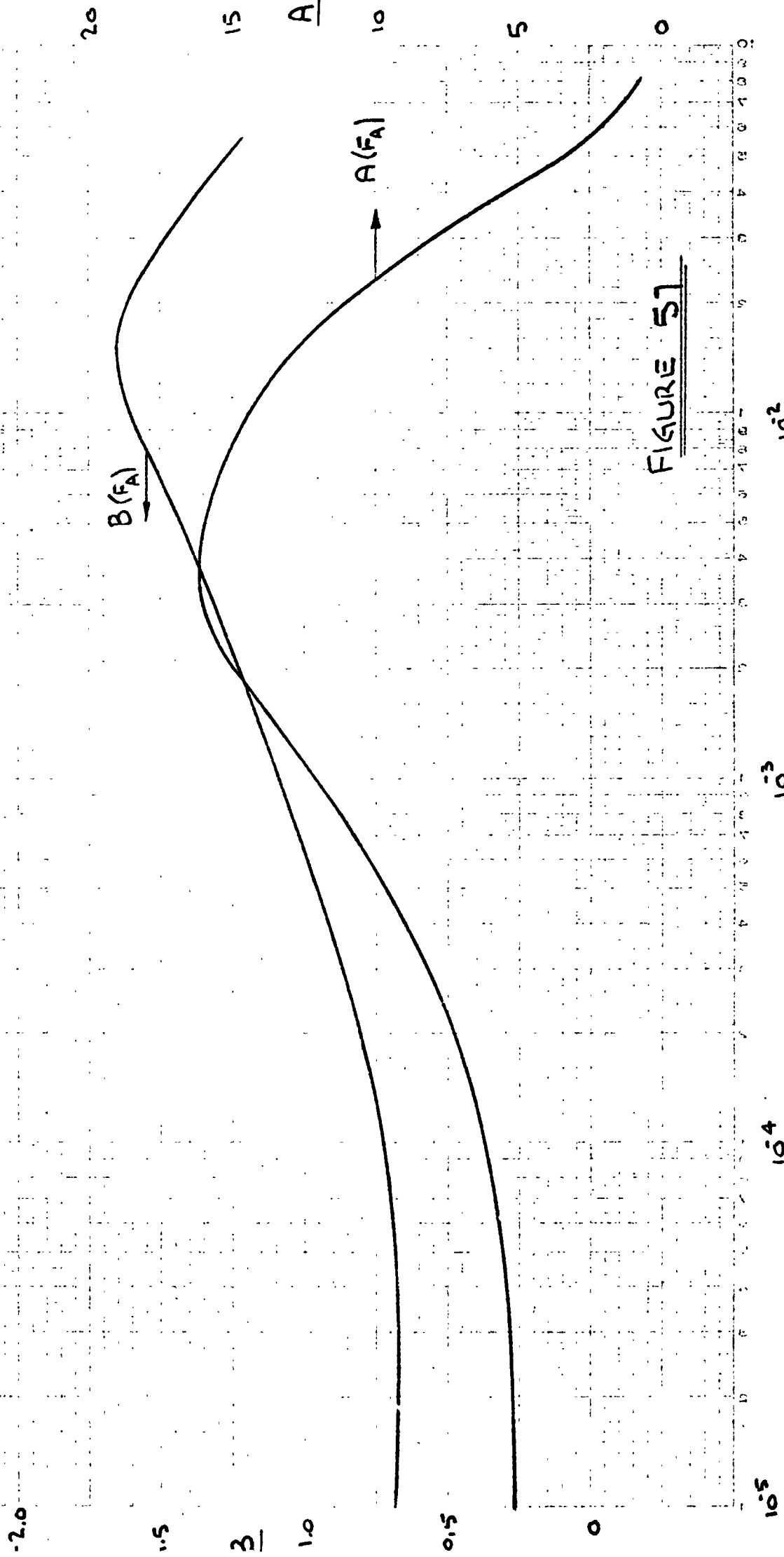


FIGURE 51

$$C_L = A(F_A) \left[ \frac{U_T}{D} \right]^{B(F_A)} - J(F_A) e^{-(E(F_A) \frac{U_T}{D})} + H(F_A) e^{\left[ \frac{1}{A(F_A) D} \right]}$$

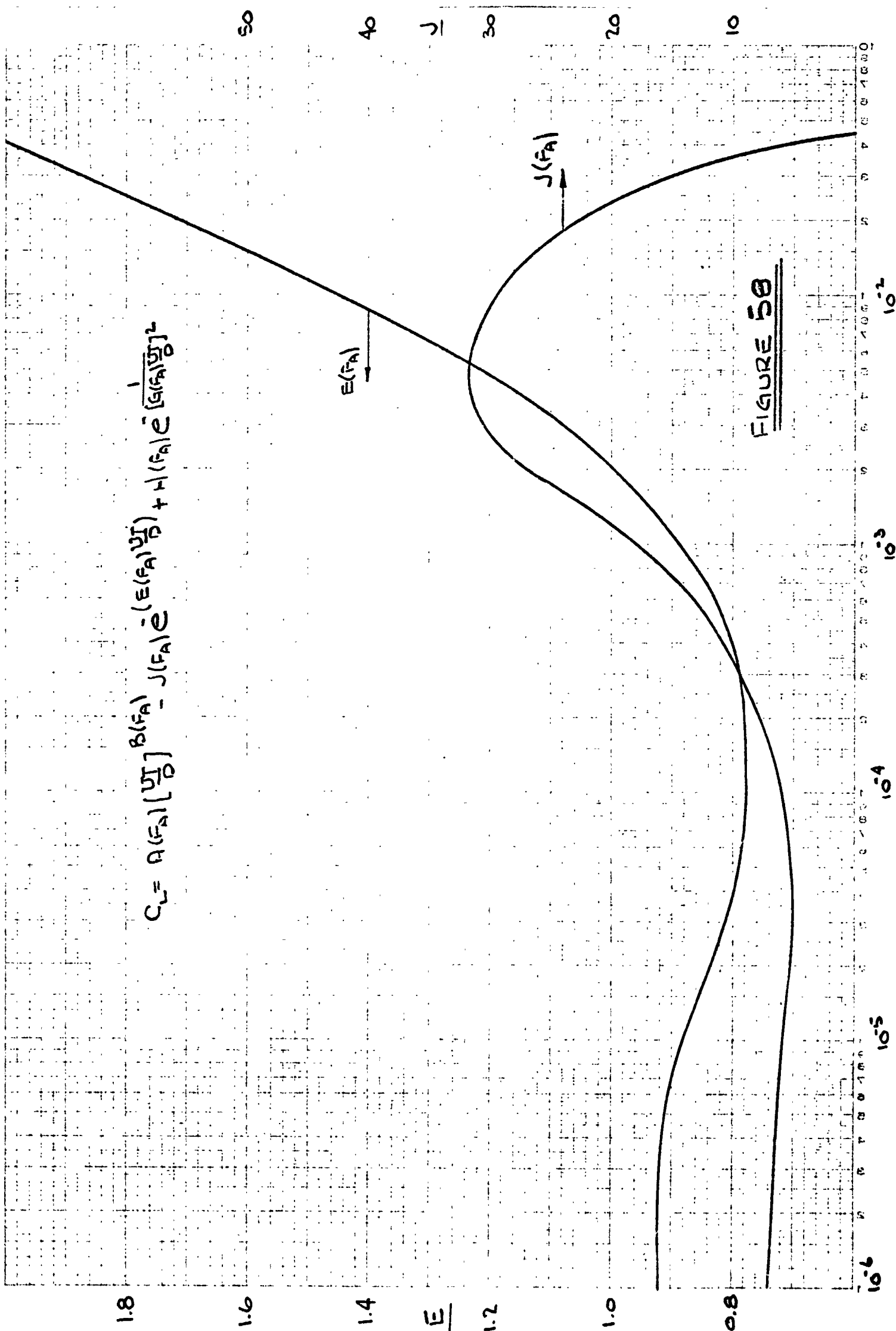


FIGURE 58



$$C_L = A(F_A) \left[ \frac{V_A}{D} \right]^{B(F_A)} - J(F_A) e^{-(E(F_A) \frac{V_A}{D})} + H(F_A) e^{\frac{1}{[G(F_A) \frac{V_A}{D}]^2}}$$

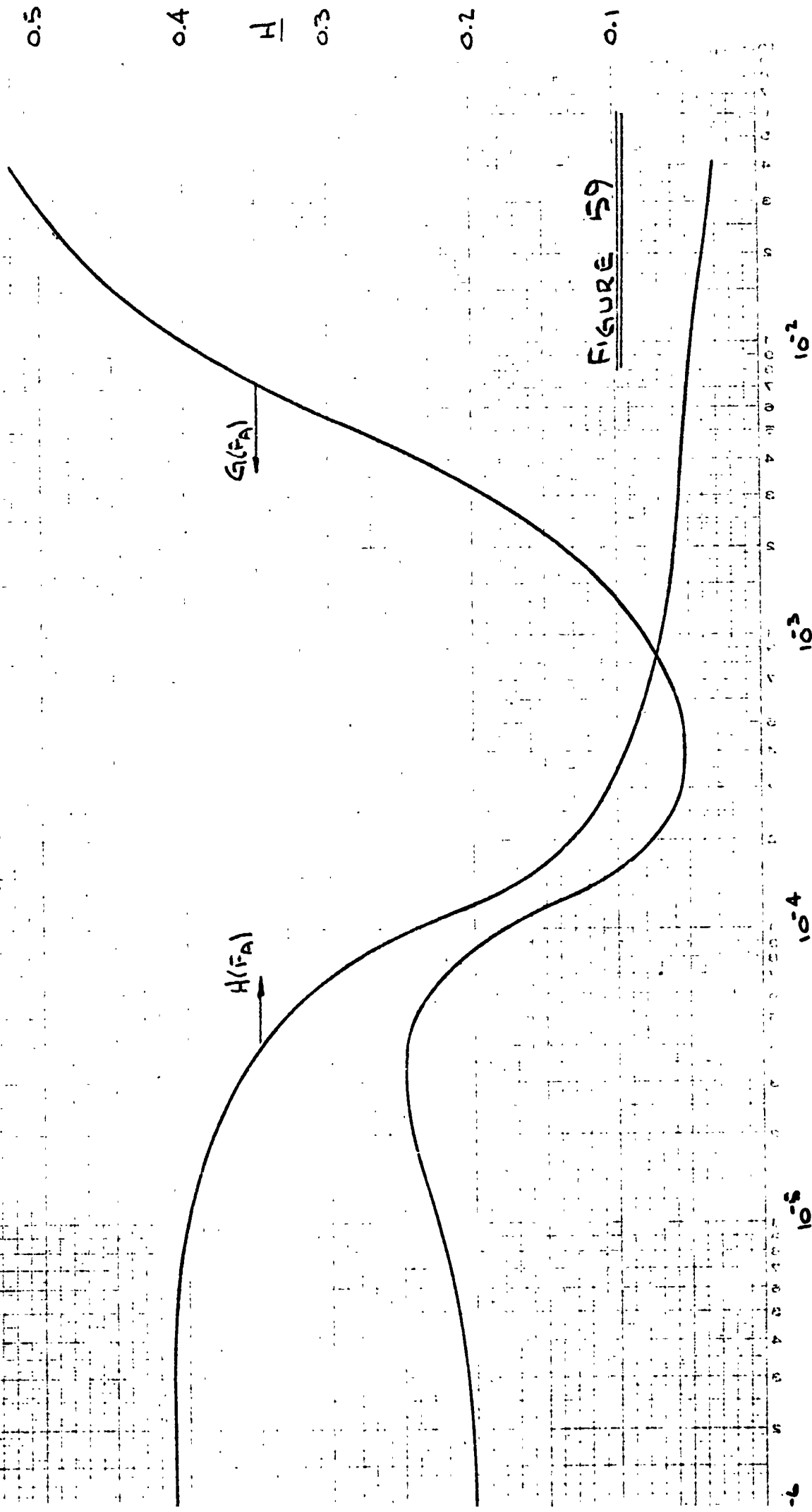


FIGURE 59

$$F_A = 8.83 \times 10^{-2} \left(\frac{\rho}{\rho_0}\right)^3 \left(\frac{\rho}{\rho_0}\right)^2 \frac{d^4}{E} f\left(\frac{b}{a}\right)$$

$$\left(\frac{\rho_s}{\rho_{s0}}\right), \text{ vs } F_A$$

RELATIVE HYDRODYNAMIC EFFICIENCY  
CIRCULAR CYLINDER  
LATERAL SLOSH

FOR  $\nu = 0.3$

$$\left(\frac{\rho_s}{\rho_{s0}}\right)$$

BEST WEIGHT  
EFFICIENCY

$\frac{W}{D} = 2$

4  
6  
10 20 30  
40

FIGURE 60

FLEXIBILITY,  $F_A$   
EUGENE DIEZGEN, CO.

2 CYCLES X 10 DIVISIONS PER INCH  
BLANK-FORMATION  
NO. 3408-7210 DIEZGEN GRAPH PAPER

BAFFLE WEIGHT EFFICIENCY

CIRCULAR CYLINDER

LATERAL SLOSH

$$\frac{\pi}{\left(\frac{E}{\rho a^3}\right)^{1/3} \left(\frac{\rho}{a}\right)^{-2/3} \left[f(-1)\right]^2 \left[f\left(\frac{b}{a}\right)\right]^{-1/3}}$$

$$F_A = 0.83 \times 10^{-2} \left(\frac{\rho}{E}\right)^3 \left(\frac{\rho}{a}\right)^2 \left(\frac{b}{E}\right)^4 f\left(\frac{b}{a}\right)$$

For  $\nu = 0.3$

BEST WEIGHT EFFICIENCY

$\frac{D}{T} = 2$   
4  
6  
10  
20  
30

FIGURE 61

NOTE: FIGURE ALSO APPLICABLE TO RECTANGULAR TANK - SEE TEXT

FLEXIBILITY,  $F_A$

2 CIRCLES X 10 DIMENSIONS SEE 1000  
SEMI-CORRELATION  
FOR DIMENSIONS IN INCHES

$$F_A = 4.23 \times 10^{-2} \left(\frac{D}{L}\right)^3 \left(\frac{D}{a}\right)^2 \frac{g a^3}{E} f\left(\frac{b}{a}\right)$$

$$\left(\frac{\gamma_s}{\gamma_{so}}\right)^2 \sqrt{s} F_A$$

RELATIVE HYDRODYNAMIC EFFICIENCY

CIRCULAR CYLINDER

AXI-SYMMETRIC SLOSH

2.0

$$\left(\frac{\gamma_s}{\gamma_{so}}\right)^2$$

1.5 For  $\gamma = 0.3$

1.0

0.5

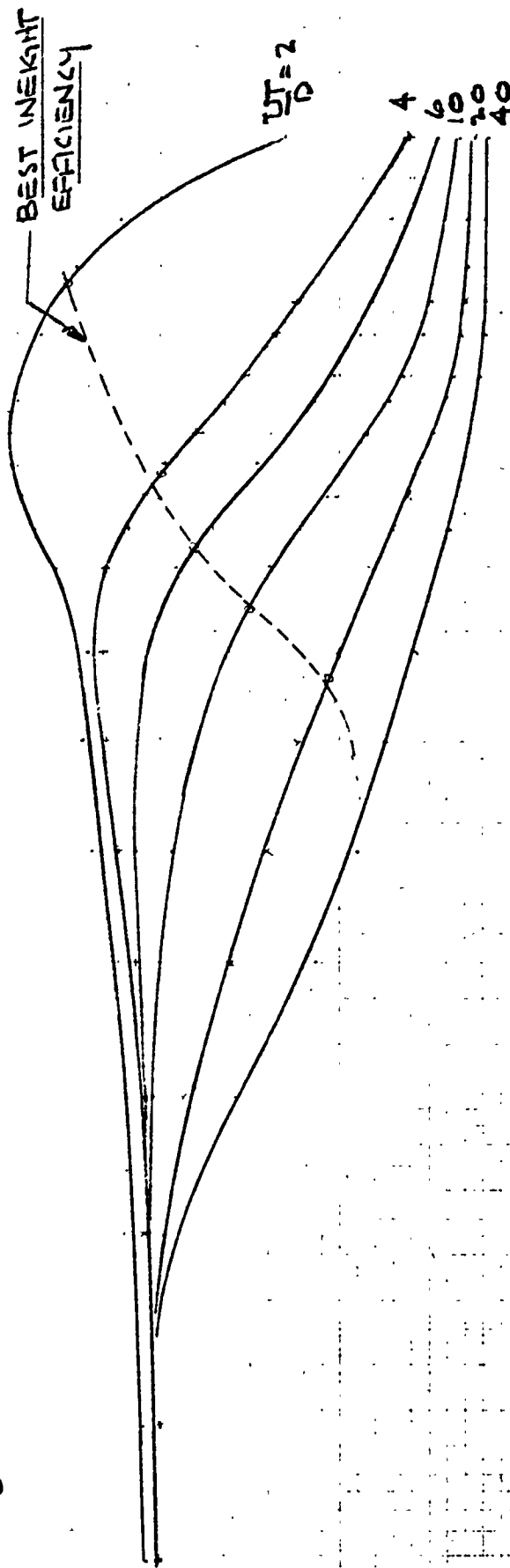


FIGURE 62

10<sup>-6</sup>

10<sup>-5</sup>

10<sup>-4</sup>

10<sup>-3</sup>

10<sup>-2</sup>

10<sup>-1</sup>

FLEXIBILITY,  $FA$

2000-EE X-10 DRIVE OVER 500' HIGH  
SEMI-COORDINATING

# BAFFLE WEIGHT EFFICIENCY

## CIRCULAR CYLINDER

### AXI-SYMMETRIC SLOSH

For  $\nu = 0.3$

$$F_A = 4.23 \times 10^{-2} \left(\frac{D}{L}\right)^3 \left(\frac{D}{a}\right)^2 \frac{g a^3}{E} f(b/a)$$

$$\frac{\pi^2}{\left(\frac{E}{g a^3}\right)^{1/3} \left(\frac{D}{a}\right)^{3/3} [f(-1)]^2 [f(b/a)]^{-1/3}}$$

BEST WEIGHT  
EFFICIENCY

$\frac{D}{L} = 2$

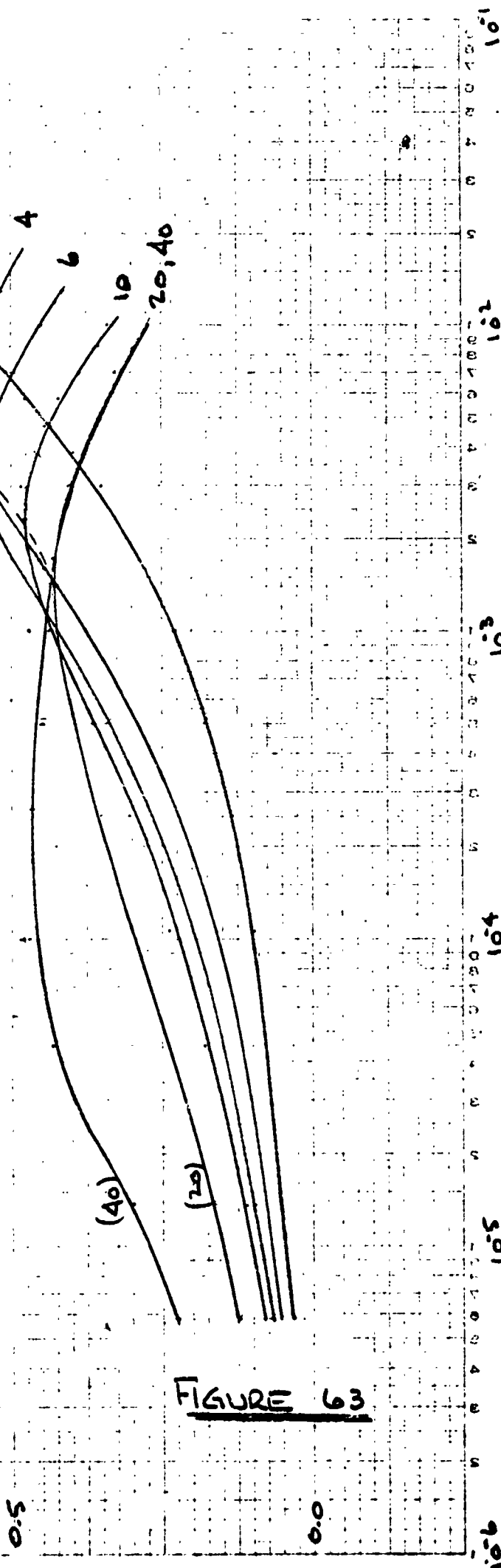


FIGURE 63

RIGID Baffle Damping  
CIRCULAR CYLINDER  
LATERAL SLOSH

$$\gamma_{so} \left( \frac{\tau^2 g}{a} \right) \frac{1}{(2 - \frac{D}{a}) \left( \frac{f_1}{a} \right) [F(-d)]^3}$$

FIGURE 64

